THREE-DIMENSIONAL FINITE-DEFORMATION MULTISCALE MODELING OF ELASTO-VISCOPLASTIC OPEN-CELL FOAMS IN THE DYNAMIC REGIME

BY PEDRO A. ROMERO

A dissertation submitted to the

Graduate School—New Brunswick

Rutgers, The State University of New Jersey

in partial fulfillment of the requirements

for the degree of

Doctor of Philosophy

Graduate Program in Mechanical and Aerospace Engineering

Written under the direction of

Dr. Alberto M. Cuitiño

and approved by

_____

_____

_____

_____

New Brunswick, New Jersey

May, 2008

© 2008
Pedro A. Romero
ALL RIGHTS RESERVED

ABSTRACT OF THE DISSERTATION

Three-Dimensional Finite-Deformation Multiscale Modeling of Elasto-Viscoplastic Open-Cell Foams in the Dynamic Regime

by Pedro A. Romero

Dissertation Director: Dr. Alberto M. Cuitiño

Cellular materials such as metallic and polymeric open-cell foams resemble a labyrinth of interconnected struts surrounded by air-filled voids however a closer inspection reveals a periodicity where a particular unit cell is repeated throughout a lattice inside a matrix of air. Depending on the loading rate, the specifics of the cellular topology and the material properties of the solid phase, the different stages of deformation can involve elasticity, plasticity, fracture, viscoelasticiy, thermoelasticity, strain rate effects, density (microinertia) etc. This dissertation contributes an approach for modeling dynamically loaded open-cell foam materials where the structure is mimicked with the replication of a periodic unit cell composed of a four ligament tetrahedron inside a dual tetrakaidecahedron volume element. Formulation of the Lagrangian for a representative unit cell comprising an imposed macroscopic deformation and enforcement of the principle of minimum action for dissipative systems results in a relation between the globally applied macroscopic deformation and the motion of the internal unit cell vertex, which uniquely defines the kinematic state of each cell and the effective stress state. By maintaining the history of local non-affine motion along with the global affine

deformation, the model is able to capture the microinertial and viscous effects important during dynamic loading of open-cell foams. The micromechanical formulation is used to predict the dynamic compressive uniaxial response of polymeric (visco-elastic) and metallic (elasto-plastic) open-cell foams for different loading rates and structural and material properties gauging the effects of strain rate, viscosity, plasticity and microinertia. The predictions capture the experimentally observed effects namely that as the strain rate increases the foam strength increases and that this effects are more pronounced for more viscous or more massive foams. The micromechanical model alone provides the effective foam response in a numerically efficient manner allowing the user to probe a wide range of material properties and cellular dimensions in a short amount of time. However in order to predict the full field, full range response of an open-cell foam specimen, it is necessary to implement the micromechanical model as a constitutive update into implicit and/or explicit nonlinear dynamic finite element analysis FEA schemes. The FEA simulations clearly capture the experimentally observed signature response with the different stages including the heterogeneous bands of deformation during dynamic compression of cellular materials.

Acknowledgements

Thanks to all the faculty in the department of Mechanical and Aerospace Engineering with whom I've had the opportunity to take a class or to discuss a topic, thank you very much for sharing your knowledge with me. I am very thankful to my dissertation committee members: Prof. Andrew N. Norris, Prof. Ellis H. Dill, and Prof. Hae Chang Gea from Rutgers University and Prof. Winston O. Soboyejo from Princeton University for spending part of their very valuable time inspecting this work and for providing me with suggestions on how to improve this dissertation. I would especially like to thank my advisor, Prof. Alberto M. Cuitiño, for all his patience, guidance, support and encouragement during the past few years. Without Dr. Cuitiño's guidance, this work could not have been completed. Dr. Cuitiño is a brilliant scientist and it has been an honor to spend time with him discussing research ideas in addition to chatting about life. I hope to continue our partnership to expand my ability to work on technical, scientific problems.

I would also like to acknowledge Dr. Shanfu F. Zhang for his invaluable assistance and helpful suggestions with the work presented here. Thanks to the current graduate director, Dr. Haim Baruh and special thanks to the former graduate director Dr. Haym Benaroya for accepting me into the department at a difficult time in my professional career. I thank the current and past members of Dr. Cuitiño's group including Kinjal Dhruva, Daniel Braido, Alisar Tunser, Dr. Shanfu Zhang, Dr. Stephen Kutchnique, Dr. Moises Smart, and Dr. Zhan Gao. Also, thanks to the past and current graduate students in the department with whom I the opportunity to interact such as Lucian, Edward, Jason, Elan, Paola, David, etc. I would also like to thank the staff at the MAE department including Bill Vasiliou, John Petrowski, Virginia Dare, Beatrice Vena, Helene Press, and Aiesha Jenkins for their assistance during my stay at the department.

I want to express my gratitude to the Center for Advanced Food Technology ($CAFT$) at Rutgers University for partially supporting my graduate work. I would also like to thank and acknowledge the National Science Foundation and Rutgers $GK12$ fellowship program for its financial support during my early years as a graduate student. Special thanks go to Dr. Kathleen Scoth and Suan Colettta of the $GK12$ program for their support, understanding, and assistance over those years. The opportunity to interact with young middle school students was very enjoyable and rewarding because while I shared my scientific knowledge and experiences with the students I was able to improve my teaching technique. I will make an effort to always get involved in similar programs in the future. Next, I would also like to sincerely thank Dean Ilene Rosen and Dean Donald Brown from the Office of Student Development for their great support and encouragement ever since I first came to Rutgers for the Engineers of the Future Program. Finally, I would like to thank my family Isidro, Maria, Daysi, Mario, Lindon, and Reynaldo. Thanks to SHE, SHPE, and CAHSEE for helping me expand my interpersonal skills. Thanks to my Rutgers engineering friends including Javier Ibañez, Lenin Medina, German Quisbert, Joseph Retuerto, David Tabora, Juan Plummer, Gerald Vasquez, Ervin Hernandez, and Joan Ortega for their friendship over the years.

Dedication

To my father, Isidro Romero
and my mother, Maria Romero.

Table of Contents

Abstract ii

Acknowledgements iv

Dedication vi

List of Tables x

List of Figures xi

1. Introduction 1

1.1. Introduction to Foams 1

1.1.1. Synthesis of Foams 3

1.1.2. Structure of Foams 5

1.1.3. Properties of Foams 6

1.1.4. Applications of Foams 7

1.1.5. Typical Mechanical Behavior 8

1.2. Review of Relevant Previous Works 10

1.2.1. Pioneering Mechanics Works 11

1.2.2. Recent Work 11

1.2.3. Dynamic Loading 12

Strain Rate Dependency 13

1.2.4. Modeling 14

1.3. Overview of the Dissertation 18

2. Micromechanical Modeling of Dynamically Loaded Open-Cell Foams 22

2.1. Introduction 22

2.2. General Framework 27

2.3. Formulation of the Model 27

2.3.1. Kinematics 29
2.3.2. Local Constitutive Relations 34
2.3.3. Linking Local to Global 35
Mass and Relative Density 36
Kinetic Energy Terms 37
Potential of the Inertial Forces 38
Elastic Potential Terms 38
Dissipative Potential Terms 40
Equilibrium Condition 41
2.3.4. Macroscopic Stresses 42
Material Frame Indifference 44
2.4. Predictions of the Theory 47
2.4.1. Cell Geometry and Ligament Response 48
2.4.2. Effective Theoretical Predictions 51
2.5. Conclusions 58

3. Micromechanical Modeling of Dynamically Loaded Open-Cell Metallic Foams: Yielding, Collapse and Strain Rate Effects 61
3.1. Introduction 61
3.2. Formulation 65
3.2.1. Micromechanical Model 66
3.2.2. Cell Wall Constitutive Behavior 68
Strut Axial Response 69
Strut Bending Response 71
3.3. Predictions 73
3.4. Conclusions 77

4. Harnessing Continuum Mechanics and Finite Element Analysis Schemes to Predict the Behavior of Open-Cell Foams 80
4.1. Introduction 81
4.2. Continuum Framework 83

4.2.1. Derivation of the Weak Form 84
4.3. Finite Element Analysis Framework 86
4.3.1. Spatial Discretization 87
4.3.2. Temporal Discretization 89
4.4. Micromechanical Formulation 91
4.4.1. Kinematic Equilibrium Condition 93
4.4.2. Macroscopic Stress State 94
4.4.3. Stress Tangents 95
4.4.4. Numerical Notation 97
4.5. Predictions 99
4.5.1. Polymeric Visco-Elastic Foam Predictions 99
4.5.2. Metallic Elasto-Plastic Foam Predictions 105
4.6. Conclusions 107

5. Conclusions and Future Work 109
5.1. Summary 109
5.2. Conclusions 110
5.3. Recommendations and Future Work 113
5.4. Final Comments 115

Appendix A. 118
A.1. Evaluation of the Effective Foam Response w/ the Maxwell stress 118
Vita 130

List of Tables

1.1. Characteristic properties, resulting applications, and necessary product forms for metal foams, Korner and Singer (2000). 8

List of Figures

1.1. A liquid foam, soap froth, Weaire and Hutzler (1999). 2

1.2. The microstructure of different natural foam systems as shown in Gibson and Ashby (1997): (a) cork, (b) balsa, (c) sponge, (d) cancellous bone, (e) coral, (f) cuttle fish bone, (g) iris leaf, (h) stalk of a plant. 3

1.3. The structures of different cellular solids as shown in Gibson and Ashby (1997): (a) open-cell polyurethane, (b) closed-cell polyethylene, (c) nickel, (d) copper, (e) zirconia, (f) mullite, (g) glass, (h) a polyether foam with both open and closed cells. 4

1.4. Examples of food foams from Gibson and Ashby (1997): (a) bread, (b) meringue, (c) chocolate bar, (d) junk food crisp, (e) Malteser, (f) Jaffa cake 5

1.5. *SEM* pictures showing the cellular structure of cancellanous bone from Gibson and Ashby (1997): (a) low density femoral head specimen, (b) high density femoral head specimen, (c) a femoral condyle specimen Gibson and Ashby (1997). 6

1.6. Synthesis of metallic open-cell foams as shown in Yamada et al. (2000). 7

1.7. The compressive stress-strain curves for foams with elastic, elastic-plastic, and brittle cell wall material as shown in Gibson and Ashby (1997). (a) an elastomeric foam, (b) an elastic-plastic foam, and (c) an elastic-brittle foam. 9

1.8. The typical response of a foam system, Weaire and Hutzler (1999). 10

1.9. Some of the possible structures in 2D foam systems, Gibson and Ashby (1997): (a) AL honeycomb foam, (b) paper-phenolic resin honeycomb foam, (c) ceramic with square cells, (d) ceramic foam with triangular cells. 15

1.10. Cubic unit open cell for foam modeling, Gibson and Ashby (1997). 16

1.11. Representation of the open-cell microstructure in foam systems with the gravity effects that help form the structure, Weaire and Hutzler (1999). 17

2.1. Representation of the open cell microstructure in foam systems, (Weaire and Hutzler, 1999). 26

2.2. Schematic of the global, continuum view and the local, cellular structural view for foam material specimens much larger than the size of the cells. The macroscopic fields such as $\mathbf{u}$ and $\mathbf{F}$ prescribed at point $\mathbf{X}$ are trickled down to the microstructure to the midpoints of the ligaments. The vertex of each unit cell is allowed to move an additional amount $\boldsymbol{\chi}$ resulting in non-affine deformation within the microstructure. . 28

2.3. Depiction of the kinematic assumptions for a 4-ligament unit cell showing the reference and deformed cell configurations. Keep in mind that each unit cell is composed with only half of the length of each ligament since each ligament is shared by two adjacent cells in the cellular microstructure. All ligament midpoints move with the specified macroscopic affine field $\mathbf{u}(\mathbf{X}, t)$, while the central vertex may have the additional displacement of $\boldsymbol{\chi}(\mathbf{X}, t)$. Note that if $\boldsymbol{\chi} = 0$ the cell motion is affine which corresponds to the position indicated by the dashed lines. 30

2.4. Schematic of the localization of bending at the unit cell vertex allowing the ligaments to remain straight during deformation. 31

2.5. (a) Four ligament unit cell and (b) unit cell with its dual tetrakaidecahedron representative volume, (Wang and Cuitiño, 2000). 48

2.6. The effects of strain rate on visco-elastic open-cell foams. (a) Predicted effective response. (b) Effective response after evaluation of the Maxwell stress which is identified as the plateau or collapse stress. The other microstructural parameters were held constant: Young's Modulus $(E) = 1.0 \times 10^9 \frac{N}{m^2}$, Foam density $(\rho) = 100.0 \frac{Kg}{m^3}$, cell ligament viscosity $(\eta) = 1000.0 \frac{N \cdot s}{m^2}$, cell ligament radius $(r) = 0.34\ mm$, cell ligament length $(L) = 1.0\ mm$. 52

2.7. The effects of strain rate on foams without viscosity (purely microinertial effects). (a) Predicted effective response. (b) Effective response after evaluation of the Maxwell stress which is identified as the plateau or collapse stress. The other microstructural parameters were held constant: Young's Modulus $(E) = 1.0 \times 10^9 \frac{N}{m^2}$, Foam density $(\rho) = 100.0 \frac{Kg}{m^3}$, cell ligament viscosity $(\eta) = 0.0 \frac{N \cdot s}{m^2}$, cell ligament radius $(r) = 0.34\ mm$, cell ligament length $(L) = 1.0\ mm$. 53

2.8. The effects of strain rate on viscous but massless foams (e.x. zero microinertial effect). (a) Local predicted effective response. (b) Effective response after evaluation of the Maxwell stress (the plateau or collapse stress). The other microstructural parameters were held constant: Young's Modulus (E) = $1.0 \times 10^9 \frac{N}{m^2}$, Foam density ($\rho$) = 0.0 $\frac{Kg}{m^3}$, cell ligament viscosity (η) = 1000.0 $\frac{N \cdot s}{m^2}$, cell ligament radius (r) = 0.34 mm, cell ligament length (L) = 1.0 mm. 54

2.9. Effect of the strain rate for non-viscous foam materials. The foam density ρ was varied as shown in the graphs but all other variables were held constant: Foam Young's modulus (E) = $1.0 \times 10^9 \frac{N}{m^2}$, Cell ligament viscosity (η) = 0 $\frac{N \cdot s}{m^2}$, Cell ligament radius (r) = 0.3 mm, Cell ligament length (L) = 1.0 mm. P_o and Δ_o were evaluated with foam density $\rho = 0$ and ligament viscosity $\eta = 0$. (a) Collapse stress P_c normalized by the static collapse stress P_o. (b) Plateau strain range Δ_p normalized by the static plateau strain range Δ_o. 55

2.10. Effect of the strain rate for viscous but massless foam materials. The solid ligament viscosity η was varied as shown in the graphs but all other variables were held constant: Foam Young's modulus (E) = $1.0 \times 10^9 \frac{N}{m^2}$, Foam density ($\rho$) = 0 $\frac{Kg}{m^3}$, Cell ligament radius (r) = 0.3 mm, Cell ligament length (L) = 1.0 mm. P_o and Δ_o were evaluated with foam density $\rho = 0$ and ligament viscosity $\eta = 0$. (a) Collapse stress P_c normalized by the static collapse stress P_o. (b) Plateau extent Δ_p normalized by the static plateau range Δ_o. 56

2.11. Effects of relative density ρ_r on the effective response of open-cell foams with zero viscosity. To obtain these results the relative density ρ_r was varied trough the ligament radius r and length L and the other parameters remained constant at: Ligament viscosity (η) = 0.0 $\frac{N \cdot s}{m^2}$, Foam density (ρ) = 100 $\frac{Kg}{m^3}$, Ligament Young's modulus (E) = $1.0 \times 10^9 \frac{N}{m^2}$. (a) Effective predicted response for varying relative density. (b) Effective response w/ the plateau stress(= Maxwell stress). 57

3.1. Cellular Structure of Metallic Open-Cell Foams. 62

3.2. Depiction of the local kinematic evolution of the length of each half ligament $\mathbf{l}^i$ and the angle between any two ligaments ψ^{ij}. The axial strain for any ligament i is defined as $\epsilon^i = log(\lambda^i) = log(\frac{l^i}{L^i})$ and the change in angle between any two ligaments i and j is defined as $\alpha^{ij} = \psi^{ij} - \Psi^{ij}$. 66

3.3. The axial constitutive behavior of the struts composing each unit cell of an open-cell metallic foam as predicted by Eqn. (3.11), Eqn. (3.12), and Eqn. (3.13). The variables in Eqn. (3.11), Eqn. (3.12), and Eqn. (3.13) were taken as *initial initial length* $L_o = 1.0mm$, *initial strut radius* $r_o = 0.3mm$, $E = 50.0Gpa$, $\sigma_{yo} = 50.0Mpa$, *exponent* $r = 4$, *axial exponet* $m = 4$, $\epsilon_p^o = 0.005$, $\dot{\epsilon}_p^o = 0.10$ (a)The loading axial constitutive response for tensile loading. (b)The axial constitutive response for loading and unloading for both tensile and compressive loading. 71

3.4. The bending constitutive behavior of the struts composing each unit cell of an open-cell metallic foam as predicted by Eqn. (3.21), Eqn. (3.22), and Eqn. (3.23). The variables in Eqn. (3.21), Eqn. (3.22), and Eqn. (3.23) were taken as *initial length* $L_o = 1.0mm$, *initial strut radius* $r_o = 0.3mm$, $E = 50.0Gpa$, $\sigma_{yo} = 50.0Mpa$, *exponet* $r = 4$, *exponent* $m = 20$, $\alpha_p^o = 0.005$, $\dot{\alpha}_p^o = 0.10$ (a)The loading bending constitutive response for tensile loading. (b)The bending constitutive response for loading and unloading for both tensile and compressive loading. 73

3.5. The predicted evolution of the unit cell configuration during compressive loading The variables in Eqns. (3.11 - 3.13) and Eqns. (3.21 - 3.23) were set to *initial strut length* $L_o = 1.0mm$, *initial strut radius* $r_o = 0.3mm$, $E = 50Gpa$, $\sigma_{yo} = 50Mpa$, *axial exponent* $r = 4$, *axial exponet* $m = 4$, $\epsilon_p^o = 0.005$, $\dot{\epsilon}_p^o = 0.10$, *bending exponet* $r = 4$, *bending exponent* $m = 20$, $\alpha_p^o = 0.005$, $\dot{\alpha}_p^o = 0.10$ 74

3.6. The effective response for foams with elastic cell walls. The values for the variables in Eqns. 3.11-3.13 and Eqns. 3.21-3.23 were set to *initial initial length* $L_o = 1.0mm$, *initial strut radius* $r_o = 0.3mm$, $E = 10Gpa$, $\sigma_{yo} = 0.5Gpa$, *axial exponent* $r = 1$, *axial exponet* $m = 1$, $\epsilon_p^o = 0.005$, $\dot{\epsilon}_p^o = 0.10$, *bending exponet* $r = 1$, *bending exponent* $m = 1$, $\alpha_p^o = 0.005$, $\dot{\alpha}_p^o = 0.10$ (a) The effective cell and plateau response for foams composed from struts with a high initial yield stress such that the response doesn't involve any plastic deformation. (b) The load and unload response when the cell walls (struts) don't undergo any plastic deformation. 75

3.7. The effective response for foams with elasto-plastic cell walls. The values for the variables in Eqns. 3.11-3.13 and Eqns. 3.21-3.23 were set to *initial strut length* $L_o = 1.0mm$, *initial strut radius* $r_o = 0.3mm$, $E = 50Gpa$, $\sigma_{yo} = 50Mpa$, *axial exponent* $r = 4$, *axial exponet* $m = 4$, $\epsilon_p^o = 0.005$, $\dot{\epsilon}_p^o = 0.10$, *bending exponet* $r = 4$, *bending exponent* $m = 20$, $\alpha_p^o = 0.005$, $\dot{\alpha}_p^o = 0.10$ (a) The effective cell and plateau response for foams composed from struts with low initial yield stress such that the response involves a lot of plastic deformation. (b) The load and unload response when the cell walls (struts) undergo plastic deformation. 76

3.8. The effect of initial yield stress on the response of metallic, open-cell foams. The foam density was taken as $100Kg/m^3$ and every run was carried out at a strain rate of $1s^{-1}$. The values for the variables in Eqns. 3.11-3.13 and Eqns. 3.21-3.23 were set to *initial strut length* $L_o = 1.0mm$, *initial strut radius* $r_o = 0.3mm$, $E = 50Gpa$, *axial exponent* $r = 4$, *axial exponet* $m = 4$, $\epsilon_p^o = 0.005$, $\dot{\epsilon}_p^o = 0.10$, *bending exponet* $r = 4$, *bending exponent* $m = 20$, $\alpha_p^o = 0.005$, $\dot{\alpha}_p^o = 0.10$ (a) The effective cell response (solid line) and the effective plateau (dashed line) for foams composed of struts with different initial yield stress σ_{yo}. (b) The effect of the initial yield stress σ_{yo} on the predicted effective plateau stress for metallic open-cell foams. . 77

3.9. The effect of applied strain rate on the response of metallic, open-cell foams. The foam density was taken as $100Kg/m^3$ and the values for the variables in Eqns. 3.11-3.13 and Eqns. 3.21-3.23 were set to *initial strut length* $L_o = 1.0mm$, *initial strut radius* $r_o = 0.3mm$, $E = 50Gpa$, $\sigma_{yo} = 50Mpa$, *axial exponent* $r = 4$, *axial exponet* $m = 4$, $\epsilon_p^o = 0.005$, $\dot{\epsilon}_p^o = 0.10$, *bending exponet* $r = 4$, *bending exponent* $m = 20$, $\alpha_p^o = 0.005$, $\dot{\alpha}_p^o = 0.10$ (a) The effective cell response (solid line) and the effective plateau (dashed line) for foams loaded at different strain rates $\dot{\epsilon}$. (b) The effect of the applied strain rate $\dot{\epsilon}$ on the predicted effective plateau stress for metallic open-cell foams. 78

3.10. The effect of the initial rate of plastic deformation ($\dot{\epsilon}_o^p$ *and* $\dot{\alpha}_o^p$) on the response of metallic, open-cell foams. The foam density was taken as $100Kg/m^3$, the applied strain was maintained at $1000s^{-1}$ and the values for the variables in Eqns. 3.11-3.13 and Eqns. 3.21-3.23 were set to *initial strut length* $L_o = 1.0mm$, *initial strut radius* $r_o = 0.3mm$, $E = 50Gpa$, $\sigma_{yo} = 50Mpa$, *axial exponent* $r = 4$, *axial exponet* $m = 4$, $\epsilon_p^o = 0.005$, *bending exponet* $r = 4$, *bending exponent* $m = 20$, $\alpha_p^o = 0.005$, (a) The effective cell response (solid line) and the effective plateau (dashed line) for foams loaded at different initial rates of plastic deformation. (b) The effect of initial rate of plastic deformation on the on the predicted effective plateau stress for metallic open-cell foams. 79

4.1. Schematic of the foam system as a continuum body with prescribed boundary conditions and initial conditions. 84

4.2. Schematic representation of the spatially discretized continuum body. Each element is assigned a number e and every node is assigned a number n. 87

4.3. a) Continuum and microstructural view of foam material composed of very small cells relative to the sample size. The macroscopic fields such as $\mathbf{u}$ and $\mathbf{F}$ prescribed at point $\mathbf{X}$ are trickled down to the microstructure to the midpoints of the ligaments. b) Kinematic assumptions for a 4-ligament unit cell showing the reference and deformed cell configurations. The cell deforms according to the prescribed macroscopic affine field $\mathbf{F}$ and all ligament midpoints move with the specified macroscopic affine field $\mathbf{u}$, however the cell vertex may have the additional displacement $\boldsymbol{\chi}$ resulting in non-affine deformation within the microstructure. 92

4.4. Simulation of impact at a constant downward velocity of $v = 10.0\frac{m}{s}$ on a visco-elastic foam material. The foam is homogeneous and composed of the unit cell described in the section 2.4.1. The foam density was taken as $\rho = 75.0\ \frac{Kg}{m^3}$ and the ligaments of every cell in the microstructure had the properties: ligament Young's Modulus (E) $= 7.5 \times 10^8$ Pa, ligament viscosity (η) $= 10.0\ \frac{N \cdot s}{m^2}$, ligament radius ($r$) $= 0.3\ mm$, ligament length (L) $= 1.0\ mm$. (a) Visco-elastic foam specimen in its initial state along with the region selected for finite element analysis. (b) Vertical Piola Stress P_{33} normalized by the Young's Modulus (E) vs. vertical strain ϵ_{yy} response evaluated at the top surface. 100

4.5. Snapshot taken at different times corresponding to different average vertical strains during the dynamic compression of the 2D visco-elastic foam sample described in Figure 4.4. Colors represent the local deformation in the vertical direction. The black lines describe the FEM mesh, not the lattice. The snapshots clearly show the transition from (nearly) homogeneous deformation to heterogeneous deformation (mixture of collapsed and un-collapsed phases) and back to nearly homogeneous (completely collapsed) phase. 101

4.6. Snapshots taken at different times corresponding to different average vertical strains during the dynamic compression of the 2D visco-elastic foam sample described in Figure 4.4. Colors represent the local strain rate in the vertical direction. The black lines describe the FEM mesh, not the lattice. The snapshots show the variation of the local strain vertical strain rate throughout the foam specimen as it is being loaded with a constant downward velocity at the top surface. The snapshots clearly show the variation of the strain rate before collapse, during collapse and after collapse. 103

4.7. Comparison of the strain and strain rate for the 36% average vertical strain snapshots in Figures 4.5d and 4.6d. (a) Variation of the local vertical strain. (b)Variation of the local vertical strain rate. 104

4.8. Simulation of impact at a constant downward velocity of $v = 10.0m/s$ on a homogeneous *elasto-plastic* 2D open-cell foam specimen with a *high initial yield stress* resulting in a small amount of plastic deformation. The snapshots were taken at different times corresponding to different average vertical strains during the dynamic compression. Colors represent the local deformation in the vertical direction and the black lines describe the FEM mesh. The snapshots clearly demonstrate the transition from (nearly) homogeneous deformation to heterogeneous deformation (mixture of collapsed and un-collapsed regions) and back to nearly homogeneous (completely collapsed) deformation. 106

4.9. Simulation of impact at a constant downward velocity of $v = 10.0m/s$ on a homogeneous *elasto-plastic* 2D open-cell foam specimen with a *low initial yield stress* resulting in a large amount of plastic deformation. The snapshot were taken at different times corresponding to different average vertical strains during the dynamic compression. Colors represent the local deformation in the vertical direction and the black lines describe the FEM mesh. The snapshots clearly demonstrate the transition from (nearly) homogeneous deformation to heterogeneous deformation (mixture of collapsed and un-collapsed regions) and back to nearly homogeneous (completely collapsed) deformation. 107

5.1. Depiction of metallic open-cell foams across the scales. 117

A.1. Evaluation of the macroscopic, effective foam specimen response from the micromechanical effective response during uniaxial dynamic compression. a) The compressive uniaxial First Piola-Kirchoff stress P_{33} normalized by the Youngs Modulus E plotted versus the uniaxial strain λ. The red/solid line represents the local micromechanical response and the green/dashed line represents the evaluated effective response with the Maxwell stress as the plateau stress. b) The elastic $\mathcal{W}$ plus viscous $\mathcal{D}$ energy potentials normalized by the Youngs Modulus E plotted against the uniaxial strain λ. The red/solid line represents the potential energy evolution with the non-convex region between strains λ^- and λ^+. The green/dashed line represents the convexified energy landscape where the non-convex region has been replaced by a linear approximation. 119

Chapter 1

Introduction

Foams are light weight cellular materials which can be conceptualized by the repetition of a particular unit cell. This unit cell can have a myriad of shapes and sizes as long as its mirror duplications can be fitted into a lattice arrangement to reproduce the cellular material. It appears that nature has always known about the advantages of cellular materials because they are found in plants, animals, and humans. Over the years, mankind has learned about the many properties offered by these materials and has began to take advantage of them in different applications. Industrial and scientific interest in the field of foams has grown significantly over the last couple of years with the advent of novel foam manufacturing processes. The work presented in this dissertation contributes to the understanding of the intriguing mechanical behavior exhibited by visco-elastic and elasto-plastic open-cell solid foam materials. This chapter presents an introduction to the field of foam materials and an overview of the work contained in this dissertation. First, Section 1.1 will give an introduction to the general field of foam materials. Next, Section 1.2 will present a concise review of the relevant experimental and modeling studies on the mechanics of solid foam materials. Lastly, Section 1.3 will present an overview of the work presented in the different chapters of this dissertation.

1.1 Introduction to Foams

Foam materials are not exclusively solids, liquids, or gases; they are made with solid or liquid cells which entrap a fluid within the solid or liquid microstructure combining properties and characteristics of multiple states of matter Perkowitz (2000). The vast field of natural and man-made foam materials is divided into liquid and solid cellular materials. The soap froth shown in Figure 1.1 is a well known example of a liquid foam

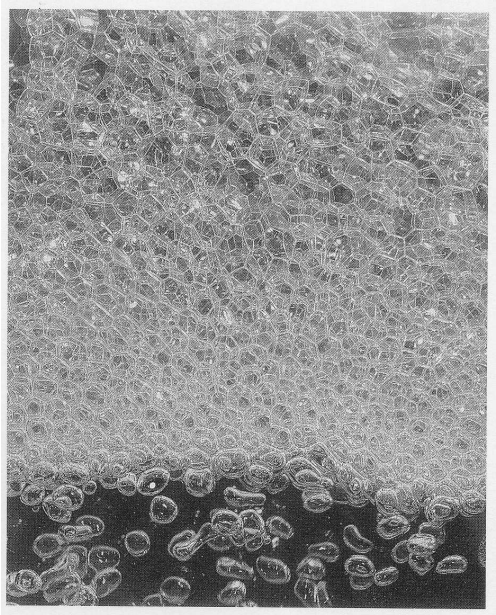

Figure 1.1: A liquid foam, soap froth, Weaire and Hutzler (1999).

because the walls, the membranes, of the spherical cells making up the froth are in the liquid state. Probably the most familiar solid cellular materials are the polymeric foams used in packaging to protect delicate and fragile products from impact during transportation.

Considering all liquid and solid cellular materials results in a vast field of foam materials. The field of solid foam materials alone can be larger than the composites field when wood is included. Many of the materials that we frequently encounter in our everyday lives such as coffee cups, cakes, cereals, snacks, whipped cream, cappuccino foam, beer foam, wood, cork, bone, packaging cushioning foams, sofa foams, mattress foams, honeycombs, etc have cellular structures and thus qualify as foams. Solid cellular-structured materials have existed naturally for many years in woods, human tissue such as cancellous bone, honeycomb structures, sponge, and coral. Figure 1.2 shows some of the different foam materials that exist naturally in world. Nowadays the number of man-made cellular materials is much larger than the number of natural cellular materials. At some point many of us have come across polymeric foams but as can be deduced from figure 1.3, many other materials such as metals, glasses, and ceramics

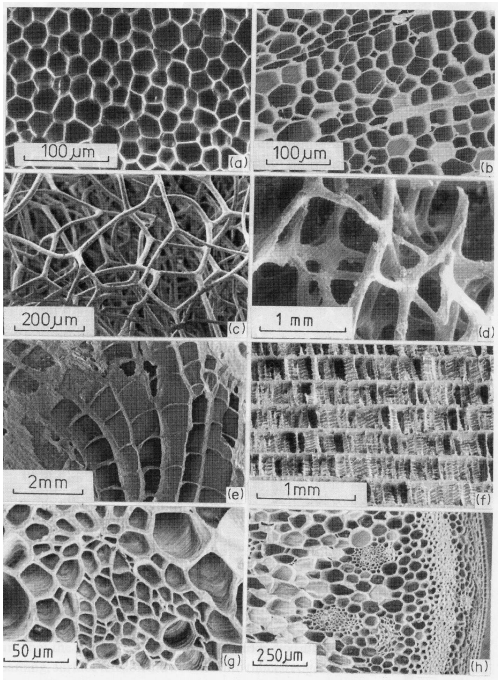

Figure 1.2: The microstructure of different natural foam systems as shown in Gibson and Ashby (1997): (a) cork, (b) balsa, (c) sponge, (d) cancellous bone, (e) coral, (f) cuttle fish bone, (g) iris leaf, (h) stalk of a plant.

which the general public is not used to seeing as foams are being synthesized as foams with different cellular structures. As can be seen from Figure 1.3, man-made solid foams have a wide range of open-cell and closed-cell cellular structures. Solid cellular materials are becoming more common because they are starting to be found everywhere. For instance solid cellular structured materials are found in foods (breads, cereals, snacks), the human body, resting equipment/furniture (chairs, sofas, mattresses), ships, aircraft, packaging materials, sports equipment (helmets, shoes), etc. Figures 1.4 and 1.5 show the cellular structure of different food foams and cancellous bone respectively.

1.1.1 Synthesis of Foams

The synthesis of foam materials is an incredibly dynamic process involving the injection of a gas into a material in the liquid state. We can be amazed by carefully observing the commonplace nucleation and self-organization of the bubbles whenever someone pours a beer into a glass or brews a cappuccino into a cup (Weaire and Hutzler, 1999;

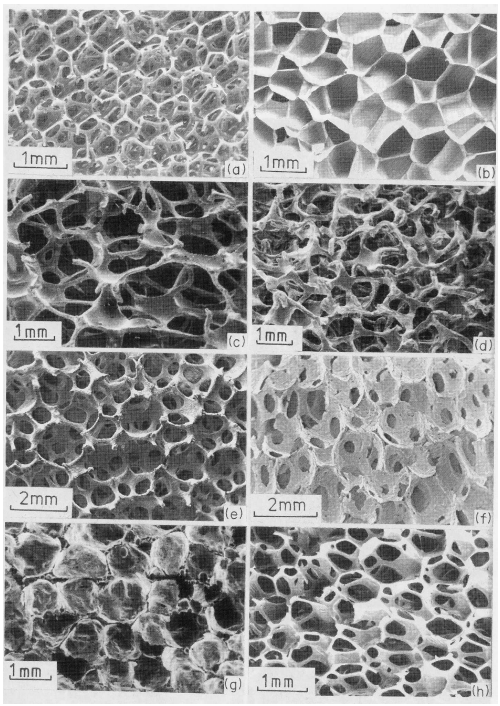

Figure 1.3: The structures of different cellular solids as shown in Gibson and Ashby (1997): (a) open-cell polyurethane, (b) closed-cell polyethylene, (c) nickel, (d) copper, (e) zirconia, (f) mullite, (g) glass, (h) a polyether foam with both open and closed cells.

Perkowitz, 2000). Man-made or artificial solid foams are essentially synthesized by generating air voids in a melt and solidifying at a specific rate to produce the desired cellular structure and material properties. The different processing routes including gas injection into a melt, immersion of gas releasing blowing agents into a melt, and pouring the melt into a removable mold have been reviewed by authors such as Banhart (2003), Gibson (2000), Ashby et al. (2000) and Gibson and Ashby (1997). There are two basic methods for manufacturing cellular solids on which almost all the current cellular material fabrication techniques are based. The first is a self-forming method which inserts a gas into the material in the liquid state. The liquid is often treated with additives to increase the material's viscosity and to decrease its surface energy in order to minimize the drainage of the liquid and to stabilize the cell walls at a desired point in the foaming process. Once the material is solidified at the desired point, we have a new cellular-structured solid. The second method uses molds with the desired cellular structure to pour the material in the liquid state and once the

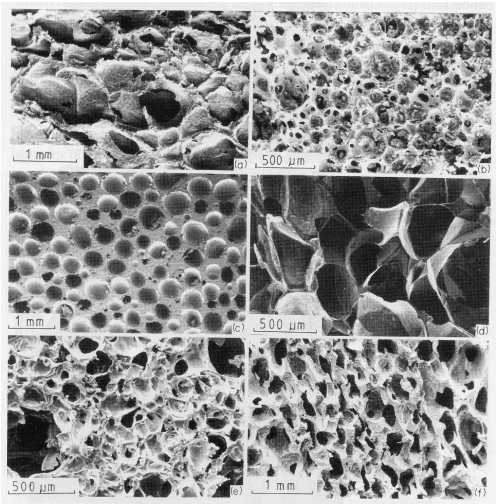

Figure 1.4: Examples of food foams from Gibson and Ashby (1997): (a) bread, (b) meringue, (c) chocolate bar, (d) junk food crisp, (e) Malteser, (f) Jaffa cake .

material solidifies in the mold's shape; the mold is burned away or chemically removed. Figure 1.6 depicts the mold process used to generate metallic foams. Using variations of these synthesis techniques, many efforts have and are being directed at foaming metals, ceramics, polymers, glasses and other materials in efforts to create foam materials with properties that can be exploited in different applications. Some of the more recent and exotic cellular solids being synthesized include syntactic foams (Erikson, 1999) and magnetic foams (Boonyongmaneerat et al., 2007).

1.1.2 Structure of Foams

The different processing routes and the properties of the material being foamed produce solid foam materials with either open- or closed-cell cellular structures. Earlier Figure 1.3 showed a couple of solid foam materials with either open- or closed-cell cellular structures. A cellular material with cells that are completely closed, such as foams composed of hollow spherical cells, is considered a closed-cell foam because the fluid, such as air, trapped in each cell is restricted to that cell. In closed-cell foams, there is no fluid flow across the foam's cellular structure without breakage of the cell walls. On the other hand, open-cell foams allow fluid flow throughout the cellular structure. The cellular architecture of open-cell foams resembles a labyrinth of small,

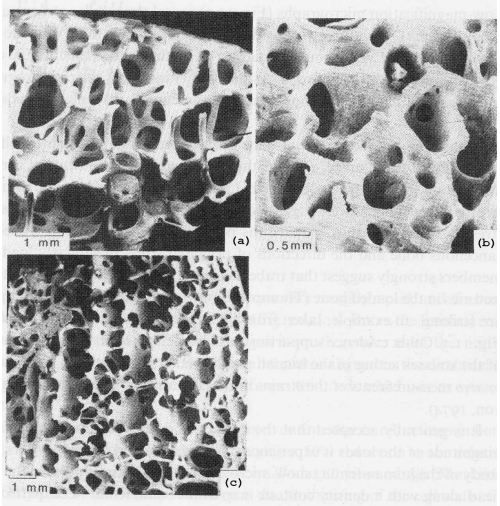

Figure 1.5: *SEM* pictures showing the cellular structure of cancellanous bone from Gibson and Ashby (1997): (a) low density femoral head specimen, (b) high density femoral head specimen, (c) a femoral condyle specimen Gibson and Ashby (1997).

interconnected trusses. In reality many cellular solids have cellular structures in between open- and closed-cell where many of the cells show characteristics of both types. The work presented here concentrates on open-cell foams which we model as a network of interconnected ligaments surrounded by air-filled voids.

1.1.3 Properties of Foams

Man-made solid cellular materials inherit their properties from the cellular architecture resulting from the synthesis process along with the material properties of the solid cell wall. Solid foam materials can have properties such as very low densities, very low thermal conductivities, moderate to small stiffness, negative Poisson's ratios, large deformation ability, very high strength to weight ratios, high damping coefficients, high friction coefficients, very large energy absorption capacity and increased moments of inertia. Table 1.1 shows the properties, applications, and products that can come out of Aluminum metallic foams. Table 1.1 corresponds to just one type of foam, Aluminum foam, if we realize that we can make foams out of many other materials such as polymers, ceramics, glasses, and other metals, one can start to imagine the enormous number of material properties that we can have at our disposal through solid foams.

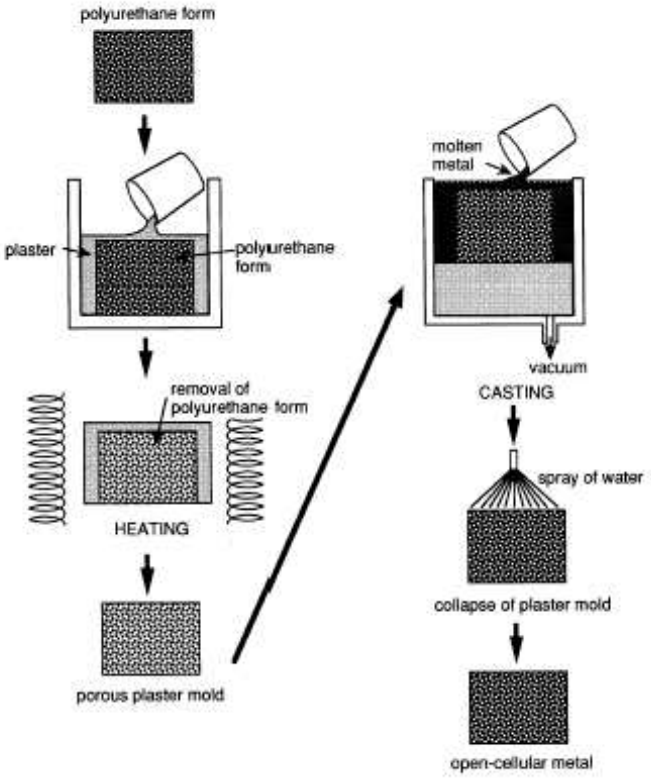

Figure 1.6: Synthesis of metallic open-cell foams as shown in Yamada et al. (2000).

1.1.4 Applications of Foams

Many enterprises such as automotive, aircraft, and rail transportation, as well as the electronic, food, and packaging industries are envisioning applications for cellular solids especially in fields requiring strong, lightweight materials, capable of handling dynamic loads. Foam materials are preferable in many engineering applications requiring mitigation of the adverse effects of sudden impact loading which can result in injuries to soft tissue and/or degradation of personnel and property shields. Cellular solids such as visco-elastic and elasto-plastic open-cell foams can offer the benefits of light weight and sufficient strength along with the ability to absorb impact energy through dissipation mechanisms appearing in the large deformation regime during cellular structure collapse. However, it is through their wonderful combinations of properties that cellular solids offer the greatest potential for applications (Korner and Singer, 2000) because

Property	Application	Product form
High specific bending stiffness and strength	-stiff and super light-weight panels for transport and architecture	-Shaped parts -(Sandwich) panels -3D-shaped (Sandwich) panels
Isotropic absorption of impact energy at a nearly constant low stress level	-Impact energy absorption components in cars -Packaging -Blast protection	-Shaped parts -Large panels
Good sound absorption, electromagnetic shielding, and vibration damping	-Self-supporting wall panels -Housing for electronic devices -Machine casing for sound absorption -Soundproof walls along railway tracks and roads	-Large panels -Sandwich panels
High thermal stability and low thermal conductivity	-Heat shields	-Large panels
Decorative, non-combustible, weather resistant	-Furniture -Wall panels	-Large panels -Shaped parts
Light-weight	-Sand core replacement -Floating structures	-Complex shaped parts with a dense surface skin
High inner surface	-Compact heat exchangers -Catalyst support -Cyrogenic applications	-Complex open-cell parts

Table 1.1: Characteristic properties, resulting applications, and necessary product forms for metal foams, Korner and Singer (2000).

nowadays, industries usually need to satisfy more than one property in a certain material application, it's here that people see the greatest potential for foam materials. The varied combinations of material properties offered by cellular solids make them advantageous in applications such as thermal insulation, packaging/transportation of fragile/dangerous products/materials, structural applications with high strength to weight ratios requirements, flotation/buoyancy, filtering, sound insulation, etc (Gibson and Ashby, 1997; Friis et al., 1988).

1.1.5 Typical Mechanical Behavior

Nowadays, due to the advent of novel synthesis processes almost every type of solid material can be transformed into a cellular solid. The resulting diversity of solid foam materials still exhibit a typical response even though the fundamental physics at cell wall level can be very different depending on the properties of the solid phase material.

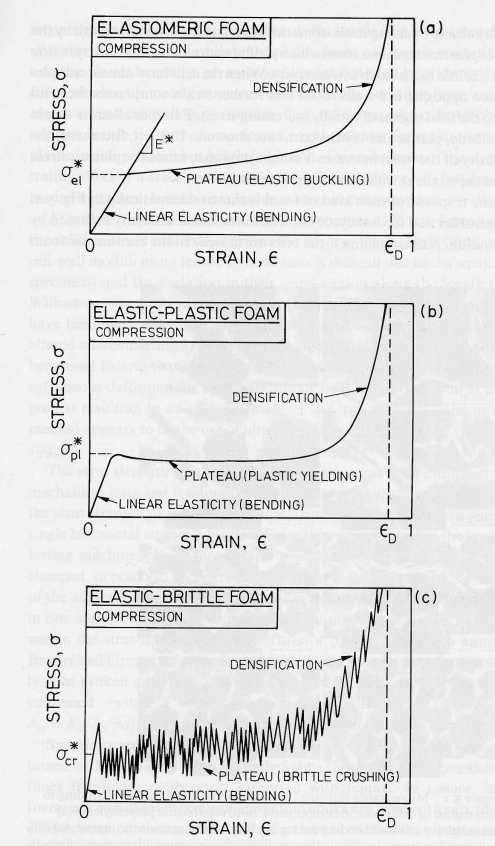

Figure 1.7: The compressive stress-strain curves for foams with elastic, elastic-plastic, and brittle cell wall material as shown in Gibson and Ashby (1997). (a) an elastomeric foam, (b) an elastic-plastic foam, and (c) an elastic-brittle foam.

The characteristic mechanical behavior of a particular foam system depends heavily on the topology of the cellular structure in addition to properties of the solid making up the cell walls Gibson and Ashby (1997). The microstructure in different cellular material can have very distinct properties because the cell walls can be made from almost any type of material. In addition, the geometry of the microstructure can be very different from one foam system to the next because the shape and size of the cells can change drastically depending on the implemented synthesis method. The large range of microstructural properties and geometries results in many inherently different mechanical responses in foam systems but still maintaining a typical pattern.

Figure 1.7 shows the typical response of cellular solids whose cell walls are made from (a) elastic, (b) plastic, or (c) brittle material. Even though the stress values can

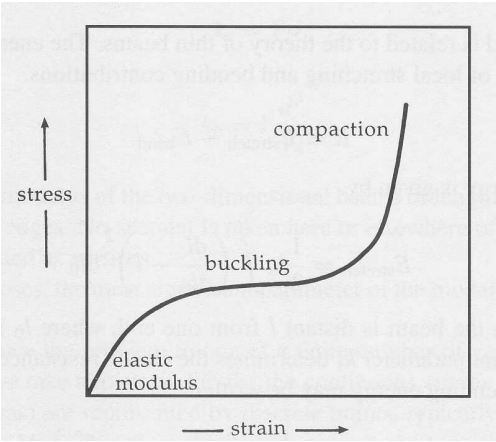

Figure 1.8: The typical response of a foam system, Weaire and Hutzler (1999).

vary enormously for the different kinds of foams, we have a good understanding of the typical pattern exhibited by the stress vs. strain curve for all solid foam systems. As shown in figure 1.8 if we were to compress a cellular solid it would result in the typical behavior where first we would observe a portion of initial elastic behavior, then we would observe a constant stress (plateau stress) portion which happens when the cell walls collapse, finally we would observe a densification portion where the collapsed cells are further compressed almost as a bulk solid and the stress increases very rapidly. The typical deformation of a foam system results in a very long strain range because very large deformations occur during the collapse portion.

1.2 Review of Relevant Previous Works

Learning about the synthesis, cellular structure, physics, and properties of foam systems seems to have captured the interest of some of the early great scientists. Robert Hooke gave the name "*cell*" to the repetitive shape that makes up the cellular material when he observed the cellular structure of cork wood using a microscope (*Micrographia*, 1664). William Thompson, Lord Kelvin, came up with the polyhedral tetrakaidecahedron as the cell which minimized the area of the cell wall material for the most efficient foam structure Thompson (1961). Joseph Antoine Ferdinand Plateau did work which helped in the understanding of soap films, bubbles and foams establishing rules for the

connectivity of the cells in a foam system Plateau (1873). Over the years, the arrangement and behavior of foam systems has caught the attention of so many people that even the idea that continents and galaxies are organized similar to foam systems has been considered Perkowitz (2000).

1.2.1 Pioneering Mechanics Works

The very interesting processes that occur in the mechanical response of solid foams has motivated scientists to perform varied experimental and theoretical studies to understand the behavior. The majority of the studies on foam mechanics have been done under quasi-static loading conditions. These pioneering works have been introduced by a number of research groups, most of which have been collected in the book on cellular solids Gibson and Ashby (1997) and the book on cellular plastics Hilyard (1982) and in reviews such as Kraynik and Warren (1994), Zhu et al. (1997b), Mills (2000), Han et al. (1998), and Zhang et al. (1998). These studies have generated substantial knowledge which has established much of the current theory and characterization of the behavior of cellular solids. Some of the more notable groups which have contributed pioneering works include Gibson and Ashby (1982); Dement'ev and Tarakanov (1970, 1973); Chen et al. (1994); Chen and Lakes (1996); Tyler and Ashby (1986); Deshpande et al. (2001); Deshpande and Fleck (2000a,b, 2001); Evans et al. (2001); Kraynik et al. (1997); Warren and Kraynik (1997). These works have provided insights on the compressive strength, tensile strength, Young's Modulus, the deformation mechanisms, and the typical stress vs. strain curve of solid foams.

1.2.2 Recent Work

More recently, experimental and modeling studies have concentrated on the different stages of deformation as well as on the effect of the cell wall properties on the macroscopic response of open-cell foams, for instance Papka and Kyriakides (1998); Gong et al. (2005); Gong and Kyriakides (2005); Zhou et al. (2004a,b); Zhou and Soboyejo (2004); Lee et al. (2003, 2006b,a). Also, due to the renewed interest in utilizing foams

for energy absorption applications, there has been a number of experimental studies focusing on the dynamic response of foam systems, including Chen et al. (2002); Tedesco et al. (1993); Rinde and Hoge (1971); Nagy et al. (1974); and especially for metallic foam materials, Deshpande and Fleck (2000a); Mukai et al. (1999a,b); Shimojima et al. (2001); Dannemann and Lankford (2000); Kanahashi et al. (2001, 2000); Yi et al. (2001); Han et al. (1998); Hall et al. (2000).

1.2.3 Dynamic Loading

The quasi-static response of foam systems has been well-studied, however the majority of foam materials being considered for future and/or potential applications will be put to use in dynamic loading environments, many times at very high strain rates. Additionally, many interesting changes occur to the mechanical behavior of foam systems under dynamic loading situations relative to the quasi-static response. As a result there is a need to obtain an improved understanding of the dynamic response of foam systems. The current quasi-static literary works don't provide the necessary understanding for dynamic loading applications at exceedingly high strain rates (Mills and Gilchrist, 1991; Fuganti et al., 2000; Gilchrist and Mills, 1994). Different researchers have performed studies on different types of helmets (Gilchrist and Mills, 1994; Mills and Gilchrist, 1991) to investigate ways to make them more protective to users such as cyclist, football and baseball players, constructions workers etc. Others researchers (Loveridge and Mills, 1993; Gibson and Ashby, 1997) have studied packaging systems where high velocity, impact type loading happens during transportation. A more effective approach to improve these current applications is to dedicate our efforts to understanding the cellular materials employed in these helmets, packages, bumpers, foods, resting equipment and vest, since it is these foam systems which absorb the energy from the impact. To date, very little work has been done in the field of solid foams to study the dynamic mechanical behavior and to develop dynamic numerical models for dynamic loading analysis. Recently experiments have been done to learn about the strain rate and relative density effects Mukai et al. (1999a,b); Kanahashi et al. (2001, 2000, 2002); Deshpande and Fleck (2000a); Shimojima et al. (2001); Chen et al. (2002); Tedesco et al. (1993) on the

mechanical response of dynamically loaded solid foam materials.

Strain Rate Dependency

Rinde and Hoge (1971) studied the compressive strength of rigid polystyrene foams at room temperature as a function of strain rate and showed that the strength increases only slightly with strain rate. Similar conclusions were reached by Nagy et al. (1974). Tyler and Ashby (1986) found that if a flexible polyurethane foam was filled with a viscous water-glycerin the plateau strength exhibited a remarkable strain rate dependence at low strain rates $(0.002\ to\ 20)s^{-1}$. Lankford and Dannemann (1998); Dannemann and Lankford (2000) reported that the strain rate dependence was negligible for a low density open-celled Aluminum foam and the effect was more apparent for higher density foams. Mukai et al. (1999a) reported recently that the plateau stress of a close-celled aluminum, ALPORAS, exhibited a higher strain rate sensitivity than a polystyrene foam with the same density. Yi et al. (2001) did experiments to investigate the effect of strain rate on the mechanical response and the energy-absorbing capacity of Aluminum alloy cellular solids and concluded that strength and energy absorbed increase with increasing strain rate, and that the increase is greater for higher density foams. Kanahashi et al. (2000) concluded that plateau stress normalized by the relative density and the absorbed energy drastically increased based on dynamic compression experiments ($strain\ rate = 1.4x10^3 s^{-1}$) on very low density Aluminum foams. The results are similar for Magnesium alloy foams. Higher strain rate (10^{-3} to $5000s^{-1}$) compression experiments were done by Deshpande and Fleck (2000a), however they concluded that strain rate had no effect on the plateau stress even though the Aluminum foam relative density was similar to that used in Kanahashi et al. (2000). Currently there is no general consensus on how exactly the mechanical response of cellular solids changes when they are loaded dynamically from low to very high strain rates because currently there aren't many experimental and/or numerical studies regarding the strain rate dependency of these materials. The limited available data is due in part to the lack of experimental equipment capable of impacting specimens of at high strain rates.

As you can deduce from the few literary works mentioned above, there is no

clarity on how exactly the strain rate affects the mechanical response of cellular solids. However, the majority of works do seem to agree that strain rate increases the plateau stress and that the range of the plateau does not decrease which results in a higher energy absorption capacity during dynamic loading applications. The majority of studies report that as long as we stay in the range of relative density that corresponds to foam systems without increasing it too much that we are looking a porous materials instead of foams, the increase of the plateau stress caused by the strain rate is greater as the relative density increases. The relation between the compressive stress and strain at dynamic strain rates must be well understood in order to adequately study the energy absorption capacity of cellular solids. Experimentally, the stress vs. strain behavior at fast strain rates has mostly been investigated using the split Hopkinson pressure bar (SHPB) method Deshpande and Fleck (2000a), an experimental technique widely used to study the dynamic response of structural materials. All the strain dependency, dynamic loading experimental studies mentioned here, have been done using the SHPB method. In order to perform dynamic loading test at exceedingly high strain rates i.e. $10000s^{-1}$, a new technique must be developed. An attempt is made to explain the reasons behind the experimentally-observed effects on the dynamic response of foams by employing the numerical micromechanical model presented in chapter 2.

1.2.4 Modeling

Modeling and simulating the behavior of foams is quite challenging due to unknown microstructural properties, complex microstructural geometry, extremely large deformations, and cell wall contact after collapse. One approach is to simply consider single portions of the solid cell wall; for instance a single ligament for open-cell foams or a single membrane for closed-cell foams (Christensen, 1986), (Zilauts and Lagzdin, 1992). The foam response is then predicted by averaging over the different possible orientations of the ligament or membrane. This approach however only considers axial deformation and ignores the cell connections as well as the shape and size of cells drastically reducing its validity. Another approach considers a representative unit cell that can replicate

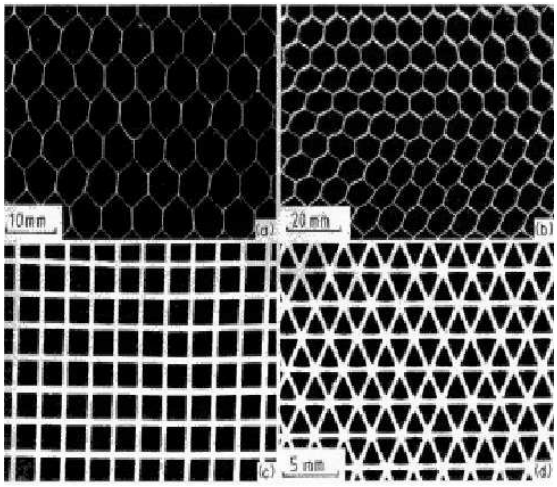

Figure 1.9: Some of the possible structures in 2D foam systems, Gibson and Ashby (1997): (a) AL honeycomb foam, (b) paper-phenolic resin honeycomb foam, (c) ceramic with square cells, (d) ceramic foam with triangular cells.

the periodic cellular structure through mirror duplications. $2D$ foams have been modeled extensively as honeycomb structures (Gibson et al., 1982; Warren and Kraynik, 1987; Overaker et al., 1998a,b), $3D$ foams have been modeled with cubic cells (Gent and Thomas, 1963; Gibson and Ashby, 1982), tetrahedral cells (Warren and Kraynik, 1988; Wang and Cuitiño, 2000), pentagonal dodecahedrons (Menges and Knipschild, 1975), and tetrakaidecahedrons (Warren and Kraynik, 1997; Zhu et al., 1997a,b). In addition to accounting for the cellular structure, this approach allows researchers to incorporation additional important modes of deformation such as bending and twisting in addition to axial deformation.

Despite the many challenges in modeling of foam mechanics, a good number of modeling/simulation studies have surfaced which have provided connections between foam cellular architecture and cell wall material response. Some of the available works are based on tetrakaidecahedral unit cell models. For example, a $3D$ open-cell foam model with periodic tetrakaidecahedral cells was presented for the purpose of studying the nonlinear response of elastic 3D-periodic microstructures Laroussi et al. (2002). The high-strain compression of open-cell foams was analyzed using a lattice model with tetrakaidecahedral cells Zhu et al. (1997b). The micromechanical dynamic modeling

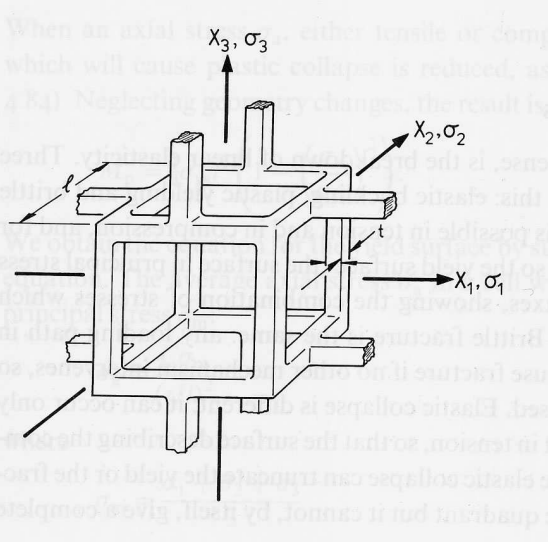

Figure 1.10: Cubic unit open cell for foam modeling, Gibson and Ashby (1997).

work presented here evolved from a previously reported quasi-static tetrakaidecahedral unit cell model Wang and Cuitiño (2000). A micromechanical model for $3D$ open-cell foams using tetrakaidecahedral cells was developed using energy methods and Castigliano's second theorem Li et al. (2003). The same group has also reported an open-cell micromechanical model for the emerging ultralightweight carbon foams Sihn and Roy (2001, 2004).

Other modeling efforts have employed the Voronoi technique. For instance, a study was done using a cubic open-cell model along with the Voronoi technique to generate the microstructure Shulmeister et al. (1998). An investigation of cell irregularity effects was performed via ABAQUS FEA and a Voronoi open-cell foam with different degrees of randomness of the cell size and shape Zhu and Windle (2002). A few models are based on continuum approaches. For example there is a visco-elastic continuum model employing ABAQUS Software Hucko and Faria (1997) and there is a Cosseret continuum modeling study on cellular solids Onck et al. (2001). Other modeling works include a comprehensive study on the effects of various geometrical imperfections on the in-plane yielding behavior of $2D$ cellular foams under biaxial loading utilizing FEA Chen et al. (1999). Another study used a modified cube as the representative unit cell

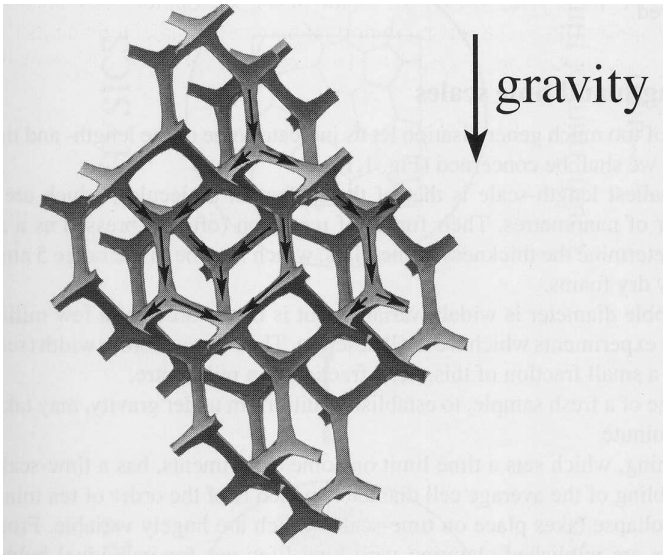

Figure 1.11: Representation of the open-cell microstructure in foam systems with the gravity effects that help form the structure, Weaire and Hutzler (1999).

to model the quasi-static crushing of closed-cell metallic foams Meguid et al. (2002). A rate-dependent elasto-plastic foam constitutive model was developed to use with LS-DYNA3D software Zhang et al. (1998). Finally, recently a version of the material point method (MPM), the Generalized Interpolation Material Point method (GIMP method), was used to analyze a small group of open cells with emphasis on the densification portion of the deformation Bardenhagen et al. (2005).

Because the unit cell that makes up a cellular solid can have a multitude of shapes, there is an enormous range of possible cellular microstructures. Of the many possible cellular structures for open-cell foams, modeling investigators tend to select honeycombs for $2D$ analysis which seems to be a good model (see figure 1.9) but the open-cube shown in figure 1.10 Gent and Thomas (1963); Gibson and Ashby (1997) used as the unit cell in many three dimensional studies does not resemble the actual cellular microstructure formed in open-cell foams very closely, see figure 1.11. The different foaming processes do not generate open-cell solid foams with cubic cellular structures because cubes are not the unit cell which provides the more stable and stronger microstructure Kusner and Sullivan (1996). A cubic cellular structure can only be generated if a mold is specifically designed to produce a cellular structure with

cubes. Based on the previous work on open-cell solid foams under the direction of prof. Alberto M. Cuitiño (Wang and Cuitiño, 2000; Wang et al., 2000), here a four column tetrahedron enclosed inside a dual tetrakaidecahedron volume element is selected as the proper unit cell to model the cellular microstructure in open-cell foams. This unit cell is more favorable foaming process and it mimics more closely the cellular microstructure observed in actual open-cell solid foams as shown in figure 1.11.

There are very few modeling studies which take into account the effects of dynamic loading Zhang et al. (1998); Laroussi et al. (2002); Hucko and Faria (1997). Furthermore, many of the available models are not very robust because some of the works have made use of commercial software to model specific aspects of foam mechanics; some have made a continuum assumption to come up with constitutive expressions for the foam behavior, and some are based on phenomenological ideas. The model presented here accounts for the effects of dynamic loading at high strain rates and can predict the overall foam response while being completely based on the cell wall material properties, the open-cell topology, and the cell wall (ligament) physics. To our knowledge there is no micromechanical formulation in the literature for dynamically loaded, open-cell, periodic cellular materials similar to the one presented here. The current formulation will provide a physical insight into the deformation process at cell wall and unit cell level while quantifying the effect of the foam structure, ligament properties, and strain-rate on the overall mechanical response. Finally, the reader is warned that many of the literary works mentioned in this introductory chapter will be mentioned again in the introduction to chapters 2, 3, and 4 in order to make each chapter self-contained.

1.3 Overview of the Dissertation

The work presented in this dissertation is organized in the following order:

- *Chapter* 1 : Background and Major Relevant Studies
- *Chapter* 2 : Formulation of the Micromechanical Model and Application to Visco-Elastic Foams

- *Chapter* 3 : Application of Micromechanical Model to Metallic Foams
- *Chapter* 4 : Implementation of Micromechanical Models for Open-cell Foams Into Nonlinear Implicit and Explicit Finite Element Analysis Schemes
- *Chapter* 5 : Summary, Conclusions and Future Work
- *Appendix* : Additional Information

The dissertation begins in *chapter* 1 with a general introduction to the field of cellular materials with an emphasis on solid foams, more specifically open-cell solid foams. There it provides a summary of the majority of pioneering scientific studies performed over the last couple of years to elucidate the intricate mechanical behavior exhibited by foam materials.

In *chapter* 2 the dissertation presents the description and formulation of a micromechanical model for dynamically loaded visco-elastic open-cell foams. The theory is based on an energy analysis of the solid microstructure through a representative $3D$ unit cell which is limited to cells with an arbitrary number of ligaments concurring at a central vertex. The formulation starts with the expression for the Lagrangian of a representative unit cell comprising an imposed macroscopic deformation. Enforcement of the principle of minimum action results in a relation between the applied deformation history and the motion of the internal vertex history, which uniquely defines the kinematic state and thus the stress state. Axial and bending deformation are incorporated at ligament level through the relocation of the unit cell vertex which is also the method trough which cell collapse is captured. By maintaining the history of global affine deformation in addition to the history of local non-affine motion of the cell vertex, the model is able to capture the microinertial effects important during dynamic loading of open-cell foam materials. The model is applied to open-cell polymeric foam with decoupled visco-elastic constitutive behavior at cell wall level. The chapter concludes with a set of predictions for visco-elastic, open-cell foams resulting from the implementation of the model into a numerical analysis code. We have selected to presents results for a compressive, uniaxial loading case because it is perhaps one of the most interesting, challenging, and technologically relevant cases to study due to the effects introduced

during the evolution of the cell collapse. It is also quite relevant from the application viewpoint due to the associated energy absorption/dissipation characteristics exhibited during the collapse. As will be shown the incorporated mechanics provides physical insights which help describe the different stages in the response of dynamically loaded open-cell foam systems.

In *chapter* 3 the dissertation presents the application of the micromechanical model developed in chapter 2 to metallic open-cell foams with elasto-plastic cell wall constitutive behavior. The key equations from the micromechanical model formulated in chapter 2 will be mentioned again in order to make the chapter self-contained. Here it is crucial to preserve the history of deformation because it dictates the future constitutive response. The history of plastic deformation is retained at ligament level to predict the succeeding axial and bending constitutive behavior while the history of cell vertex motion is maintained at cell level to account for microinertial effects during dynamic loading. The chosen cell wall constitutive relations account for the coupled elastic and viscous response of metallic materials. As in chapter 2, the process of cell collapse is again captured through ligament reorientation at unit cell level. The chapter concludes with a set a parametric predictions for the dynamic compression of different metallic open-cell foams. The effects of dynamic loading are investigated independently for the rate of loading and viscosity which is investigated through the initial yield stress and the initial rate of plastic deformation.

In *chapter* 4 the dissertation presents the implementation of the micromechanical model for Open-cell foams developed in chapter 2 as a constitutive update into nonlinear implicit and explicit finite element analysis schemes. The chapter presents the key equations of the general continuum framework along with the spatial and temporal discretization of the general finite element analysis framework. Again, the key expressions from the micromechanical model formulated in chapter 2 will be restated to make the chapter self-contained. Here we well develop the formulation for the consistent tangents based on the micromechanical model from chapter 2. The chapter concludes with various simulations for visco-elastic and elasto-plastic open-cell foams capturing the different key stages in the deformation of foam materials such the heterogenous

bands of deformation during cellular structure collapse.

Finally, in *chapter* 5 the dissertation presents a brief summary along with a set of concluding remarks for the work presented here. The chapter will also make explicit the limitations of the developed model and it will also point out the work that could be undertaken in the near future to extend the applicability of the formulated theory. Here, the dissertation also presents areas of research work needed to help the scientific community complete our understanding of cellular solids with diverse properties in varying application environments such as brittle open-cell and closed-cell under thermal loading. Lastly, there is an *appendix* where the process for obtaining the effective foam response from the micromechanical model and the concept of Maxwell stress is presented.

Chapter 2

Micromechanical Modeling of Dynamically Loaded Open-Cell Foams

This chapter introduces a mesoscopic formulation for modeling the *dynamic* response of visco-elastic, open-cell solid foams. The effective material response is obtained by enforcing on a representative 3D unit cell the principle of minimum action for dissipative systems. The resulting model accounts explicitly for the foam topology, the elastic and viscous properties of the cell wall, and the inertial effects arising from non-affine motion within the cells. The micro-inertial effects become significant in retarding the foam collapse during extremely high strain-rate loading. The simulations show the ability of the model to capture the progressive foam collapse during dynamic compression as observed in experimental studies. The inertial and viscous strain rate effects are investigated through the foam density, viscosity, and relative density. Based on the physics incorporated into the micromechanical model, we provide insights on the physics mechanisms responsible for the experimentally observed strain rate effects on the behavior of dynamically loaded foam materials.

2.1 Introduction

Foam materials engage our interest because they are hybrid in structure and behavior, not exclusively solids, liquids, or gases. Foams have a solid or liquid cellular structure that entraps a gas within it, so they exhibit properties and characteristics of multiple states of matter (Perkowitz, 2000). Foams are usually produced by injecting a gas, such as air, into a material in the liquid state. The formation of foams can be seen in the commonplace nucleation and self-organization of the bubbles whenever someone pours a glass of beer or brews a cappuccino (Weaire and Hutzler, 1999). Solid cellular

materials are categorized as either open-cell or closed-cell foams depending on the shape of the cells. The cellular structure of open-cell foams looks like a network of small, interconnected ligaments allowing the surrounding fluid to flow during loading. The work presented in this chapter concentrates on homogeneous open-cell solid foams; however some of the ideas described here are also applicable to closed-cell solid foams.

Industrially there is a constant and sustained interest in utilizing cellular materials in dynamic loading scenarios. Foam materials are preferable in many engineering applications requiring mitigation of the adverse effects of sudden impact loading which can result in injuries to soft tissue and/or degradation of personnel and property shields. Many enterprises such as automotive, aircraft, and rail transportation, as well as the electronic, and packaging industries require strong yet lightweight materials which are capable of handling dynamic (up to impact-type) loads. Cellular solids such as viscoelastic open-cell foams can offer the benefits of light weight and sufficient strength along with the ability to absorb impact energy through dissipation mechanisms appearing in the large deformation regime during cellular structure collapse. Consequently, the focus of this treatment is on modeling the dynamic aspects of foams deformed at high strain rates.

As mentioned in chapter 1, Pioneering work in the area of foam mechanics has been introduced by a number of research groups, including Gibson and Ashby (1982, 1997); Dement'ev and Tarakanov (1970, 1973); Chen et al. (1994); Chen and Lakes (1996); Tyler and Ashby (1986); Deshpande et al. (2001); Deshpande and Fleck (2000a,b, 2001); Evans et al. (2001); Kraynik et al. (1997); Warren and Kraynik (1997). More recently, experimental and modeling studies have concentrated on the different stages of deformation as well as on the effect of the cell wall properties on the macroscopic response of foams, for instance Papka and Kyriakides (1998); Gong et al. (2005); Gong and Kyriakides (2005); Zhou et al. (2004a,b); Zhou and Soboyejo (2004); Lee et al. (2003, 2006b,a). Also, due to the constant interest in utilizing foams for energy absorption applications, there has been a number of experimental studies focusing on the dynamic response of foam systems, including Chen et al. (2002); Tedesco et al.

(1993); Rinde and Hoge (1971); Nagy et al. (1974); and especially for metallic foam materials, Deshpande and Fleck (2000a); Mukai et al. (1999a,b); Shimojima et al. (2001); Dannemann and Lankford (2000); Kanahashi et al. (2001, 2000); Yi et al. (2001); Han et al. (1998); Hall et al. (2000).

Modeling and simulating the behavior of foams is quite challenging due to unknown microstructural properties, complex microstructural geometry, extremely large deformations, and cell wall contact after collapse. Nevertheless, a number of modeling/simulation studies have surfaced which have provided connections between cellular architecture, cell wall material properties and the foam response. Some of the available works are based on tetrakaidecahedral unit cell models. For example, a 3D open-cell foam model with periodic tetrakaidecahedral cells was presented for the purpose of studying the nonlinear response of elastic 3D-periodic microstructures (Laroussi et al., 2002). The high-strain compression of open-cell foams was analyzed using a lattice model with tetrakaidecahedral cells (Zhu et al., 1997b). The micromechanical dynamic modeling work presented here evolved from a previously reported quasi-static tetrakaidecahedral unit cell model (Wang and Cuitiño, 2000). A micromechanical model for 3D open-cell foams using tetrakaidecahedral cells was developed using energy methods and Castigliano's second theorem (Li et al., 2003). The same group has also reported an open-cell micromechanical model for the emerging ultralightweight carbon foams (Sihn and Roy, 2001, 2004).

Other modeling efforts have employed the Voronoi technique. For instance, a study was done using a cubic open-cell model along with the Voronoi technique to generate the microstructure (Shulmeister et al., 1998). An investigation of cell irregularity effects was performed via ABAQUS FEA and a Voronoi open-cell foam with different degrees of randomness of the cell size and shape (Zhu and Windle, 2002). A few models are based on continuum approaches. For example there is a visco-elastic continuum model employing ABAQUS Software (Hucko and Faria, 1997) and there is a Cosseret continuum modeling study on cellular solids (Onck et al., 2001). Some other modeling works include the FEM comprehensive study on the effects of various geometrical imperfections on the in-plane yielding behavior of 2D cellular foams under biaxial

loading (Chen et al., 1999). Another study used a modified cube as the representative unit cell to model the quasi-static crushing of closed-cell metallic foams (Meguid et al., 2002). A rate-dependent elasto-plastic foam constitutive model was developed to use with LS-DYNA3D software (Zhang et al., 1998). Finally, recently a version of the material point method (MPM), the Generalized Interpolation Material Point method (GIMP method), was used to analyze a small group of open cells with emphasis on the densification portion of the deformation (Bardenhagen et al., 2005).

There are very few modeling studies which take into account the effects of dynamic loading (Zhang et al., 1998; Laroussi et al., 2002; Hucko and Faria, 1997). This paper presents a formulation for how the cells composing the cellular structure deform and move when a foam material is dynamically loaded at high strain rates. The model accounts for the effects of dynamic loading at high strain rates and can predict the overall foam response while being completely based on the open-cell topology, the cell wall properties, and the dominant deformation mechanisms at unit cell level. To our knowledge there is no micromechanical formulation in the literature for dynamically loaded, open-cell, periodic cellular materials similar to the one presented here. This model can provide physical insight into the deformation process happening at cell level while quantifying the effects of the foam cellular structure, ligament properties, and strain-rate on the overall mechanical response.

The model presented here evolved from a previously reported, quasi-static, hyper-elastic model (Wang and Cuitiño, 2000). Our version enhances the previous one through the added ability to model the response of dynamically loaded, viscoelastic, open-cell foams. While the local general formulation presented here can be applied to different unit cells, we limit the description to cells with an arbitrary number (M) of ligaments concurrent to one vertex. M is later set equal to four as a sample unit cell resulting in the cellular microstructure shown in Figure 2.1. The formulation starts with the expression for the Lagrangian of a representative unit cell comprising a given (imposed) macroscopic deformation history. Then, by enforcing the principle of minimum action, we determine a relation between the applied deformation and the motion of the unit cell vertex, which uniquely defines the kinematic state and thus the stress

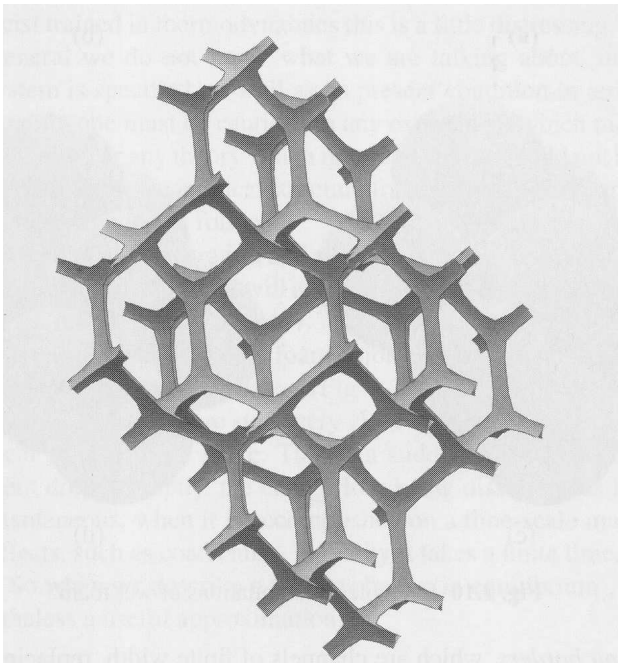

Figure 2.1: Representation of the open cell microstructure in foam systems, (Weaire and Hutzler, 1999).

state. The details of the formulation are presented in section 2.3.

Section 2.4 presents the predictions of the local microstructural model described in Section 2.3. We have selected a compressive, uniaxial loading case because it is perhaps one of the most interesting, challenging, and technologically relevant cases to study due to the effects introduced during the evolution of the cell collapse. It is also quite relevant from the application viewpoint due to the associated energy absorption/dissipation characteristics exhibited during the collapse. Based solely on the local microstructural model, a parametric study of a broad range of strain rates, ligament properties, and cellular structures are presented for the case of uniaxial compression. We gage the effects of strain rate, ligament material properties, and cellular geometry on the overall response of a dynamically loaded visco-elastic foam material. Finally, the local predicted response is contrasted with published experimental studies, the results will show similar trends to those exhibited in the experiments. A central aspect of the comparison with the experimental data is the characterization of the stress plateau. This plateau is due to the progressive cell collapse across the sample (Wang and Cuitiño,

2000; Gioia et al., 2001) and thus involves more than one cell. It is therefore necessary, before comparing the model's local predicted response with experiments, to 'average' the unit cell results in order to account for the entire sample. The effective response is based on the convexification of the microscopic non-convex energy landscape predicted by the unit cell model during the cell collapse process. In this context, the plateau stress is identified as the Maxwell stress (Ericksen, 1998). The procedure used to obtain the effective or 'average' response from the local response is briefly described in appendix A.

2.2 General Framework

We seek to obtain continuum-level constitutive relations for open-cell foam materials attendant to their internal microstructure. In particular, we concentrate on including in these relations the inertial effects arising from the internal collapse of the foam structure during dynamic loading. These constitutive relation can then be used in the framework of continuum mechanics to study the mechanical response of foam materials under general dynamic conditions by satisfying the governing field equations as will be done in Chapter 4. Formulating a proper constitutive relation $\mathbf{P}(\mathbf{F})$ for open-cell foams suffices for closing the problem defined by the field equations of continuum mechanics assuming that the foam material can be analyzed as a continuum system. In formulating the constitutive relation, we conceptualize that the material is generated by the systematic repetition of a particular unit cell, the size of which is much smaller than the region of interest (sample). In other words we assume separation of scales where the mechanical response of any material macroscopic point in the body is obtained from a local or microscopic model of the cellular structure as sketched in Figure 2.2.

2.3 Formulation of the Model

In this section we derive a continuum level constitutive relation $\mathbf{P}(\mathbf{F})$ for open cell foams subjected to dynamic loading based on a unit cell approach. While the procedure can be utilized for a more general class of unit cells, we limit our description

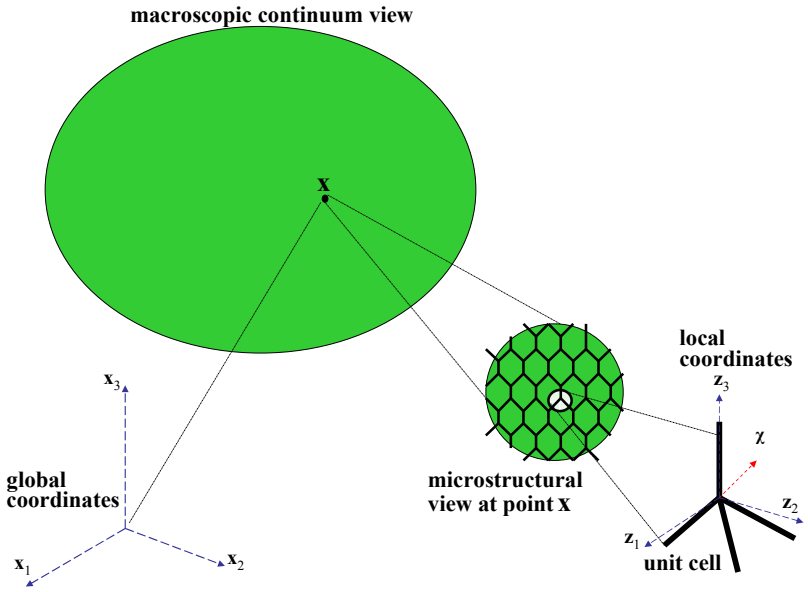

Figure 2.2: Schematic of the global, continuum view and the local, cellular structural view for foam material specimens much larger than the size of the cells. The macroscopic fields such as $\mathbf{u}$ and $\mathbf{F}$ prescribed at point $\mathbf{X}$ are trickled down to the microstructure to the midpoints of the ligaments. The vertex of each unit cell is allowed to move an additional amount $\boldsymbol{\chi}$ resulting in non-affine deformation within the microstructure.

to cells containing M ligaments concurring into one internal vertex. A coherent cellular solid can be generated from this type of unit cell by recursive application of point symmetry operations centered on each of the ligament midpoints (Wang and Cuitiño, 2000). For example, distorted or regular diamond-like structures such as the one shown in Figure 2.1 result from this procedure by setting $M = 4$. The four ligament unit cell is enclosed inside a dual tetrakaidecahedron volume element ($\mathcal{B}_o$) which represents the portion of volume occupied by the unit cell.

In Section 2.3.1, we describe the assumed kinematics for the unit cell and continue in Section 2.3.2 with the expressions for the elastic and viscous potentials which define the local constitutive behavior of the unit cell ligaments. Then in Section 2.3.3, we introduce a key step in the derivation of the constitutive relation that allows us to link the macroscopic deformation to the local non-affine deformation by enforcing the principle of stationary action at cell level. One of the key aspects in setting up the Lagrangian is the selection of the appropriate boundary conditions. As we shall see in

that section, both surface and volumetric terms need to be considered for the present dynamic case. Finally in Section 2.3.4, we define the stress state for the kinematic state of the unit cell based on the assumed elastic and viscous potentials.

2.3.1 Kinematics

Consider that the *macroscopic* description of the kinematics of a cellular material point $\mathbf{X}$ is governed by the time-evolution of the displacement field $\mathbf{u}(\mathbf{X}, t)$ such that $\mathbf{x} = \mathbf{X} + \mathbf{u}$. It it is implicitly assumed that there is a length scale separation where the microstructural dimensions are much smaller than the macroscopic dimensions. In this context, a macroscopic point $\mathbf{X}$ translates into a microscopic array of homogeneous unit cells sharing the same macroscopic fields. The macroscopic fields such as displacement $\mathbf{u}$, velocity $\mathbf{v}$, and acceleration $\mathbf{a}$ are trickled down to a microstructural model, however in the present formulation we allow for non-affine motion within each cell. More specifically, we assume that the macroscopic fields ($\mathbf{u}$, $\mathbf{v}$, $\mathbf{a}$) *only* describe the motion of the ligament midpoints, and the intra-cell deformation (ligament bending and stretching) is uniquely determined by the motion of the unit cell central vertex. While more relaxed kinematics can also be considered by introducing, for example, central vertex rotations, we select the present one as the simplest description that can capture the process of cell collapse for low relative density foams.

To start lets define the initial unit cell configuration. The solid part of each unit cell is composed by half of the length of M ligaments converging at the cell vertex. The initial undeformed state of this unit cell is described by M vectors denoted by $\mathbf{L}$ representing the M ligaments. All the vectors have a common origin, the central vertex, and each one ends at the ligament midpoint. These vectors are defined as

$$\mathbf{L}^i = L^i \mathbf{e}^{L^i} \quad \text{with } i = 1 \text{ to } M \tag{2.1}$$

where L^i represents half of the ligament's initial length and $\mathbf{e}^{L^i}$ is a unit vector centered at the vertex that defines the initial orientation. The initial angle (Ψ^{ij}) between any two ligaments $\mathbf{L}^i$ and $\mathbf{L}^j$ can be easily obtained by recourse of the inner product:

$$\Psi^{ij} = \cos^{-1}\left(\frac{\mathbf{L}^i \cdot \mathbf{L}^j}{L^i \, L^j}\right) \tag{2.2}$$

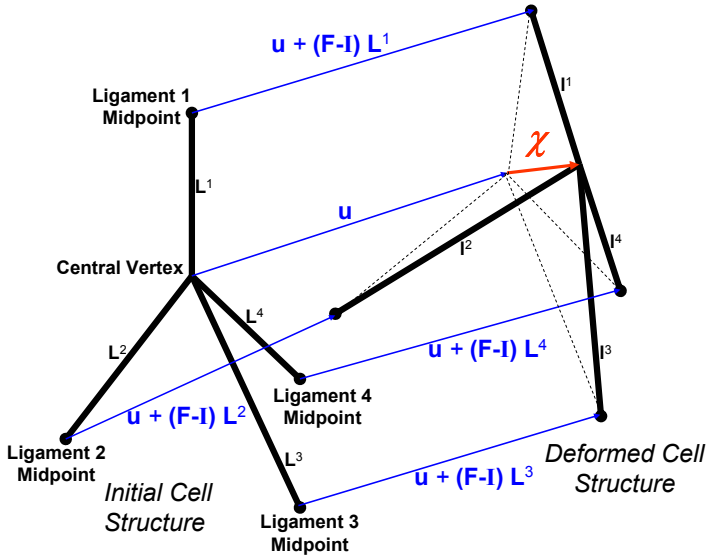

Figure 2.3: Depiction of the kinematic assumptions for a 4-ligament unit cell showing the reference and deformed cell configurations. Keep in mind that each unit cell is composed with only half of the length of each ligament since each ligament is shared by two adjacent cells in the cellular microstructure. All ligament midpoints move with the specified macroscopic affine field $\mathbf{u}(\mathbf{X}, t)$, while the central vertex may have the additional displacement of $\boldsymbol{\chi}(\mathbf{X}, t)$. Note that if $\boldsymbol{\chi} = 0$ the cell motion is affine which corresponds to the position indicated by the dashed lines.

Now, let $\boldsymbol{\chi}(\mathbf{X}, t)$ be the non-affine component of the motion of the central vertex, i.e. that the total displacement field of the central vertex is given by $\mathbf{u}(\mathbf{X}, t) + \boldsymbol{\chi}(\mathbf{X}, t)$, which is schematically shown in Figure 2.3. As indicated in Figure 2.3, all midpoints are tied-up to the macroscopic motion while the central vertex may have the additional motion $\boldsymbol{\chi}$ inducing heterogeneous deformation within the cell. Only axial and bending (including bending shear) deformation are considered in the present description because these are the dominant modes of deformation during cell collapse for uniaxial loading. Other effects such as torsion are not introduced in the formulation. Moreover, as the relative-density is reduced (i.e. thinner ligaments) the bending deformation concentrates near the central vertex, as depicted in Figure 2.4, where the bending moment is a maximum. We exploit this observation to postulate that bending deformation is localized at the central vertex, which further implies that all ligaments remain straight. In order to describe the intra-cell fields, we define a local coordinate system for each

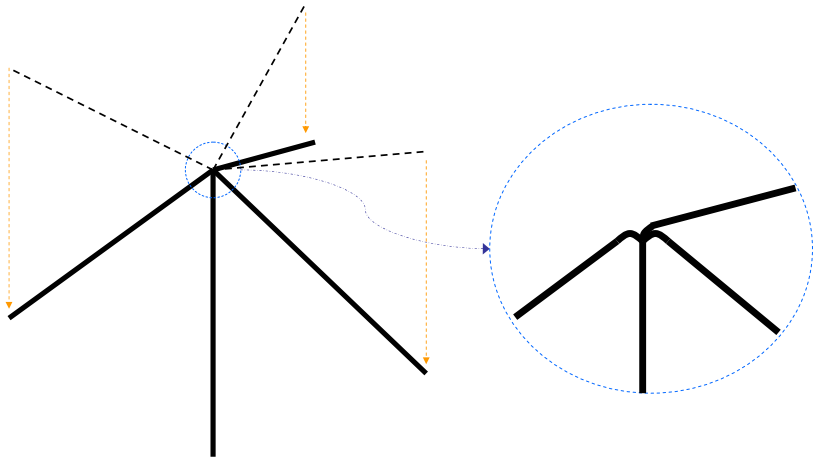

Figure 2.4: Schematic of the localization of bending at the unit cell vertex allowing the ligaments to remain straight during deformation.

ligament i,

$$\zeta^i = \frac{Z^i}{L^i} \tag{2.3}$$

where Z^i is the location of the material point along the ligament i measured from the central vertex and as mentioned earlier L^i is the half length of the corresponding ligament. In this manner, $\zeta^i = 0$ is always at the central vertex and $\zeta^i = 1$ is a point located at the outer boundary of the unit cell or at the midpoint of ligament i. The intra-cell displacement field for each ligament i can then be written as:

$$\mathbf{u}^i(\mathbf{X}, t, \zeta^i) = \mathbf{u}^i_{\text{affine}}(\mathbf{X}, t, \zeta^i) + \mathbf{u}^i_{\text{non-affine}}(\mathbf{X}, t, \zeta^i) \tag{2.4}$$

where the affine and non-affine components can be expressed by

$$\mathbf{u}^i_{\text{affine}}(\mathbf{X}, t, \zeta^i) = \mathbf{u}(\mathbf{X}, t) + (\mathbf{F}(\mathbf{X}, t) - \mathbf{I})\ \mathbf{L}^i\ \zeta^i \quad \text{(no sum over } i\text{)} \tag{2.5}$$

and

$$\mathbf{u}^i_{\text{non-affine}}(\mathbf{X}, t, \zeta^i) = \boldsymbol{\chi}\ (1 - \zeta^i)\ . \tag{2.6}$$

Similarly, the velocity field can be written for each ligament i as

$$\mathbf{v}^i(\mathbf{X}, t, \zeta^i) \quad = \quad \mathbf{v}^i_{\text{affine}}(\mathbf{X}, t, \zeta^i) + \mathbf{v}^i_{\text{non-affine}}(\mathbf{X}, t, \zeta^i) \quad \text{with} \tag{2.7}$$

$$\mathbf{v}^i_{\text{affine}}(\mathbf{X},t,\zeta^i) = \mathbf{v}(\mathbf{X},t) + \dot{\mathbf{F}}(\mathbf{X},t)\ \mathbf{L}^i\ \zeta^i \quad \text{(no sum in } i\text{) and} \tag{2.8}$$

$$\mathbf{v}^i_{\text{non-affine}}(\mathbf{X},t,\zeta^i) = \dot{\boldsymbol{\chi}}(1-\zeta^i) \tag{2.9}$$

and acceleration field as

$$\mathbf{a}^i(\mathbf{X},t,\zeta^i) = \mathbf{a}^i_{\text{affine}}(\mathbf{X},t,\zeta^i) + \mathbf{a}^i_{\text{non-affine}}(\mathbf{X},t,\zeta^i) \quad \text{with} \tag{2.10}$$

$$\mathbf{a}^i_{\text{affine}}(\mathbf{X},t,\zeta^i) = \mathbf{a}(\mathbf{X},t) + \ddot{\mathbf{F}}(\mathbf{X},t)\ \mathbf{L}^i\ \zeta^i \quad \text{(no sum in } i\text{) and} \tag{2.11}$$

$$\mathbf{a}^i_{\text{non-affine}}(\mathbf{X},t,\zeta^i) = \ddot{\boldsymbol{\chi}}(1-\zeta^i) \tag{2.12}$$

The assumed kinematics implies that the current configuration of each ligament $\mathbf{l}^i(\mathbf{X},t)$ can be expressed as:

$$\mathbf{l}^i(\mathbf{X},t) = l^i\mathbf{e}^{l^i} = \mathbf{F}(\mathbf{X},t)\ \mathbf{L}^i - \boldsymbol{\chi}(\mathbf{X},\mathbf{t}) \tag{2.13}$$

where l^i is the current half length of the ligament and $\mathbf{e}^{l^i}$ is the current orientation (unit vector). Notice that

$$\frac{\partial l^i}{\partial \mathbf{l}^i} = \frac{\partial}{\partial \mathbf{l}^i}\sqrt{\mathbf{l}^i\cdot\mathbf{l}^i} = \frac{\mathbf{l}^i}{\sqrt{\mathbf{l}^i\cdot\mathbf{l}^i}} = \mathbf{e}^{l^i} \tag{2.14}$$

The rate of change of each leg vector can be expressed as:

$$\frac{d}{dt}(\mathbf{l}^i(\mathbf{X},t)) = \dot{\mathbf{l}}^i(\mathbf{X},t) = \dot{\mathbf{F}}(\mathbf{X},t)\ \mathbf{L}^i - \dot{\boldsymbol{\chi}}(\mathbf{X},t). \tag{2.15}$$

or

$$\dot{\mathbf{l}}^i = \frac{d}{dt}l^i\mathbf{e}^{l^i} = \dot{l}^i\mathbf{e}^{l^i} + l^i\dot{\mathbf{e}}^{l^i} \tag{2.16}$$

Here $\dot{l}^i$ refers to the component of the leg velocity along the leg direction and it is not to be confused with the magnitude of the entire leg velocity $|\dot{\mathbf{l}}^i|$, namely

$$\dot{l}^i \neq |\dot{\mathbf{l}}^i| = \sqrt{\dot{\mathbf{l}}^i\cdot\dot{\mathbf{l}}^i} \tag{2.17}$$

Also notice that

$$\dot{l}^i = \frac{d\sqrt{\mathbf{l}^i\cdot\mathbf{l}^i}}{dt} = \mathbf{e}^{l^i}\cdot\dot{\mathbf{l}}^i \ \text{ and thus } \ \frac{\partial \dot{l}^i}{\partial \dot{\mathbf{l}}^i} = \mathbf{e}^{l^i} \tag{2.18}$$

The current angle ψ^{ij} and the angle rate of change $\dot{\psi}^{ij}$ between any two ligaments i and j can be computed using expressions 2.13 and 2.15 and the recourse of the inner

product,

$$\psi^{ij} = \cos^{-1}\left(\frac{\mathbf{l}^i \cdot \mathbf{l}^j}{l^i l^j}\right) \tag{2.19}$$

$$\dot{\psi}^{ij} = \frac{d\psi^{ij}}{dt} = \frac{\partial \psi^{ij}}{\partial \mathbf{l}^i} \cdot \dot{\mathbf{l}}^i + \frac{\partial \psi^{ij}}{\partial \mathbf{l}^j} \cdot \dot{\mathbf{l}}^j. \tag{2.20}$$

Notice that

$$\frac{\partial \psi^{ij}}{\partial \mathbf{l}^i} = \frac{\partial}{\partial \mathbf{l}^i} cos^{-1}\left(\frac{\mathbf{l}^i \cdot \mathbf{l}^j}{l^i l^j}\right) = \frac{\partial}{\partial \mathbf{l}^i} cos^{-1}\left(\frac{\mathbf{l}^i \cdot \mathbf{l}^j}{\sqrt{\mathbf{l}^i \cdot \mathbf{l}^i} l^j}\right) \tag{2.21}$$

$$= \frac{-1}{\sqrt{1 - \left(\frac{\mathbf{l}^i \cdot \mathbf{l}^j}{l^i l^j}\right)^2}} \left[\frac{\mathbf{l}^j}{l^i l^j} - \frac{(\mathbf{l}^i \cdot \mathbf{l}^j)\mathbf{l}^i}{(l^i)^3 l^j}\right] \tag{2.22}$$

$$= \frac{-l^i l^j}{\sqrt{(l^i l^j)^2 - (\mathbf{l}^i \cdot \mathbf{l}^j)^2}} \left[\frac{\mathbf{l}^j}{l^i l^j} - \frac{(\mathbf{l}^i \cdot \mathbf{l}^j)\mathbf{l}^i}{(l^i)^3 l^j}\right] \tag{2.23}$$

$$= \frac{-1}{\sqrt{(l^i l^j)^2 - (\mathbf{l}^i \cdot \mathbf{l}^j)^2}} \left[\mathbf{l}^j - \frac{(\mathbf{l}^i \cdot \mathbf{l}^j)\mathbf{l}^i}{\mathbf{l}^i \cdot \mathbf{l}^i}\right] \tag{2.24}$$

Let

$$\mathbf{a}^{l^i l^j} = \mathbf{l}^j - \frac{(\mathbf{l}^i \cdot \mathbf{l}^j)\mathbf{l}^i}{\mathbf{l}^i \cdot \mathbf{l}^i} \tag{2.25}$$

and notice that the magnitude of $\mathbf{a}^{l^i l^j}$ is

$$|\mathbf{a}^{l^i l^j}| = \sqrt{\mathbf{a}^{l^i l^j} \cdot \mathbf{a}^{l^i l^j}} \tag{2.26}$$

$$= \sqrt{\mathbf{l}^j \cdot \mathbf{l}^j - 2\frac{(\mathbf{l}^i \cdot \mathbf{l}^j)}{\mathbf{l}^i \cdot \mathbf{l}^i}(\mathbf{l}^i \cdot \mathbf{l}^j) + \frac{(\mathbf{l}^i \cdot \mathbf{l}^j)}{(\mathbf{l}^i \cdot \mathbf{l}^i)}\frac{(\mathbf{l}^i \cdot \mathbf{l}^j)}{(\mathbf{l}^i \cdot \mathbf{l}^i)}(\mathbf{l}^i \cdot \mathbf{l}^i)} \tag{2.27}$$

$$= \sqrt{(\ l^j)^2 - 2\frac{(\mathbf{l}^i \cdot \mathbf{l}^j)^2}{(l^i)^2} + \frac{(\mathbf{l}^i \cdot \mathbf{l}^j)^2}{(l^i)^2}} \tag{2.28}$$

$$= \sqrt{(l^j)^2 - \frac{(\mathbf{l}^i \cdot \mathbf{l}^j)^2}{(l^i)^2}} \tag{2.29}$$

$$= \frac{1}{l^i}\sqrt{(l^i l^j)^2 - (\mathbf{l}^i \cdot \mathbf{l}^j)^2} \tag{2.30}$$

This means that $\frac{\partial \psi^{ij}}{\partial \mathbf{l}^i}$ can be written as

$$\frac{\partial \psi^{ij}}{\partial \mathbf{l}^i} = \frac{1}{l^i}\mathbf{e}^{l^i l^j} \tag{2.31}$$

where $\mathbf{e}^{l^i l^j}$ is a direction defined as

$$\mathbf{e}^{l^i l^j} = -\frac{\mathbf{a}^{l^i l^j}}{|\mathbf{a}^{l^i l^j}|} \tag{2.32}$$

Based on Equation 2.20, we can also say that

$$\frac{\partial \dot{\psi}^{ij}}{\partial \dot{\mathbf{l}}^{i}} = \frac{\partial \psi^{ij}}{\partial \mathbf{l}^{i}} = \frac{1}{l^{i}} \mathbf{e}^{l^{i} l^{j}} \tag{2.33}$$

Equations 2.13, 2.15, 2.19 and 2.20 are the primary kinematic variables used in the present formulation. These variables are defined in terms of the *specified* field $\mathbf{u}(\mathbf{X}, t)$ (and its associated fields $\mathbf{F}(\mathbf{X}, t)$, $\mathbf{v}(\mathbf{X}, t)$ etc..) and in terms of the *unknown and yet to be determined* field $\boldsymbol{\chi}(\mathbf{X}, t)$. In Section 2.3.3 we introduce a condition that implicitly ties up $\boldsymbol{\chi}$ to $\mathbf{u}$, making 2.13, 2.15, 2.19 and 2.20 unique functions of the specified field $\mathbf{u}$. Before finding such a condition it is convenient to define the local, ligament constitutive relations.

2.3.2 Local Constitutive Relations

We assume that there exist an elastic potential $\mathcal{W}$ and a dissipative potential $\mathcal{D}$ which are functions of the primary kinematic variables defined in Equations 2.13, 2.15, 2.19 and 2.20. We based our assumptions of the existence of these potentials on Ortiz and Stainer (1999) and Lubliner (1972, 1990) which provide guidelines for the selection of constitutive updates in modeling the behavior of visco-elastic and visco-plastic solids. While the structure of these potentials could be quite general, we adopt an additive form for the stretching and the bending contributions. The elastic potential is written as

$$\mathcal{W}(l^{i}, \psi^{ij}) = \frac{1}{\mathcal{B}_o} \left[\sum_{i=1,M} W_{\mathcal{N}}(l^{i}) + \frac{1}{2} \sum_{i=1,M} \sum_{j=1,M} W_{\mathcal{M}}(\psi^{ij}) \right] \tag{2.34}$$

where $\mathcal{B}_o$ is the volume of the unit cell in the reference configuration and $W_{\mathcal{N}}(l^{i})$ and $W_{\mathcal{M}}(\psi^{ij})$ are defined as the elastic energy due to stretching and bending respectively. The derivatives with respect to their independent variables give the *elastic* axial force $\mathcal{N}_i^E$ in ligament i and the *elastic* bending moment $\mathcal{M}_{ij}^E$ between ligaments i and j, i.e.

$$\frac{\partial W_{\mathcal{N}}(l^{i})}{\partial l^{i}} = \mathcal{N}_i^E(l^{i}) \quad \text{and} \quad \frac{\partial W_{\mathcal{M}}(\psi^{ij})}{\partial \psi^{ij}} = \mathcal{M}_{ij}^E(\psi^{ij}) \tag{2.35}$$

Similarly, the dissipative potential is written as

$$\mathcal{D}(\dot{l}^{i}, \dot{\psi}^{ij}) = \frac{1}{\mathcal{B}_o} \left[\sum_{i=1,M} D_{\mathcal{N}}(\dot{l}^{i}) + \frac{1}{2} \sum_{i=1,M} \sum_{j=1,M} D_{\mathcal{M}}(\dot{\psi}^{ij}) \right] \tag{2.36}$$

where $D_{\mathcal{N}}(\dot{l}^i)$ and $D_{\mathcal{M}}(\dot{\psi}^{ij})$ are the dissipative energy terms due to stretching and bending respectively. Again, the derivatives with respect to their independent variables provide the *viscous* axial force $\mathcal{N}_i^\eta$ in ligament i and the *viscous* bending moment $\mathcal{M}_{ij}^\eta$ between ligaments i and j, i.e.

$$-\frac{\partial D_{\mathcal{N}}(\dot{l}^i)}{\partial \dot{l}^i} = \mathcal{N}_i^\eta(\dot{l}^i) \quad \text{and} \quad -\frac{\partial D_{\mathcal{M}}(\dot{\psi}^{ij})}{\partial \dot{\psi}^{ij}} = \mathcal{M}_{ij}^\eta(\dot{\psi}^{ij}). \tag{2.37}$$

It should be noted that the functions in Equations 2.35 and 2.37 should be provided as part of the material description. These functions describe the constitutive behavior of the ligament material and thus will depend on the specific material to be modeled. In Section 2.4 some concrete examples are provided for all four functions, which are needed to obtain definite predictions.

2.3.3 Linking Local to Global

Before a constitutive expression can be formulated, it is necessary to link the specified global field $\mathbf{u}(\mathbf{X}, t)$ with the local unknown one $\boldsymbol{\chi}(\mathbf{X}, t)$. By providing such a condition, the intra-cell kinematics can be determined univocally for a given macroscopic field, and thus, the stress state can be obtained as will be shown in Section 2.3.4. The sought relationship can be realized by enforcing the principle of stationary action on the Lagrangian. Since dissipation is included in the present formulation, we also need to account for the non-conservative terms. The application of this principle in the static case reduces to enforcing local or cell level equilibrium (Wang and Cuitiño, 2000). The dynamic case, however, requires a more careful consideration.

Our region of analysis is the representative unit cell for which we need to specify the appropriate constraints: boundary and loading conditions. To enforce compatibility among cells, we specify that at the intersection of unit cell boundary with each ligament, i.e. when $\zeta^i = 1$ in Equation 2.3, the motion is prescribed by the macro fields or the affine components of the displacement, velocity and acceleration fields. These conditions are trivially satisfied by the assumed cell kinematics, which gives only the affine components for $\zeta^i = 1$ in Equations 2.4, 2.7 and 2.10. The treatment of the inertial forces is similar to the one appearing in formulating the static problem under

gravitational loads. Here the inertial force field $\mathbf{p}$ prescribed by the macro fields is:

$$\mathbf{p}^i(\mathbf{X}, t, \zeta_i) = \tilde{\rho}_s^i(\zeta^i) \;\; \mathbf{a}_{\text{affine}}(\mathbf{X}, t, \zeta^i) \tag{2.38}$$

where $\tilde{\rho}_s^i$ is the mass density per unit length of the solid ligament i and $\mathbf{a}^i_{\text{affine}}$ is the affine component of the acceleration defined in Equation 2.11. Note that these inertial forces will "work" against the cell displacements, contributing to the potential of the forces.

Now we turn our attention to formulating the principle of stationary action for the representative unit cell, which provides the condition to link the macro-fields with the intra-cell fields. At unit cell level, the only degree of freedom in our system is the motion of the central vertex $\boldsymbol{\chi} = \chi_\alpha \mathbf{e}_\alpha$ where χ_α are the Cartesian components along an orthogonal 3D basis, $\mathbf{e}_\alpha$. For a non-conservative system such as the one here, the principle of stationary action states that

$$\frac{d}{dt}\left(\frac{\partial \mathcal{L}}{\partial \dot{\chi}_\alpha}\right) - \frac{\partial \mathcal{L}}{\partial \chi_\alpha} = Q_\alpha \tag{2.39}$$

where Q_α are the nonconservative terms arising from the ligament's viscous response which are given by

$$Q_\alpha = \frac{\partial \mathcal{D}}{\partial \dot{\chi}_\alpha} \tag{2.40}$$

$\mathcal{L}$ is the Lagrangian which is defined as

$$\mathcal{L}(\chi_\alpha, \dot{\chi}_\alpha) = \mathcal{T}(\dot{\chi}_\alpha) - \mathcal{V}(\chi_\alpha) = \mathcal{T}(\dot{\chi}_\alpha) - [\mathcal{W}(\chi_\alpha) + \mathcal{P}(\chi_\alpha)] \tag{2.41}$$

where $\mathcal{T}$ is the kinetic energy and $\mathcal{V}$ is the potential energy which includes both the elastic potential energy ($\mathcal{W}$) and the inertial potential energy ($\mathcal{P}$) due to the affine inertial forces. Noting that the kinetic energy doesn't depend on χ_α and the potential energy terms don't depend on $\dot{\chi}_\alpha$, the principle of stationary actions can now be recast as

$$\frac{d}{dt}\left(\frac{\partial \mathcal{T}}{\partial \dot{\chi}_\alpha}\right) + \frac{\partial \mathcal{W}}{\partial \chi_\alpha} + \frac{\partial \mathcal{P}}{\partial \chi_\alpha} = \frac{\partial \mathcal{D}}{\partial \dot{\chi}_\alpha} \quad . \tag{2.42}$$

Mass and Relative Density

The unit cell mass and density terms needed for the present formulation are presented here. The total mass contained in the unit cell can be easily computed by adding the

individual mass of each ligament. We define a mass density per unit reference length $\tilde{\rho}_s^i$ for each ligament i as

$$\tilde{\rho}_s^i(\zeta^i) = \rho_s^i(\zeta^i) A^i(\zeta^i) \tag{2.43}$$

where $\rho_s^i(\zeta^i)$ and $A(\zeta^i)$ are respectively the volumetric mass density and the cross sectional area of the solid ligament i at the location ζ^i. Remembering that the total reference length of each ligament is L^i, the mass of each ligament (m^i) is computed as

$$m^i = L^i \int_0^1 \tilde{\rho}_s^i(\zeta^i)\ \mathrm{d}\zeta^i \tag{2.44}$$

and the total unit cell mass (m) and foam density (ρ) are respectively given by

$$m = \sum_{i=1,M} m^i \quad \text{and} \quad \rho = m/\mathcal{B}_o \tag{2.45}$$

Recall that $\mathcal{B}_o$ is the volume of the unit cell in the initial or reference configuration.

The *relative* density (ρ_r) which is defined as the ratio of the foam density (ρ) to the solid ligament material density (ρ_s) can be defined solely in terms of microstructural geometrical parameters. As previously shown in the quasi-static, elastic version of this model (Wang and Cuitiño, 2000), the relative density can be defined solely in terms of the ligament radius (r) and ligament length (L) for foams composed of unit cells containing 4 cylindrical ligaments ($M = 4$).

$$\rho_\mathrm{r} = \frac{\rho}{\rho_\mathrm{s}} = \frac{3\sqrt{3}\pi}{16}\frac{r^2}{L^2} - \left(\frac{3\sqrt{6}\pi}{32} - \frac{23\sqrt{2}}{96}\right)\frac{r^3}{L^3} \tag{2.46}$$

Now we concentrate on writing down the expressions and derivatives indicated in the principle of stationary action Equation 2.42.

Kinetic Energy Terms

The kinetic-energy-density expression for the M-strut unit cell model can be obtained using the definitions for velocity and mass defined in Equations 2.7 and 2.44 respectively.

$$\mathcal{T} = \frac{1}{2\mathcal{B}_o}\left(\sum_{i=1,M} L^i \int_0^1 \tilde{\rho}_s^i\ (\mathbf{v}^i \cdot \mathbf{v}^i)\ \mathrm{d}\zeta^i\right) \tag{2.47}$$

The principal of stationary action requires the time derivative of the partial derivative of the kinetic energy with respect to the components of $\dot{\boldsymbol{\chi}}$. In order to obtain this

derivative, first we evaluate the partial derivative of the kinetic energy with respect to the components of $\dot{\boldsymbol{\chi}}$ resulting in

$$\frac{\partial \mathcal{T}}{\partial \dot{\chi}_\alpha} = \frac{1}{\mathcal{B}_o}\left(\sum_{i=1,M} L^i \int_0^1 \tilde{\rho}_s^i \; v^i_{\text{affine},\alpha} \; (1-\zeta^i) \; \mathrm{d}\zeta^i + m_c \; \dot{\chi}_\alpha\right) \tag{2.48}$$

where $v^i_{\text{affine},\alpha}$ are the Cartesian components of the affine portion of the velocity of ligament i which is given in Equation 2.8 and

$$m_c = \sum_{i=1,M} L^i \int_0^1 \tilde{\rho}_s^i \; (1-\zeta^i)^2 \; \mathrm{d}\zeta^i, \tag{2.49}$$

which can be interpreted as the effective mass at the central vertex. Finally, we evaluate the time derivative of Equation 2.48 to obtain

$$\frac{d}{dt}\left(\frac{\partial \mathcal{T}}{\partial \dot{\chi}_\alpha}\right) = \frac{1}{\mathcal{B}_o}\left(\sum_{i=1,M} L^i \int_0^1 \tilde{\rho}_s^i \; a^i_{\text{affine},\alpha} \; (1-\zeta^i) \; \mathrm{d}\zeta^i + m_c \; \ddot{\chi}_\alpha\right) \tag{2.50}$$

where $a^i_{\text{affine},\alpha}$ are the Cartesian components of the affine portion of the acceleration of ligament i which is given in Equation 2.11.

Potential of the Inertial Forces

The potential of the inertial forces $\mathcal{P}$ is defined as the negative of the work done by the inertial forces

$$\mathcal{P} = -\frac{1}{\mathcal{B}_o} \sum_{i=1,M} L^i \int_0^1 (\mathbf{p}^i \cdot \mathbf{u}^i) \; \mathrm{d}\zeta^i \tag{2.51}$$

where $\mathbf{p}$ is the inertial force field given in Equation 2.38 and $\mathbf{u}$ is the displacement field given in Equation 2.4. Now, the partial derivative of this inertial potential energy with respect to the components of $\boldsymbol{\chi}$ becomes

$$\frac{\partial \mathcal{P}}{\partial \chi_\alpha} = -\frac{1}{\mathcal{B}_o} \sum_{i=1,M} L^i \int_0^1 \tilde{\rho}_s^i a^i_{\text{affine},\alpha} \; (1-\zeta^i) \; \mathrm{d}\zeta^i. \tag{2.52}$$

Elastic Potential Terms

The principle of stationary action will also require the derivative of the elastic potential $\mathcal{W}$ defined in Equation 2.34 with respect to the components of $\boldsymbol{\chi}$, namely

$$\frac{\partial \mathcal{W}}{\partial \chi_\alpha} = \frac{1}{\mathcal{B}_o}\left[\sum_{i=1,M} \frac{\partial W_{\mathcal{N}}(l^i)}{\partial \chi_\alpha} + \frac{1}{2}\sum_{i=1,M}\sum_{j=1,M} \frac{W_{\mathcal{M}}(\psi^{ij})}{\partial \chi_\alpha}\right] \tag{2.53}$$

This derivative can be evaluated by employing the chain rule along with the kinematic relations in Equations 2.13 and 2.19.

$$\frac{\partial \mathcal{W}}{\partial \boldsymbol{\chi}} = \frac{1}{\mathcal{B}_o}\left[\sum_{i=1,M}\left(\frac{\partial W_{\mathcal{N}}}{\partial l^i}\frac{\partial l^i}{\partial \mathbf{l}^i}\frac{\partial \mathbf{l}^i}{\partial \boldsymbol{\chi}} + \frac{1}{2}\sum_{j=1,M}\frac{\partial W_{\mathcal{M}}}{\partial \psi^{ij}}\left(\frac{\partial \psi^{ij}}{\partial \mathbf{l}^i}\frac{\partial \mathbf{l}^i}{\partial \boldsymbol{\chi}} + \frac{\partial \psi^{ij}}{\partial \mathbf{l}^j}\frac{\partial \mathbf{l}^j}{\partial \boldsymbol{\chi}}\right)\right)\right] \tag{2.54}$$

Recalling that $\frac{\partial W_{\mathcal{N}^i}}{\partial l^i} = \mathcal{N}_i^E$ and $\frac{\partial W_{\mathcal{M}^i}}{\partial \psi^{ij}} = \mathcal{M}_{ij}^E$ from Equation 2.35 and also recalling that

$$\frac{\partial l^i}{\partial \mathbf{l}^i} = \mathbf{e}^{l^i} \quad \text{and} \quad \frac{\partial \psi^{ij}}{\partial \mathbf{l}^i} = \frac{\mathbf{e}^{l^i l^j}}{l^i} \tag{2.55}$$

from Equations 2.14 and 2.31, where $\mathbf{e}^{l^i l^j}$ is a unit vector contained in the plane defined by $\mathbf{l}^i$ and $\mathbf{l}^j$ and normal to $\mathbf{l}^i$. Then, the derivative can now be expressed in a more compact form as

$$\frac{\partial \mathcal{W}}{\partial \boldsymbol{\chi}} = \frac{1}{\mathcal{B}_o}\left[\sum_{i=1,M}\left(\mathcal{N}_i^E\mathbf{e}^{l^i} + \frac{1}{l^i}\sum_{j=1,M}\mathcal{M}_{ij}^E\mathbf{e}^{l^i l^j}\right)\frac{\partial \mathbf{l}^i}{\partial \boldsymbol{\chi}}\right] \tag{2.56}$$

or in component form as

$$\frac{\partial \mathcal{W}}{\partial \chi_\alpha} = \frac{1}{\mathcal{B}_o}\left[\sum_{i=1,M}\left(\mathcal{N}_i^E e_m^{l^i} + \frac{1}{l^i}\sum_{j=1,M}\mathcal{M}_{ij}^E e_m^{l^i l^j}\right)\frac{\partial l_m^i}{\partial \chi_\alpha}\right] \tag{2.57}$$

where sum in m is implied. Additionally from Equation 2.13, we have that $l_m^i = F_{kK}L_K^i - \chi_m$ and consequently

$$\frac{\partial l_m^i}{\partial \chi_\alpha} = -\delta_{\alpha m} \tag{2.58}$$

Then, the derivative of the elastic potential with respect to the components of $\boldsymbol{\chi}$ becomes

$$\begin{aligned}
\frac{\partial \mathcal{W}}{\partial \chi_\alpha} &= -\frac{1}{\mathcal{B}_o}\left[\sum_{i=1,M}\left(\mathcal{N}_i^E e_\alpha^{l^i} + \frac{1}{l^i}\sum_{j=1,M}\mathcal{M}_{ij}^E e_\alpha^{l^i l^j}\right)\right] \\
&= -\frac{1}{\mathcal{B}_o}\left[\sum_{i=1,M}\left(\mathcal{N}_i^E e_\alpha^{l^i} + \mathcal{V}_i^E e_\alpha^{\bar{l}^i}\right)\right] \\
&= -\frac{1}{\mathcal{B}_o}\left[\sum_{i=1,M} f_\alpha^{E,i}\right]
\end{aligned} \tag{2.59}$$

In the expressions above, recall that $\mathcal{W}$ refers to the elastic potential defined in Equation 2.34 and $\mathcal{N}_i^E$ and $\mathcal{M}_i^E$ are the elastic forces and moments respectively which were

defined in Equation 2.35. In the last expression above, the term denoted by $f_\alpha^{E,i}$ represents the sum of the Cartesian components of the *elastic* axial $\mathcal{N}_i^E$ and shear $\mathcal{V}_i^E$ forces from ligament i applied at the vertex of the unit cell.

Dissipative Potential Terms

In the same manner that $\frac{\partial \mathcal{W}}{\partial \chi_\alpha}$ was evaluated earlier, we evaluate the derivative of the dissipated viscous energy $\mathcal{D}$ with respect to the vertex velocity $\dot{\boldsymbol{\chi}}$, namely $\frac{\partial \mathcal{D}}{\partial \dot{\chi}_\alpha}$ which provides us with the nonconservative forces Q_α, needed in the principle of minimum action,

$$\frac{\partial \mathcal{D}}{\partial \dot{\chi}_\alpha} = \frac{1}{\mathcal{B}_o}\left[\sum_{i=1,M} \frac{\partial D_{\mathcal{N}}(\dot{l}^i)}{\partial \dot{\chi}_\alpha} + \frac{1}{2}\sum_{i=1,M}\sum_{j=1,M} \frac{\partial D_{\mathcal{M}}(\dot{\psi}^{ij})}{\partial \dot{\chi}_\alpha}\right] \tag{2.60}$$

Taking the rate of change in length for each strut $\dot{l}^i$ and the rate of change in angle between struts $\dot{\psi}^{ij}$ as given by Equations 2.13-2.20 allows us to rewrite $\frac{\partial \mathcal{D}}{\partial \dot{\chi}_\alpha}$ as

$$\frac{\partial \mathcal{D}}{\partial \dot{\boldsymbol{\chi}}} = \frac{1}{\mathcal{B}_o}\left[\sum_{i=1,M} \frac{\partial D_{\mathcal{N}}}{\partial \dot{l}^i}\frac{\partial \dot{l}^i}{\partial \dot{\mathbf{l}}^i}\frac{\partial \dot{\mathbf{l}}^i}{\partial \dot{\boldsymbol{\chi}}} + \frac{1}{2}\sum_{i=1,M}\sum_{j=1,M} \frac{\partial D_{\mathcal{M}}}{\partial \dot{\psi}^{ij}}\left(\frac{\partial \dot{\psi}^{ij}}{\partial \dot{\mathbf{l}}^i}\frac{\partial \dot{\mathbf{l}}^i}{\partial \dot{\boldsymbol{\chi}}} + \frac{\partial \dot{\psi}^{ij}}{\partial \dot{\mathbf{l}}^j}\frac{\partial \dot{\mathbf{l}}^j}{\partial \dot{\boldsymbol{\chi}}}\right)\right] \tag{2.61}$$

Recalling that $-\frac{\partial D_{\mathcal{N}}(\dot{l}^i)}{\partial \dot{l}^i} = \mathcal{N}_i^\eta$ and $-\frac{D_{\mathcal{M}}(\dot{\psi}^{ij})}{\partial \dot{\psi}^{ij}} = \mathcal{M}_{ij}^\eta$ from Equation 2.37 and also recalling that

$$\frac{\partial \dot{l}^i}{\partial \dot{\mathbf{l}}^i} = \mathbf{e}^{l^i} \quad \text{and} \quad \frac{\partial \dot{\psi}^{ij}}{\partial \dot{\mathbf{l}}^i} = \frac{\mathbf{e}^{l^i l^j}}{l^i} \tag{2.62}$$

from Equations 2.18 and 2.33. Now we can rewrite $\frac{\partial \mathcal{D}}{\partial \dot{\boldsymbol{\chi}}}$ as

$$\frac{\partial \mathcal{D}}{\partial \dot{\boldsymbol{\chi}}} = -\frac{1}{\mathcal{B}_o}\left[\sum_{i=1,M}\left(\mathcal{N}_i^\eta \mathbf{e}^{l^i} + \frac{1}{l^i}\sum_{j=1,M}\mathcal{M}_{ij}^\eta \mathbf{e}^{l^i l^j}\right)\frac{\partial \dot{\mathbf{l}}^i}{\partial \dot{\boldsymbol{\chi}}}\right] \tag{2.63}$$

or in term of components the above derivative takes the form

$$\frac{\partial \mathcal{D}}{\partial \dot{\chi}_\alpha} = -\frac{1}{\mathcal{B}_o}\left[\sum_{i=1,M}\left(\mathcal{N}_i^\eta e_m^{l^i} + \frac{1}{l^i}\sum_{j=1,M}\mathcal{M}_{ij}^\eta e_m^{l^i l^j}\right)\left(\frac{\partial \dot{l}_m^i}{\partial \dot{\chi}_\alpha}\right)\right] \tag{2.64}$$

From $\dot{l}_m^i = \dot{F}_{kK} L_K^i - \dot{\chi}_m$ we have

$$\frac{\partial \dot{l}_m^i}{\partial \dot{\chi}_\alpha} = -\delta_{\alpha m} \tag{2.65}$$

Therefore the derivative of the dissipated viscous energy with respect to the components of $\dot{\chi}_\alpha$, the dissipative forces Q_α $(= \frac{\partial \mathcal{D}}{\partial \dot{\chi}_\alpha})$ can be written as

$$\begin{aligned}\frac{\partial \mathcal{D}}{\partial \dot{\chi}_\alpha} &= \frac{1}{\mathcal{B}_o}\left[\sum_{i=1,M}\left(\mathcal{N}_i^\eta e_\alpha^{l^i} + \frac{1}{l^i}\sum_{j=1,M}\mathcal{M}_{ij}^\eta e_\alpha^{l^i l^j}\right)\right] \\ &= \frac{1}{\mathcal{B}_o}\left[\sum_{i=1,M}\left(\mathcal{N}_i^\eta e_\alpha^{l^i} + \mathcal{V}_i^\eta e_\alpha^{\bar{l^i}}\right)\right] \\ &= \frac{1}{\mathcal{B}_o}\left[\sum_{i=1,M} f_\alpha^{\eta,i}\right]\end{aligned} \tag{2.66}$$

In the expression above, recall that $\mathcal{D}$ represents the dissipative potential defined in Equation 2.36 and $\mathcal{N}_i^\eta$ and $\mathcal{M}_i^\eta$ are the viscous forces and moments respectively which were defined in Equation 2.37. In the last equation above the term $f_\alpha^{\eta,i}$ represents the Cartesian component α of the *viscous* axial $\mathcal{N}_i^\eta$ and shear $\mathcal{V}_i^\eta$ forces from ligament i applied at the vertex of the unit cell.

Equilibrium Condition

We are now ready to apply the principle of stationary action to obtain the equilibrium condition which will define the kinematic state of the unit cells in the microstructure. Replacing Equations 2.50, 2.52, 2.59 and 2.66 into the principle of stationary action given in Equation 2.42, we obtain

$$\begin{aligned}&\frac{1}{\mathcal{B}_o}\left(\sum_{i=1,M} L^i \int_0^1 \tilde{\rho}_s^i \; a^i_{\text{affine},\alpha}\; (1-\zeta^i)\; \mathrm{d}\zeta^i + m_c\; \ddot{\chi}_\alpha\right) - \frac{1}{\mathcal{B}_o}\left[\sum_{i=1,M} f_\alpha^{E,i}\right] \\ &\quad -\frac{1}{\mathcal{B}_o}\sum_{i=1,M} L^i \int_0^1 \tilde{\rho}_s^i a^i_{\text{affine},\alpha}\; (1-\zeta^i)\; \mathrm{d}\zeta^i = \frac{1}{\mathcal{B}_o}\left[\sum_{i=1,M} f_\alpha^{\eta,i}\right]\;.\end{aligned} \tag{2.67}$$

The above expression is the equation of motion for the vertex of the unit cell which is a second order system of nonlinear ordinary differential equations for $\boldsymbol{\chi}(\mathbf{X}, t)$. We can express the above equation of motion as a dynamic equilibrium condition by simplifying and rearranging the terms into a resultant $(\mathcal{R}_\alpha)$ of the elastic, viscous, and inertial forces at the vertex as

$$\mathcal{R}_\alpha = \sum_{i=1,M}\left(f_\alpha^{E,i} + f_\alpha^{\eta,i}\right) - m_c\ddot{\chi}_\alpha = 0 \qquad \text{with } \alpha = 1,3 \tag{2.68}$$

or in vector form as

$$\boldsymbol{\mathcal{R}} = \sum_{i=1,M} \left(\mathbf{f}^{E,i} + \mathbf{f}^{\eta,i} \right) - m_c \ddot{\boldsymbol{\chi}} = 0 \tag{2.69}$$

In equation 2.68 above, $(f_\alpha^{\eta,i} + f_\alpha^{\eta,i})$ represent the sum at the cell vertex of the *elastic* and *viscous* forces respectively for ligament i and $m_c \ddot{\chi}_\alpha$ represents the effective microinertia for the unit cell given by the motion of the vertex. This condition provides the link between the macroscopic fields and the intra-cell ones, and allows us to univocally define the stress state for an applied macroscopic deformation field as described in Section 2.3.4. In particular, this condition allows us to write that $\mathcal{W} = \mathcal{W}(\mathbf{F})$ and $\mathcal{D} = \mathcal{D}(\dot{\mathbf{F}})$.

2.3.4 Macroscopic Stresses

Once both the elastic and the viscous potentials are univocally defined in terms of the macroscopic fields and the kinematic state of the cells in the microstructure is determined by enforcing the equilibrium condition stated in Equation 2.68, the constitutive relation $\tilde{\mathbf{P}}(\mathbf{F}(t))$ can be obtained. In particular, the First Piola-Kirchhoff stress tensor $\mathbf{P} = \tilde{\mathbf{P}}(\mathbf{F}(t))$ emerges as the derivative with respect to $\mathbf{F}$ and $\dot{\mathbf{F}}$ of the *elastic* $\mathcal{W}(\mathbf{F})$ and *viscous* $\mathcal{D}(\dot{\mathbf{F}})$ potentials respectively.

$$P_{kK}(\mathbf{F}(t)) = \frac{\partial \mathcal{W}(\mathbf{F})}{\partial F_{kK}} + \frac{\partial \mathcal{D}(\dot{\mathbf{F}})}{\partial \dot{F}_{kK}} \tag{2.70}$$

$P_{kK}(\mathbf{F}(t))$ represents the Cartesian components of the First Piola Kirchhoff stress tensor and $\frac{\partial \mathcal{W}(\mathbf{F})}{\partial F_{kK}}$ and $\frac{\partial \mathcal{D}(\dot{\mathbf{F}})}{\partial \dot{F}_{kK}}$ are respectively the Cartesian components of the elastic and viscous contributions to the total stress state. The elastic contribution to the stress tensor is written as

$$\begin{aligned} \frac{\partial \mathcal{W}(\mathbf{F})}{\partial F_{kK}} &= \frac{1}{\mathcal{B}_o} \left[\sum_{i=1,M} \left(\mathcal{N}_i^E e_\alpha^{l^i} + \frac{1}{l^i} \sum_{j=1,M} \mathcal{M}_{ij}^E e_\alpha^{l^i l^j} \right) \frac{\partial l_\alpha^i}{\partial F_{kK}} \right] \\ &= \frac{1}{\mathcal{B}_o} \left[\sum_{i=1,M} f_\alpha^{E,i} \frac{\partial l_\alpha^i}{\partial F_{kK}} \right] \end{aligned} \tag{2.71}$$

and the viscous contribution to the stress tensor is written as

$$\frac{\partial \mathcal{D}(\dot{\mathbf{F}})}{\partial \dot{F}_{kK}} = \frac{1}{\mathcal{B}_o} \left[\sum_{i=1,M} \left(\mathcal{N}_i^\eta e_\alpha^{l^i} + \frac{1}{l^i} \sum_{j=1,M} \mathcal{M}_{ij}^\eta e_\alpha^{l^i l^j} \right) \frac{\partial \dot{l}_\alpha^i}{\partial \dot{F}_{kK}} \right]$$

$$= \frac{1}{\mathcal{B}_o}\left[\sum_{i=1,M} f_\alpha^{\eta,i}\frac{\partial \dot{l}_\alpha^i}{\partial \dot{F}_{kK}}\right] . \tag{2.72}$$

Remembering Equations 2.13 and 2.15, the derivatives $\frac{\partial l_\alpha^i}{\partial F_{kK}}$ and $\frac{\partial \dot{l}_\alpha^i}{\partial \dot{F}_{kK}}$ can be evaluated as

$$\frac{\partial l_\alpha^i}{\partial F_{kK}} = \delta_{\alpha k} L_K^i - \frac{\partial \chi_\alpha}{\partial F_{kK}} \quad and \quad \frac{\partial \dot{l}_\alpha^i}{\partial \dot{F}_{kK}} = \delta_{\alpha k} L_K^i - \frac{\partial \dot{\chi}_\alpha}{\partial \dot{F}_{kK}} . \tag{2.73}$$

Using these expressions we can restate the stress tensor as

$$P_{kK}(\mathbf{F}(t)) = \frac{1}{\mathcal{B}_o}\left[\sum_{i=1,M}\left(f_k^{E,i}L_K^i + f_k^{\eta,i}L_K^i\right) - \sum_{i=1,M}\left(f_\alpha^{E,i}\frac{\partial \chi_\alpha}{\partial F_{kK}} + f_\alpha^{\eta,i}\frac{\partial \dot{\chi}_\alpha}{\partial \dot{F}_{kK}}\right)\right] \tag{2.74}$$

Additionally since Equation 2.68 implicitly provides a relationship between $\boldsymbol{\chi}$ and $\mathbf{F}$, it is possible then to write that $\boldsymbol{\chi} = h(\mathbf{F})$ and thus $\dot{\boldsymbol{\chi}} = h' \, \dot{\mathbf{F}}$ which allow us to write

$$\frac{\partial \chi_\alpha}{\partial F_{kK}} = \frac{\partial \dot{\chi}_\alpha}{\partial \dot{F}_{kK}} = h' . \tag{2.75}$$

Introducing Equation 2.75 into Equation 2.74 and then using Equation 2.68 results in the following expression for the stress tensor.

$$\begin{aligned} P_{kK}(\mathbf{F}(t)) &= \frac{1}{\mathcal{B}_o}\left[\sum_{i=1,M}\left(f_k^{E,i}L_K^i + f_k^{\eta,i}L_K^i\right) - \frac{\partial \chi_\alpha}{\partial F_{kK}}\sum_{i=1,M}\left(f_\alpha^{E,i} + f_\alpha^{\eta,i}\right)\right] \\ &= \frac{1}{\mathcal{B}_o}\left[\sum_{i=1,M}\left(f_k^{E,i}L_K^i + f_k^{\eta,i}L_K^i\right) - m_c\frac{\partial \chi_\alpha}{\partial F_{kK}}\ddot{\chi}_\alpha\right] \end{aligned} \tag{2.76}$$

or in vector form

$$\mathbf{P}(\mathbf{F}(t)) = \frac{1}{\mathcal{B}_o}\left[\sum_{i=1,M}\left(\mathbf{f}^{E,i}\otimes\mathbf{L}^i + \mathbf{f}^{\eta,i}\otimes\mathbf{L}^i\right) - m_c\frac{\partial \boldsymbol{\chi}}{\partial \mathbf{F}}\cdot\ddot{\boldsymbol{\chi}}\right] \tag{2.77}$$

Equation 2.76 above is the final expression for the effective First Piola-Kirchhoff stress tensor for a dynamically loaded visco-elastic, open-cell foam material. Notice that this stress tensor includes the elastic and viscous contributions $\frac{1}{\mathcal{B}_o}\sum_{i=1,M}(f_k^{E,i}L_K^i + f_k^{\eta,i}L_K^i)$ and the inertial contribution $\frac{1}{\mathcal{B}_o}\frac{\partial \chi_\alpha}{\partial F_{kK}}m_c\ddot{\chi}_\alpha$. As the predictions will show, the inertial stresses due to the non-affine acceleration are especially important during cell collapse at exceptionally high strain rates. Equations 2.76 and 2.77 above reduce to the previously reported version of this model for quasi-statically loaded elastic foams (Wang and Cuitiño, 2000).

Material Frame Indifference

The formulated constitutive relation $\tilde{\mathbf{P}}(\mathbf{F})$ given in Equation 2.77 satisfies the principle of material frame indifference, where the material behavior is unaffected by a superposed rigid body rotation $\mathbf{R}$. Recall that enforcing the principle of minimum action gave us the unit cell kinematic state condition stated in Equation 2.69 and repeated below for convenience

$$\mathcal{R}(\mathbf{F},\boldsymbol{\chi}) = \sum_{i=1,M}\left(\mathbf{f}^{E,i}+\mathbf{f}^{\eta,i}\right) - m_c\ddot{\boldsymbol{\chi}} = 0 \quad \Rightarrow \quad \boldsymbol{\chi} = \tilde{\boldsymbol{\chi}}(\mathbf{F}). \tag{2.78}$$

In order to be consistent with the principle of *frame indifference*, we first show that for a rigid rotation $\mathbf{R}$ such that $\mathbf{F}^* = \mathbf{RF}$, the rotated kinematic state of the unit cell is also in equilibrium. Namely that

$$\mathcal{R}(\mathbf{F}^*,\boldsymbol{\chi}^*) = 0 \quad \Rightarrow \quad \boldsymbol{\chi}^* = \tilde{\boldsymbol{\chi}}(\mathbf{F}^*) \tag{2.79}$$

is also satisfied if $\boldsymbol{\chi}^* = \mathbf{R}\boldsymbol{\chi}$. Recall that $\boldsymbol{\chi}$ is just a 3D vector for the current position of the unit cell vertex, therefore let's assume that

$$\boldsymbol{\chi}^* = \mathbf{R}\boldsymbol{\chi} \quad \Rightarrow \quad \dot{\boldsymbol{\chi}}^* = \mathbf{R}\dot{\boldsymbol{\chi}} \quad \Rightarrow \quad \ddot{\boldsymbol{\chi}}^* = \mathbf{R}\ddot{\boldsymbol{\chi}}. \tag{2.80}$$

Now recall that the current ligament vectors for each ligament composing the unit cell are given by $\mathbf{l}^i = \mathbf{l}^i(\mathbf{F}) = \mathbf{FL}^i - \tilde{\boldsymbol{\chi}}(\mathbf{F})$, then the rotated current ligament vectors are

$$\begin{aligned}
\mathbf{l}^{i^*} &= \mathbf{l}^i(\mathbf{F}^*) = \mathbf{F}^*\mathbf{L}^i - \tilde{\boldsymbol{\chi}}(\mathbf{F}^*) \\
&= \mathbf{F}^*\mathbf{L}^i - \boldsymbol{\chi}^* \\
&= \mathbf{RFL}^i - \mathbf{R}\boldsymbol{\chi} \\
&= \mathbf{R}[\mathbf{FL}^i - \boldsymbol{\chi}].
\end{aligned}$$

Noticing that the term inside the square brackets above is the un-rotated current ligament vector, we write that

$$\mathbf{l}^{i^*} = \mathbf{Rl}^i \tag{2.81}$$

which then implies that

$$\mathbf{e}^{l_i^*} = \mathbf{Re}^{l_i} \quad \textit{and} \quad \mathbf{e}^{l_i^* l_j^*} = \mathbf{Re}^{l_i l_j} \tag{2.82}$$

because $\mathbf{e}^{l_i^*}$ and $\mathbf{e}^{l_i^* l_j^*}$ are simply unit vectors defined by the current leg vectors $\mathbf{l}^i$ and $\mathbf{l}^j$.

The magnitude of the axial and shear forces from each ligament depend only on the magnitude of the length of each leg and the magnitude of the angle between legs. Therefore the magnitude of the forces doesn't change due to a rigid rotation $\mathbf{R}$. As shown by Wang and Cuitiño (2000) for the elastic forces, the force vectors $\mathbf{f}^{E,i}$ and $\mathbf{f}^{\eta,i}$ are the sum of the product of the axial and shear force magnitudes times the unit vectors mentioned above in equation 2.82. This implies that if the unit vectors rotate as mentioned above in equation 2.82 then the rotated elastic and viscous force vectors in $\mathcal{R}^*(\mathbf{F}^*, \boldsymbol{\chi}^*) = 0$ are

$$\mathbf{f}^{E,i^*} \;=\; \mathbf{R}\mathbf{f}^{E,i} \quad \textit{and} \quad \mathbf{f}^{\eta,i^*} \;=\; \mathbf{R}\mathbf{f}^{\eta,i}. \tag{2.83}$$

Now consider the rotated kinematic state and lets make use of Equations 2.80, 2.81, 2.82, and 2.83.

$$\begin{aligned} \mathcal{R}(\mathbf{F}^*, \boldsymbol{\chi}^*) &= \sum_{i=1,M} \mathbf{f}^{E,i^*} + \mathbf{f}^{\eta,i^*} - m_c \boldsymbol{\chi}^* \\ &= \sum_{i=1,M} \mathbf{R}\mathbf{f}^{E,i} + \mathbf{R}\mathbf{f}^{\eta,i} - m_c \mathbf{R}\ddot{\boldsymbol{\chi}} \\ &= \mathbf{R}\left\{ \sum_{i=1,M} \mathbf{f}^{E,i} + \mathbf{f}^{\eta,i} - m_c \ddot{\boldsymbol{\chi}} \right\} \end{aligned} \tag{2.84}$$

Noticing that the term in curly brackets above corresponds to the un-rotated kinematic equilibrium stated in Equation 2.78, we can write that $\mathcal{R}(\mathbf{F}^*, \boldsymbol{\chi}^*) \;=\; \mathbf{R}\{\mathcal{R}(\mathbf{F}, \boldsymbol{\chi})\}$which then implies that rotated kinematic state is also in equilibrium

$$\mathcal{R}(\mathbf{F}^*, \boldsymbol{\chi}^*) = \sum_{i=1,M} \mathbf{f}^{E,i^*} + \mathbf{f}^{\eta,i^*} - m_c \boldsymbol{\chi}^* = 0 \tag{2.85}$$

The above expression dictates that if $\mathbf{F}^* \;=\; \mathbf{R}\mathbf{F}$, then $\boldsymbol{\chi}^* \;=\; \mathbf{R}\boldsymbol{\chi}$.

Now we show that the derived effective stress state obeys the principle of *frame indifference*. We have

$$\mathbf{P} = \tilde{\mathbf{P}}(\mathbf{F}, \dot{\mathbf{F}}) \quad \Rightarrow \quad \mathbf{P} = \tilde{\mathbf{P}}(\mathbf{F}(t)) \tag{2.86}$$

Recall the un-rotated stress state in component form

$$P_{sK} = \tilde{\mathbf{P}}(F_{sK}) = \frac{1}{\mathcal{B}_o}\left[\sum_{i=1,M}(f_s^{E,i}L_K + f_s^{\eta,i}L_K) - \frac{\partial\chi_\alpha}{\partial F_{sK}}m_c\ddot{\chi}_\alpha\right] \tag{2.87}$$

Similarly, the rotated stress state in component can written as

$$P^*_{lK} = \tilde{\mathbf{P}}(F^*_{lK}) = \frac{1}{\mathcal{B}_o}\left[\sum_{i=1,M}(f_l^{E,i^*}L_K + f_l^{\eta,i^*}L_K) - \frac{\partial\chi^*_\beta}{\partial F^*_{lK}}m_c\ddot{\chi}^*_\beta\right]. \tag{2.88}$$

Now Let's consider a rigid body rotation $\mathbf{R}$ with components R_{ls} such that $F^*_{lK} = R_{ls}F_{sK}$ ($\mathbf{F}^* = \mathbf{RF}$). First let's look at the 2nd term in Equation 2.88 without m_c, the effective mass constant located at the unit cell vertex.

$$\frac{\partial\chi^*_\beta}{\partial F^*_{lK}}\ddot{\chi}^*_\beta = \frac{\partial\chi^*_\beta}{\partial\chi_\alpha}\frac{\partial\chi_\alpha}{\partial F_{sK}}\frac{\partial F_{sK}}{\partial F^*_{lK}}\ddot{\chi}^*_\beta \tag{2.89}$$

Remembering that $\chi^*_\beta = R_{\beta\alpha}\chi_\alpha$ dictates that $\ddot{\chi}^* = R_{\beta\alpha}\ddot{\chi}_\alpha$ as stated in Equation 2.80. Now performing the multiplication $\mathbf{R}^{-1}(\mathbf{F}^* = \mathbf{RF})$ in component form and remembering that $\mathbf{R}^{-1} = \mathbf{R}^T$ and $\mathbf{R}^T\mathbf{R} = \mathbf{I}$ gives

$$\begin{aligned} R^{-1}_{sl}F^*_{lK} &= R^{-1}_{sl}R_{lm}F_{mK} \\ &= \delta_{sm}F_{mK} \\ &= F_{sK} \\ R_{ls}F^*_{lK} &= F_{sK} \end{aligned}$$

then

$$\frac{\partial F_{sK}}{\partial F^*_{lK}} = R_{ls}. \tag{2.90}$$

Now Equation 2.89 can be restated as

$$\frac{\partial\chi^*_\beta}{\partial F^*_{lK}}\ddot{\chi}^*_\beta = R_{\beta\alpha}\frac{\partial\chi_\alpha}{\partial F_{sK}}R_{ls}R_{\beta\delta}\ddot{\chi}_\delta \tag{2.91}$$

$$= R_{\beta\alpha}R_{\beta\delta}R_{ls}\frac{\partial\chi_\alpha}{\partial F_{sK}}\ddot{\chi}_\delta \tag{2.92}$$

Noticing that $R_{\beta\alpha}R_{\beta\delta} = \delta_{\alpha\delta}$, we can write

$$\begin{aligned} \frac{\partial\chi^*_\beta}{\partial F^*_{lK}}\ddot{\chi}^*_\beta &= \delta_{\alpha\delta}R_{ls}\frac{\partial\chi_\alpha}{\partial F_{sK}}\ddot{\chi}_\delta \\ &= R_{ls}\frac{\partial\chi_\alpha}{\partial F_{sK}}\ddot{\chi}_\alpha \end{aligned} \tag{2.93}$$

Now consider the 1st term in Equation 2.88, applying Equation 2.83 gives us

$$\sum_{i=1,M} (f_l^{E,i^*} L_K + f_l^{\eta,i^*} L_K) = \sum_{i=1,M} (R_{ls} f_l^{E,i} L_K + R_{ls} f_l^{\eta,i} L_K). \tag{2.94}$$

Substituting 2.93 and 2.94 into 2.88 gives

$$P^*_{lK} = \frac{1}{\mathcal{B}_o} \left[\sum_{i=1,M} (R_{ls} f_l^{E,i} L_K + R_{ls} f_l^{\eta,i} L_K) - R_{ls} \frac{\partial \chi_\alpha}{\partial F_{sK}} m_c \ddot{\chi}_\alpha \right] \tag{2.95}$$

$$= R_{ls} \left\{ \frac{1}{\mathcal{B}_o} \left[\sum_{i=1,M} (f_l^{E,i} L_K + f_l^{\eta,i} L_K) - \frac{\partial \chi_\alpha}{\partial F_{sK}} m_c \ddot{\chi}_\alpha \right] \right\} \tag{2.96}$$

Noticing that the term in curly brackets above is the un-rotated stress state, P_{sK}, means that

$$P^*_{sk} = R_{ls} P_{sK} \qquad or \qquad \mathbf{P}^* = \mathbf{R}\mathbf{P}. \tag{2.97}$$

Therefore

$$\mathbf{P} = \mathbf{R}^{-1}\mathbf{P}^* \qquad \Rightarrow \qquad \tilde{\mathbf{P}}(\mathbf{F}) = \mathbf{R}^{-1}\tilde{\mathbf{P}}(\mathbf{R}\mathbf{F}) \tag{2.98}$$

This demonstrates that the effective stress state equation that we have derived for an open-cell foam material obeys the principle of *frame indifference*.

2.4 Predictions of the Theory

This section presents a specific application of the general framework developed in Section 2.3. Here, the formulation is utilized to predict the effective mechanical response of polymeric foams with visco-elastic constitutive cell wall behavior for homogeneous conditions of global applied deformation. In order to obtain the resulting predictions it is necessary to select a specific unit cell geometry along with the properties and constitutive laws for the material composing the ligaments of the cells. Therefore, Section 2.4.1 will describe the chosen unit cell geometry and the form adopted for the elastic and viscous potentials which dictate the axial and bending constitutive response of the ligaments composing the unit cell through Equations 2.35 and 2.37. Then, Section 2.4.2 presents the effective response of a small groups of cells and then evaluates the effective foam response, including the plateau stress, employing the concept of Maxwell stress. Using these results, we quantify the role of strain rate, cell geometry and ligament

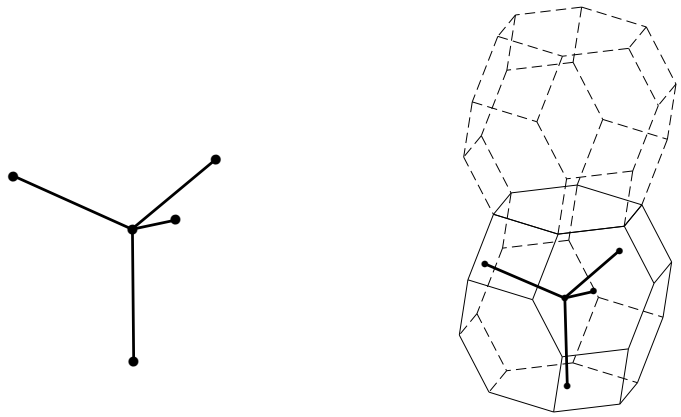

Figure 2.5: (a) Four ligament unit cell and (b) unit cell with its dual tetrakaidecahedron representative volume, (Wang and Cuitiño, 2000).

properties for dynamic uniaxial compression under macroscopically homogeneous conditions. Finally, the predictions are contrasted with the available experimental data to verify the validity of the formulation.

2.4.1 Cell Geometry and Ligament Response

Consider a unit cell composed of four ligaments ($M = 4$) converging at the cell's vertex and occupying a dual tetrakaidecahedron volume element as shown in Figure 2.5. Figure 2.5a shows the solid phase of the unit cell and Figure 2.5b shows the portion of the foam volume corresponding to each unit cell. The ligaments composing the unit cell are taken as cylindrical rods of length L and radius r. The initial ligament orientations stated in Equation 2.1 are selected as

$$\begin{aligned}
\mathbf{L}^1 &= L^1\left(\frac{2\sqrt{2}}{2}\mathbf{z}^2 + \frac{1}{3}\mathbf{z}^3\right) \\
\mathbf{L}^2 &= L^2\left(\frac{\sqrt{6}}{3}\mathbf{z}^1 - \frac{\sqrt{2}}{3}\mathbf{z}^2 + \frac{1}{3}\mathbf{z}^3\right) \\
\mathbf{L}^3 &= L^3\left(\frac{-\sqrt{6}}{3}\mathbf{z}^1 - \frac{\sqrt{2}}{3}\mathbf{z}^2 + \frac{1}{3}\mathbf{z}^3\right) \\
\mathbf{L}^4 &= L^4\left(-\mathbf{z}^3\right)
\end{aligned} \tag{2.99}$$

where L^1 to L^4 represent the initial half length of each ligament while the terms in parenthesis are unit vectors describing the initial ligament orientation. $\mathbf{z}^i$ is a local Cartesian coordinate basis centered at the vertex of the unit cell.

It is necessary to select an specific form for the axial elastic potential $W_{\mathcal{N}}(l^i)$ and the bending elastic potential $W_{\mathcal{M}}(\psi^{ij})$ stated in Equation 2.34 in order to apply Equation 2.35 to obtain the elastic constitutive relations for the ligaments composing the unit cells. The axial elastic potential is taken as

$$W_{\mathcal{N}}(l^i) = \Lambda_c L^i \mathcal{N}_c^E \left\{ \frac{\Lambda^i}{\Lambda_c} \sinh^{-1}\left(\frac{\Lambda^i}{\Lambda_c}\right) - \sqrt{\left(\frac{\Lambda^i}{\Lambda_c}\right)^2 + 1} \right\} \tag{2.100}$$

where $\Lambda^i = l^i/L^i - 1$ is the ligament axial strain, $\mathcal{N}_c^E = EA\Lambda_c$ is the characteristic elastic axial force, which is written in terms of the ligament's Young Modulus E, cross sectional area A ($= \pi r^2$ for circular cross sections of radius r) and a characteristic elastic strain Λ_c which controls the degree of nonlinearity. After application of Equation 2.35, the elastic axial force $\mathcal{N}_i^E$ for each ligament i becomes

$$\mathcal{N}_i^E(l^i) = \mathcal{N}_c^E \sinh^{-1}\left(\frac{\Lambda^i}{\Lambda_c}\right) \tag{2.101}$$

which is a non-linear (*depending on* Λ_c) function of the current ligament half length l^i. The elastic bending potential is similarly taken as

$$W_{\mathcal{M}}(\psi^{ij}) = \Xi_c \mathcal{M}_c^E \left\{ \frac{\Xi^{ij}}{\Xi_c} \sinh^{-1}\left(\frac{\Xi^{ij}}{\Xi_c}\right) - \sqrt{\left(\frac{\Xi^{ij}}{\Xi_c}\right)^2 + 1} \right\} \tag{2.102}$$

where $\Xi^{ij} = \psi^{ij} - \Psi^{ij}$ is the change in angle and $\mathcal{M}_c^E = 3EI\Xi_c L^{-1}$ is the characteristic elastic bending moment, which is written in terms of the ligament's Young Modulus E, moment of inertia I ($= \pi r^4/4$ for circular cross sections of radius r), length L, and a characteristic angle Ξ_c which controls the degree of nonlinearity. After application of Equation 2.35, the elastic bending moment $\mathcal{M}_{ij}^E$ between any two ligaments i and j becomes

$$\mathcal{M}_{ij}^E(\psi^{ij}) = \mathcal{M}_c^E \sinh^{-1}\left(\frac{\Xi^{ij}}{\Xi_c}\right) \tag{2.103}$$

which is a non-linear (*depending on* Ξ_c) function of the current angle ψ^{ij} between the two ligaments. We have selected the $sinh^{-1}$ relations in the expressions above because they can be adapted to provide highly nonlinear behavior.

Finally, it is also necessary to select an specific form for the axial dissipative potential $D_{\mathcal{N}}(\dot{l}^i)$ and the bending dissipative potential $D_{\mathcal{M}}(\dot{\psi}^{ij})$ stated in Equation 2.36 in order to apply Equation 2.37 to obtain the viscous constitutive relations for the ligaments composing the unit cells. The axial viscous potential is taken

$$D_{\mathcal{N}}(\dot{l}^i) = \dot{\Lambda}_c L^i \mathcal{N}_c^E \left\{ \frac{\dot{\Lambda}^i}{\dot{\Lambda}_c} \sinh^{-1}\left(\frac{\dot{\Lambda}^i}{\dot{\Lambda}_c}\right) - \sqrt{\left(\frac{\dot{\Lambda}^i}{\dot{\Lambda}_c}\right)^2 + 1} \right\} \tag{2.104}$$

where $\dot{\Lambda}^i = \dot{l}^i / L^i$ is the ligament axial strain rate, $\mathcal{N}_c^\eta = \eta A \dot{\Lambda}_c$ is the characteristic viscous axial force, which is written in terms of the ligament's viscosity η, cross sectional area A and a characteristic strain rate $\dot{\Lambda}_c$ which determines the degree of nonlinearity. After application of Equation 2.37, the axial viscous force $\mathcal{N}_i^\eta$ takes the form

$$\mathcal{N}_i^\eta(\dot{l}^i) = \mathcal{N}_c^\eta \sinh^{-1}\left(\frac{\dot{\Lambda}^i}{\dot{\Lambda}_c}\right) \tag{2.105}$$

This is a non-linear (*depending on* $\dot{\Lambda}_c$) function of the rate of change of the ligament half length $\dot{l}^i$. The bending dissipative potential is similarly taken as

$$W_{\mathcal{M}}(\dot{\psi}^{ij}) = \dot{\Xi}_c \mathcal{M}_c^E \left\{ \frac{\dot{\Xi}^{ij}}{\dot{\Xi}_c} \sinh^{-1}\left(\frac{\dot{\Xi}^{ij}}{\dot{\Xi}_c}\right) - \sqrt{\left(\frac{\dot{\Xi}^{ij}}{\dot{\Xi}_c}\right)^2 + 1} \right\} \tag{2.106}$$

where $\dot{\Xi}^{ij} = \dot{\psi}^{ij}$ is the rate of angle change between ligaments i and j and $\mathcal{M}_c^\eta = 3\eta I \dot{\Xi}_c L^{-1}$ is the characteristic viscous bending moment, which is written in terms of the ligament's viscosity η, inertia moment I, length L, and a characteristic rate of angle change $\dot{\Xi}_c$ which again controls the degree of nonlinearity. After application of Equation 2.37, the viscous bending moment $\mathcal{M}_{ij}^\eta$ between any two ligaments i and j takes the form

$$\mathcal{M}_{ij}^\eta(\dot{\psi}^{ij}) = \mathcal{M}_c^\eta \sinh^{-1}\left(\frac{\dot{\Xi}^{ij}}{\dot{\Xi}_c}\right) \tag{2.107}$$

Again, this is a function nonlinear (*depending on* $\dot{\Xi}_c$) of the rate of change of the angle $\dot{\psi}^{ij}$ between two ligaments.

It is worthwhile to notice that the framework presented in here allows for the incorporation of any ligament constitutive response. In the examples presented in this section, we have chosen a local constitutive law defined by $\sinh^{-1}$ which follows a prototypical material response characterized by a stiff linear regime at low strains followed by

a softer non-linear response at larger strains. As reported in Wang and Cuitiño (2000), the extent of linear regime is determined by the selection of the characteristic parameters Λ_c, $\dot{\Lambda}_c$, Ξ_c and $\dot{\Xi}_c$ for the elastic/viscous force/moment relations respectively. In addition, we have assumed that the elastic and viscous potentials are decoupled. However, other forms of the potentials can be implemented. For example, the response of typical metals can be incorporated by formulating a coupled elatico-visco-plastic potential as done in chapter 3.

2.4.2 Effective Theoretical Predictions

This section presents a set of effective predictions based solely on the micromechanical model formulated in Section 2.3. The effective predictions presented here correspond to a nominal strain rate without accounting for the variation in local strain rate in an actual foam specimen. The effective response is obtained by first obtaining the response of a small group of cells and then evaluating the plateau stress employing the Maxwell stress idea. A brief overview of the procedure that was used to obtain the Maxwell (plateau) stress is presented in Appendix A. Using the effective predictions, we quantify the role of *strain rate*, ligament material properties, and cell geometry (relative density) for *dynamic* uniaxial compression under macroscopic homogeneous conditions. These predictions are also contrasted with some of the available experimental studies to verify the validity of our formulation.

Figure 2.6 shows the model's prediction for the effects of strain rate on the effective response of a visco-elastic open-cell foam. Figure 2.6a shows the effective local response prediction and Figure 2.6b shows the effective response with the plateau stress evaluated as the Maxwell stress. According to Figure 2.6b, the model predicts an increase in the plateau stress as the strain rate increases with a stronger effect for extremely high strain rates. Figure 2.6b also predicts that as the strain rate increases both the length of the plateau region and the initial slope (the Youngs Modulus of the foam) increase as the strain rate increases. Finally, Figure 2.6 demonstrates that the effects of strain rate are a lot stronger at extremely high strain rates ($\dot{\epsilon} > 50000\ s^{-1}$).

Experimentally, the exact mechanisms operating at high strain rates during

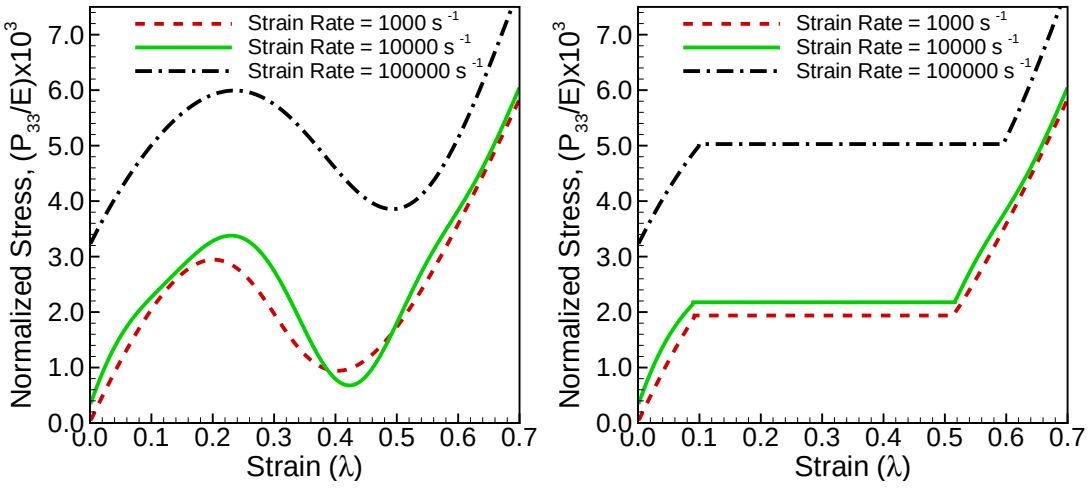

(a) Predicted effective response

(b) Effective response w/ Collapse Stress

Figure 2.6: The effects of strain rate on visco-elastic open-cell foams. (a) Predicted effective response. (b) Effective response after evaluation of the Maxwell stress which is identified as the plateau or collapse stress. The other microstructural parameters were held constant: Young's Modulus (E) $= 1.0 \times 10^9 \frac{N}{m^2}$, Foam density ($\rho$) $= 100.0 \frac{Kg}{m^3}$, cell ligament viscosity (η) $= 1000.0 \frac{N \cdot s}{m^2}$, cell ligament radius ($r$) $= 0.34$ mm, cell ligament length (L) $= 1.0$ mm.

collapse in foam materials are still unclear, however most experimental studies agree that the higher the applied strain rate, the higher the plateau stress, at least for the range of rates (up to $\dot{\epsilon} = 5000\ s^{-1}$) for which data is available. Rinde and Hoge (1971) studied the compressive strength of rigid poly-styrene foams at room temperature as a function of strain rate and showed that the strength increases slightly with increasing strain rate with similar conclusions being reached by Nagy et al. (1974). Kanahashi et al. (2000) concluded that plateau stress normalized by the relative density and the absorbed energy drastically increased based on dynamic compression experiments ($\dot{\epsilon} = 1.4x \times 10^3 s^{-1}$) of very low density aluminum foams. Yi et al. (2001) showed that the collapse stress of aluminum foams increases with increasing strain rate, but this effect becomes less pronounced as the relative density of the foam decreases. Higher strain rate (up to 5000 s^{-1}) compression experiments were done by Deshpande and Fleck (2000a); however, they concluded that strain rate had no effect on the plateau stress. Studies for open-cell metallic foams and textile/pyramidal truss cores with strain rates up to $10000 s^{-1}$ using a Kolsky bar and a Gas Gun were recently reported by Lee et al. (2006b,a). They concluded that strain has very minimal effects on the collapse stress

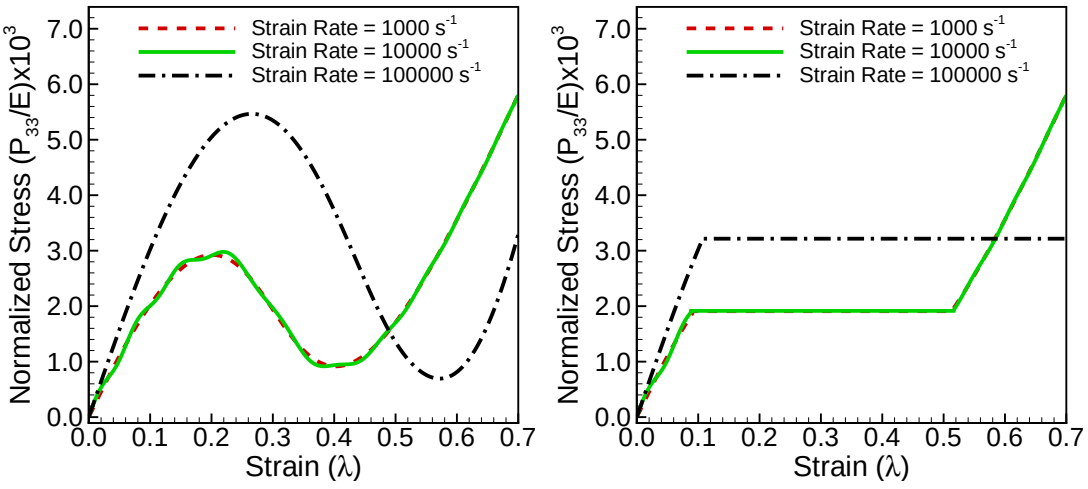

(a) Predicted effective response

(b) Effective response w/ Maxwell Stress

Figure 2.7: The effects of strain rate on foams without viscosity (purely microinertial effects). (a) Predicted effective response. (b) Effective response after evaluation of the Maxwell stress which is identified as the plateau or collapse stress. The other microstructural parameters were held constant: Young's Modulus $(E) = 1.0 \times 10^9 \frac{N}{m^2}$, Foam density $(\rho) = 100.0 \frac{Kg}{m^3}$, cell ligament viscosity $(\eta) = 0.0 \frac{N \cdot s}{m^2}$, cell ligament radius $(r) = 0.34\ mm$, cell ligament length $(L) = 1.0\ mm$.

for strain rates up to $10000 s^{-1}$ which is in agreement with our predictions.

The predictions of the present theory are in general agreement with the majority of the available experimental work, namely that as the strain rate increases, the plateau stress increases and that the extent of the plateau region increases slightly with higher strain rates. These predictions imply that the energy absorption capacity of viscoelastic foams increases for impact loading at high strain rates. The strain rate effects shown in Figure 2.6 are the combined effect of viscosity and density (inertia) during dynamic loading of the foam material. The effect of the strain rate on the overall response during foam collapse (plateau region) can be understood within the present framework as the coupled effect of the ligament viscosity and the inertial effects due to non-affine motion within the cells of the foam material. While in actual materials both effects are coupled, we can afford to investigate numerically and theoretically the effect of each individual contribution separately.

Figure 2.7 shows the effects of strain rate due to microinertia alone, which was done by simply setting the viscosity of the solid ligament material to zero during each run. According to Figure 2.7b, the microinertial strain rate effects on the plateau stress

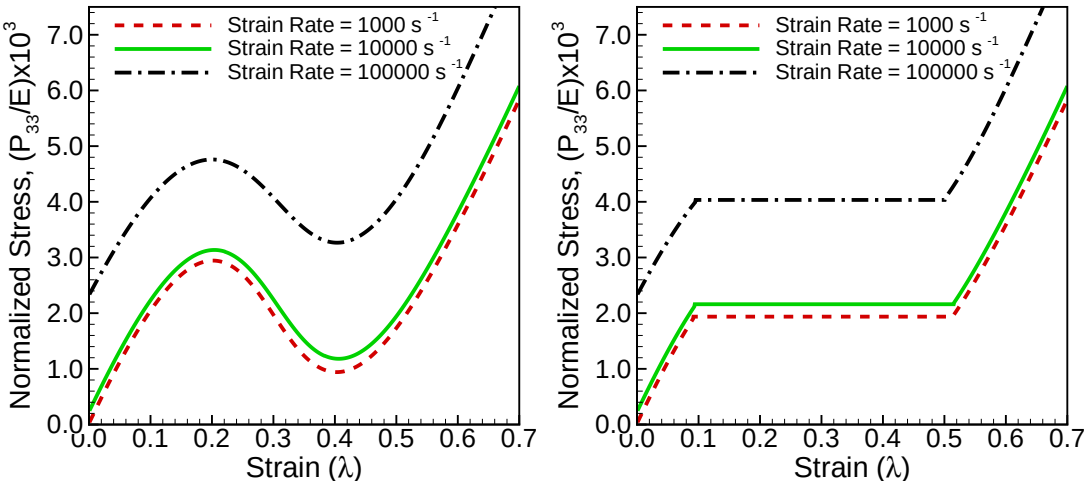

(a) Predicted effective response

(b) Effective response w/ Maxwell Stress

Figure 2.8: The effects of strain rate on viscous but massless foams (e.x. zero microinertial effect). (a) Local predicted effective response. (b) Effective response after evaluation of the Maxwell stress (the plateau or collapse stress). The other microstructural parameters were held constant: Young's Modulus $(E) = 1.0 \times 10^9 \frac{N}{m^2}$, Foam density $(\rho) = 0.0 \frac{Kg}{m^3}$, cell ligament viscosity $(\eta) = 1000.0 \frac{N \cdot s}{m^2}$, cell ligament radius $(r) = 0.34\ mm$, cell ligament length $(L) = 1.0\ mm$.

are very minimal for lower strain rates ($\dot{\varepsilon} < 10000\ s^{-1}$) but very strong at exceptionally high strain rates. Figure 2.7b also shows that the microinertial strain rate effects cause the length of the plateau region to increase as the strain rate increases. Additionally, microinertia seems to only affect the initial slope of the response at extremely high strain rates ($\dot{\varepsilon} > 50000\ s^{-1}$).

In order to look at the viscous strain rate effects alone, every run in Figure 2.8 was done with the foam density set to zero to exclude the microinertial strain rate effects. Therefore, Figure 2.8 shows the isolated strain rate effects due to the viscosity of the solid phase of the foam material. As shown in Figure 2.8b, the viscous strain rate effects on the plateau stress are clearly noticeable for lower strain rates ($\dot{\varepsilon} < 10000\ s^{-1}$). Therefore, we conclude that at lower strain rates the viscosity dominates the effect on the plateau stress during dynamic loading. Similar to the microinertia, at exceptionally high strain rates ($\dot{\varepsilon} > 50000\ s^{-1}$) the viscosity has a very strong effect on the plateau stress. Figure 2.8b also shows that the viscous strain rate effects don't affect the length of the plateau region which tells us that only the microinertia is responsible for the length of the plateau. Finally, based on Figure 2.8b, viscosity appears to cause a

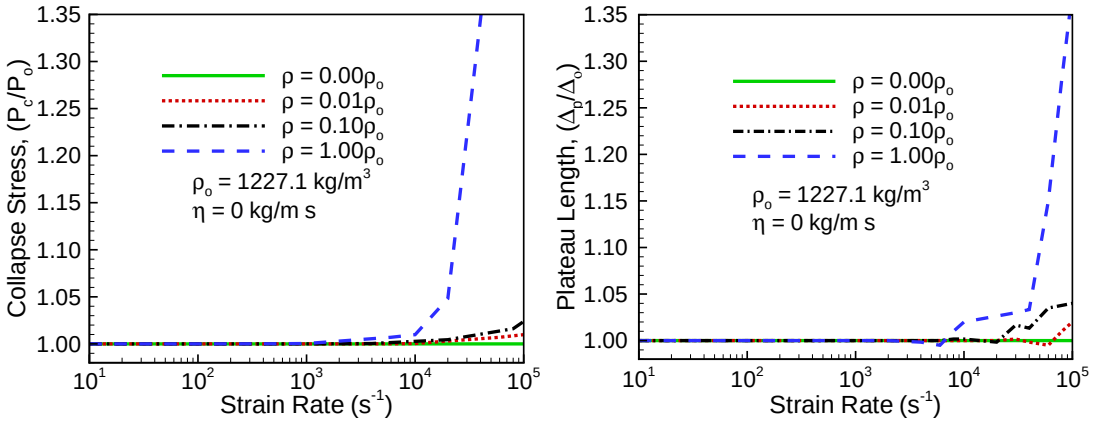

(a) Collapse Stress (b) Plateau Extent

Figure 2.9: Effect of the strain rate for non-viscous foam materials. The foam density ρ was varied as shown in the graphs but all other variables were held constant: Foam Young's modulus (E) = $1.0 \times 10^9 \frac{N}{m^2}$, Cell ligament viscosity (η) = 0 $\frac{N \cdot s}{m^2}$, Cell ligament radius (r) = 0.3 mm, Cell ligament length (L) = 1.0 mm. P_o and Δ_o were evaluated with foam density $\rho = 0$ and ligament viscosity $\eta = 0$. (a) Collapse stress P_c normalized by the static collapse stress P_o. (b) Plateau strain range Δ_p normalized by the static plateau strain range Δ_o.

gradual steady increase in the initial slope of the response as the strain rate increases.

Next we look at how the dynamic collapse of the visco-elastic foam materials compares to the quasi-static collapse behavior. We look at the effects of viscous and dynamic effects separately. First, we study the case where the ligament material has no viscosity ($\eta = 0$), and thus the strain-rate effects are solely due to the microinertial aspects. Figure 2.9a shows the predicted increase in the collapse stress and Figure 2.9b shows the predicted increase in the plateau extent as a function of the strain rate for different foam densities ρ. The foam density spans two orders of magnitude from $0.01\rho_o$ (an order of magnitude which is seen in very light woods), to $0.1\rho_o$ (for polymers) to ρ_o (for some metals), where $\rho_o = 1227.1 \frac{Kg}{m^3}$ [1]. Figure 2.9 shows that when a foam is loaded at high strain rates, the effects of microinertia are more pronounced for higher density foams such as foams with higher ligament density ρ_s. Figure 2.9a shows that the higher the foam density, the higher the increase in the plateau stress, and Figure 2.9b shows that the higher the foam density, the higher the increase in the plateau length for

[1]Note: The relative density ρ_r for all cases in Figure 2.9 is kept constant at $\rho_r = 0.0815$, therefore, as the foam density ρ is altered, the ligament density ρ_s changes.

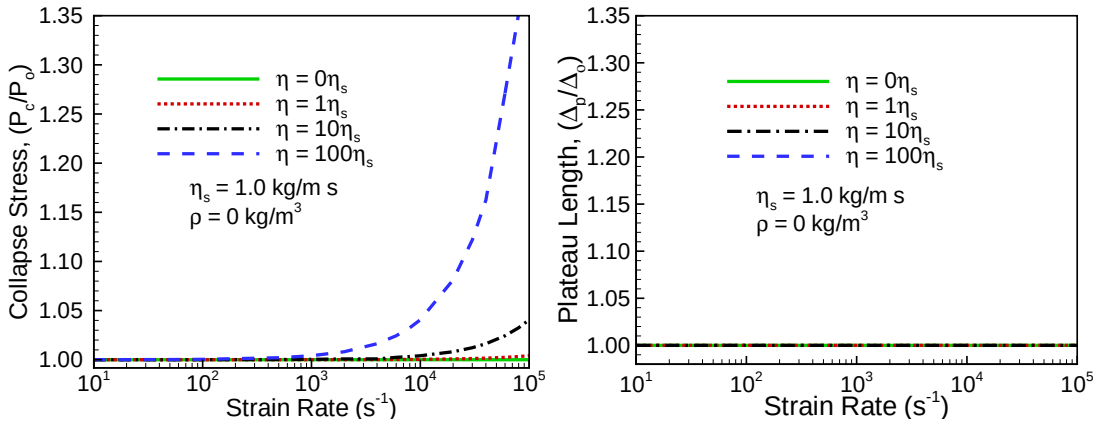

(a) Collapse Stress (b) Plateau Extent

Figure 2.10: Effect of the strain rate for viscous but massless foam materials. The solid ligament viscosity η was varied as shown in the graphs but all other variables were held constant: Foam Young's modulus $(E) = 1.0 \times 10^9 \frac{N}{m^2}$, Foam density $(\rho) = 0 \frac{Kg}{m^3}$, Cell ligament radius $(r) = 0.3\ mm$, Cell ligament length $(L) = 1.0\ mm$. P_o and Δ_o were evaluated with foam density $\rho = 0$ and ligament viscosity $\eta = 0$. (a) Collapse stress P_c normalized by the static collapse stress P_o. (b) Plateau extent Δ_p normalized by the static plateau range Δ_o.

loading at increasingly higher strain rates. The behavior is very nonlinear with respect to the applied macroscopic strain rat. As in the majority of experimental works, there is no noticeable effects for low strain rates ($\dot{\varepsilon} < 1000\ s^{-1}$), a weak dependency for intermediate rates ($\dot{\varepsilon} < 10000\ s^{-1}$) and a very strong effect for extremely high strain rates ($\dot{\varepsilon} > 50000\ s^{-1}$). If we look at the plateau stress in Figure 2.9a at $\dot{\varepsilon} = 100000\ s^{-1}$, the plateau stress increases by about 1%, 3% and 383% for $\rho_s/\rho_o = 0.01, 0.1$ and 1.0 respectively. Similarly in Figure 2.9b at $\dot{\varepsilon} = 100000\ s^{-1}$, the plateau length increases by about 1%, 3.5% and 35% for $\rho_s/\rho_o = 0.01, 0.1$ and 1.0 respectively.

Now, consider the case where the inertial aspects are ignored, i.e. when $\rho_s = 0$, this allows us to study the role of the strain rate due to ligament viscosity alone. Figure 2.10 shows both the collapse stress (P_c) normalized by the static collapse stress (P_o) and the plateau extent (Δ_p) normalized by the static plateau extent (Δ_o) as a function of the applied strain rate for different values of the viscosity η. The range of the viscosity spans two orders of magnitude from $\eta = 1\eta_s$ to $\eta = 10^2\eta_s$, where η_s is set to 1.0 $\frac{N \cdot s}{m^2}$. As expected higher collapse stress is observed for higher viscosity and higher applied strain rate as shown in Figure 2.10a. Notice that the effects of viscosity are

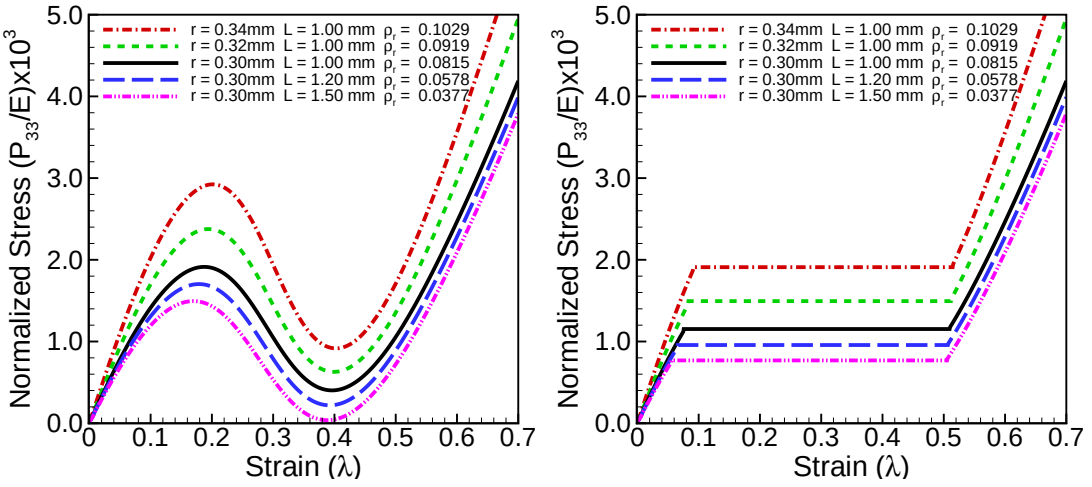

(a) Effective predicted response

(b) Effective response w/ Plateau stress

Figure 2.11: Effects of relative density ρ_r on the effective response of open-cell foams with zero viscosity. To obtain these results the relative density ρ_r was varied trough the ligament radius r and length L and the other parameters remained constant at: Ligament viscosity $(\eta) = 0.0\ \frac{N \cdot s}{m^2}$, Foam density $(\rho) = 100\ \frac{Kg}{m^3}$, Ligament Young's modulus $(E) = 1.0 \times 10^9\ \frac{N}{m^2}$. (a) Effective predicted response for varying relative density. (b) Effective response w/ the plateau stress(= Maxwell stress).

initially observed for values of strain rate above 10^3, but these effects grow very rapidly for faster rates. As the strain rate increases, the viscosity η, however, does not affect the length of the plateau region, which remains unaltered by any value considered as shown in Figure 2.10b.

Finally, to further investigate the role of microinertia, we consider the role of foam relative density in Figure 2.11. As discussed in Wang and Cuitiño (2000), for the present cellular microstructure with cylindrical ligaments, the *relative* density ($\rho_{\mathrm{r}} = \rho/\rho_{\mathrm{s}}$) is univocally determined by the cell geometry (cell ligament length L and radius r) and is written as stated in Equation 2.46. We concentrate on the effects of the cell geometry at a constant strain rate of 1000 s^{-1} where microinertial effects from modeling can be compared with most of the available experimental data.

Higher relative density foams which result from adopting shorter and/or thicker ligaments, increase the plateau stress as shown in Figure 2.11b.[2] Figure 2.11b shows that when the relative density is increased by augmenting the thickness of the ligaments

[2]Note: the foam density (ρ) for all these cases is kept constant and equal to $100\frac{Kg}{m^3}$; therefore, as the relative density (ρ_{r}) is altered, the ligament density (ρ_{s}) changes.

while holding the length constant, the plateau stress increases and similarly when the relative density is increased by reducing the ligament length while holding the thickness constant, the plateau stress increases. Experimentally, Yi et al. (2001) showed that as the relative density of the foam is decreased, the collapse stress shows a decreased sensitivity to strain rate. Lankford and Dannemann (1998) and Dannemann and Lankford (2000) reported that the strain rate dependence was negligible for low density open-celled aluminum foams, and the effect was more apparent for higher density foams. Similarly, Mukai et al. (1999a) reported that the plateau stress of a close-celled aluminum, ALPORAS, exhibited a higher strain rate sensitivity than a polystyrene foam with the same density. These experimental conclusions are in agreement with the predictions of the current model.

2.5 Conclusions

A mesoscopic model to describe spatially homogeneous open-cell visco-elastic foams subjected to *dynamic*loading has been developed where the effective macroscopic stress state is obtained by enforcing the principle of stationary action on a representative unit cell. While the present approach is independent of the particular unit cell selection, in this chapter we limit the formulation to unit cells where all ligaments converge into a central vertex. Moreover, for the presented theoretical predictions, the cell topology is further constrained to cells with only four ligaments realizing a diamond structure. In the formulation both the elastic and viscous contributions for both the bending and axial components are incorporated. The bending and axial contributions are written in additive form thanks to the introduction of the simplifying kinematic assumption that the bending deformation is concentrated near the cell vertex for low relative density foams. A distinctive feature which arises naturally from the present formulation is a microinertial term in the constitutive relation. This term appears due to the non-affine motion (acceleration) of the unit cell vertex, which is most notably observed during cell collapse at high strain rates.

A set of effective predictions are presented in order to investigate the effects of strain rate. These predictions are based only on the local formulation at unit cell

level and the Maxwell stress idea. As in the majority of experimental studies, the simulations showed that as the strain rate increases the plateau stress increases with minimal effects at lower strain rates and stronger effects at higher strain rates. The effect of the strain rate on the effective response during foam collapse (plateau region) can be understood within the present framework as the coupled effect of the ligament viscosity and the inertial effects due to foam density and non-affine motion within the cells of the foam material. While in actual materials both effects are coupled, we investigate the effect of each individual contribution separately. The predictions for non-viscous ligaments isolated the microinertial strain rate effects and exhibited an increase in plateau length for increasing strain rates and an increased collapse stress and Young's modules for strain rates above 50000 s^{-1}. The predictions for foams with massless but viscous ligaments demonstrated an increase in plateau stress and the Young's modulus for increasing strain rate but zero effect on the length of the plateau region. Based on these results, we conclude that the microinertial strain rate effects are most significant at extremely high strain rates ($\dot{\epsilon} > 50000 s^{-1}$) and that the viscosity is mostly responsible for the effects at lower strain rates ($\dot{\epsilon} < 10000 s^{-1}$). Even though the viscosity affects the response at all rates, it doesn't seem to have an effect of the length of the plateau region.

As in the majority of experimental studies, we observed very minimal strain rate effects for less than $1000 s^{-1}$ strain rates. Overall the formulation agrees well with the main conclusions of the experimental studies, namely that as the strain rate increases the plateau stress increases. These effects are more noticeable for more viscous and/or more massive foams which can happen by increasing the ligament density for a constant relative density or by increasing the relative density (by increasing the ligament thickness and/or decreasing the ligament length) for a constant ligament density. In summary the present theory allows one to define a constitutive formulation for lightweight, open-cell foams based on clear and quantifiable parameters such as microstructural topology, geometry and ligament properties. The model incorporates the competition between the bending and axial contributions which are necessary in order to capture the process of collapse. The effects of dynamic loading are considered

through the incorporation of viscosity at ligament level and microinertia at unit cell level. The theory can be incorporated into the general framework of nonlinear finite element analysis codes as a constitutive update in the context of either quasi-static or dynamic problems using either explicit or implicit formulations as will be shown in chapter 4. The details of the numerical formulation and implementation including the derivation and performance evaluation of the consistent tangents are the scope of chapter 4.

Chapter 3

Micromechanical Modeling of Dynamically Loaded Open-Cell Metallic Foams: Yielding, Collapse and Strain Rate Effects

Open-celled metallic foams exhibit properties desirable in engineering applications requiring mitigation of the adverse effects resulting from impact loading however the history dependent, dynamic response of these cellular materials has not been clearly elucidated. This chapter contributes an approach for modeling the response of dynamically loaded open-cell metallic foams from ligament level to unit cell level to specimen level. The effective response captures the localized chaotic collapse phenomena through ligament reorientation at cell level while maintaining the history of plastic deformation at ligament level. First, the phenomenological elasto-plastic constitutive behavior of the ligaments composing the unit cell is modeled. Then, using the constitutive ligament model, the effective unit cell response is obtained from a micromechanical model which enforces the principle of minimum action on a representative $3D$ unit cell. The current communication focuses on the ability of the model to capture the yielding and collapse behavior as well as the strain rate effects observed in recent tests on metallic foams.

3.1 Introduction

Man-made cellular materials such as polymeric, metallic, ceramic, and glassy foams and natural cellular materials such as wood, bone, coral, and sponge engage our interest because they are hybrid in structure and behavior exhibiting properties and characteristics of multiple states of matter Weaire and Hutzler (1999). The variety in cellular structure combined with the diversity of materials which can form the solid phase results in foam materials with a vast array of combinations of properties capable

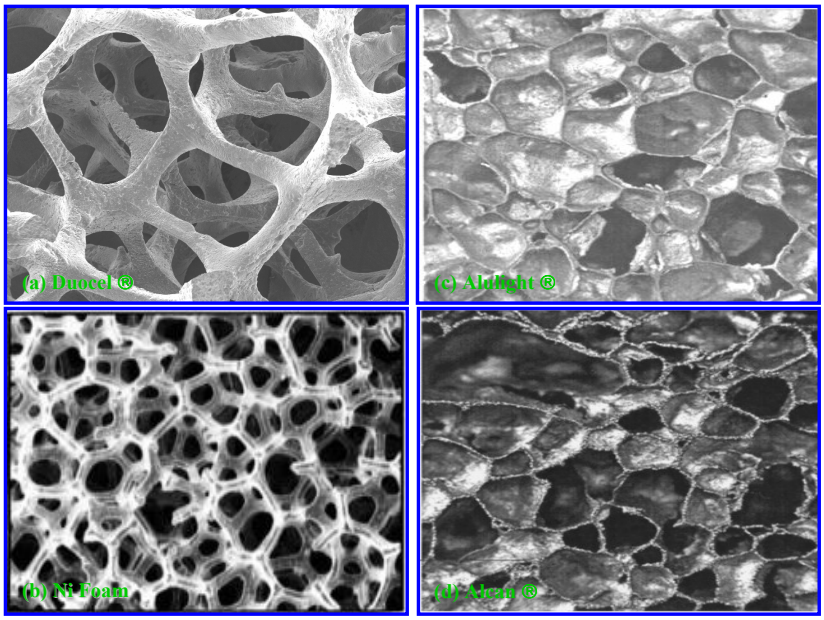

Figure 3.1: Cellular Structure of Metallic Open-Cell Foams.

of performing multiple functions. Here we focus on metallic foams, an emerging class of man-made cellular material with intriguing properties which could be exploited in different potential applications.

Metallic foams can have open-cell or closed-cell or mixed cellular structures depending on the synthesis process. These materials are essentially synthesized by generating bubbles in a molten metal and solidifying at a specific rate to produce the desired cellular structure and material properties such as high strength to weight ratio, high deformability, and high surface area. The different processing routes including gas injection into a melt, immersion of gas releasing blowing agents into a melt, and pouring the molten metal into a removable mold have been reviewed by authors such as Banhart (2003); Gibson (2000); Ashby et al. (2000); Gibson and Ashby (1997). Open-cell foams are permeable and resemble a labyrinth of interconnected struts while closed-cell foams are impermeable and can be though of as a lattice arrangement of hollow spherical bubbles. The work presented here concentrates on open-cell metallic foams which we model as a network of interconnected struts surrounded by air-filled voids. Figure 3.1 shows a typical open-cell metallic foam.

Many industries such as automotive, aircraft, maritime, and rail transportation, as well as the electronic and packaging industries require strong and/or lightweight materials such as metallic foams. These materials are being considered for applications such as lightweight construction (sandwich panel cores), impact energy mitigation, thermal management (heat dissipators), acoustic and vibration insulation (dampers). Recently there has been an elevated interest in utilizing metallic foams in applications requiring mitigation of impact energy during exposure to dynamic loading at high strain rates especially in areas requiring high collapse strengths not currently accessible with polymeric, ceramic and glass foams. Because of their varied combinations of properties, metallic foams can be best implemented as multi-functional materials in applications requiring a set of properties not available from their bulk solid counterparts.

The mechanical response of cellular materials such as metallic open-cell foams is dominated by the cellular structure and the properties of the solid phase such as the constitutive behavior of the ligaments in open-cell foams. The response is characterized by an initial elastic region (usually linear) followed by a long plateau region due to unstable collapse of cells and concluded by a densification region after termination of cell collapse. The majority of the early pioneering studies on the mechanics, characterization and properties of metallic foams has been well documented in reviews such as Gibson (2000); Ashby et al. (2000); Gibson and Ashby (1997); Evans et al. (1999). More recently, experimental and modeling studies have concentrated on the different stages of deformation as well as on the effects of the cell wall properties on the macroscopic response of open-cell foams, for instance Bardenhagen et al. (2005); Gong et al. (2005); Zhou et al. (2004a). Due to the recent interest in utilizing metallic foams for energy absorption applications, there has been a number of experimental studies focusing on the dynamic response of metallic foam materials for example Mukai et al. (1999a,b); Shimojima et al. (2001); Dannemann and Lankford (2000); Kanahashi et al. (2001); Han et al. (1998); Hall et al. (2000) The majority of these studies concluded that the collapse strength of the foam increases with increasing strain rate, density and/or viscosity.

Most of the studies on foams under dynamic loading focus on the effects of

strain on the overall response. For example, the effect of strain rate on the dynamic compression of aluminum alloys foams was reported by Yi et al. (2001) where the effects of strain rate up to $3000s^{-1}$ along with relative density were presented showing that the collapse stress of aluminum foams increases with increasing strain rate, but this effect becomes less pronounced as the relative density of the foam decreases. Kanahashi et al. (2000) concluded that plateau stress normalized by the relative density and the absorbed energy drastically increased based on dynamic compression experiments ($\dot{\epsilon} = 1.4x \times 10^3 s^{-1}$) of very low density aluminum foams. Higher strain rate (up to 5000 s^{-1}) compression experiments were done by Deshpande and Fleck (2000a); however, they concluded that strain rate had no effect on the plateau stress. Studies for open-cell metallic foams and pyramidal truss cores with strain rates up to $10000s^{-1}$ using a Kolsky bar and a Gas Gun were recently reported by Lee et al. (2006b,a) where it was shown that strain rate has very minimal effects on the collapse stress for strain rates up to $10000s^{-1}$.

The theoretical and numerical response remains to fully assessed due to the challenges posed by the history dependent plastic yielding that occurs during large deformation of metallic foams. Some of the available modeling efforts include the FEM comprehensive study on the effects of various geometrical imperfections on the in-plane yielding behavior of $2D$ cellular foams under biaxial loading Chen et al. (1999). Meguid et al. (2002) used a modified cube as the representative unit cell to model the quasi-static crushing of closed-cell metallic foams. A rate-dependent elasto-plastic foam constitutive model was developed in Zhang et al. (1998) to use with $LS - DYNA3D$ software. A version of the material point method (MPM), the Generalized Interpolation Material Point method (GIMP method), was recently used to analyze a small group of open cells with emphasis on the densification portion of the deformation Bardenhagen et al. (2005). Finally, Demiray et al. (2007) reported an approach for the numerical determination of the evolution of the initial and subsequent yield surfaces of metallic open-cell foams. Our has reported a micromechanical model to predict the effective response of open-cell foams; initially the model was developed for quasi-statically loaded, hyper-elastic open-cell foams as communicated in Wang and Cuitiño (2000) and recently it was further

developed to predict the response of dynamically loaded, visco-elastic open-cell foams as presented in chapter 2. Here we present the extension of that model to dynamically loaded open-cell elasto-plastic metallic foams.

As stated earlier, there is a need for additional modeling work based on consistent strut and unit cell level mechanics capable of predicting the full field response of metallic foam materials in dynamic loading environments. Any model for metallic foams should accurately capture the history dependent constitutive response of the solid phase (struts) as well as the unit cell buckling process. Here, we present the application to metallic foams of the micromechanical formulation for dynamically loaded open-cell foams developed in chapter 2. The current approach starts by modeling the experimentally observed elasto-plastic constitutive behavior (including hardening) of the metallic struts composing the open-cell structure and then incorporating this behavior into the micromechanical model which captures the unit cell collapse and predicts the effective foam response. The history dependent, elasto-plastic constitutive model of the solid struts and the unit cell formulation can then be implemented as a constitutive update into a nonlinear Finite Elements Analysis (FEA) scheme to predict the response of the macroscopic metallic open-cell foam specimen as will be shown in Chapter 4.

The rest of this chapter is organized as follows. Section 3.2 presents an overview of the formulation and the modeling approach. Section 3.2.1 briefly reviews the unit cell micromechanical model formulated in Chapter 2. Section 3.2.2 presents the axial and bending elasto-plastic, history dependent constitutive behavior of the struts composing the unit cell along with the predicted constitutive response for the struts. The effects of the history of plastic deformation and effects of loading rate are presented in Section 3.3 through the effective metallic foam response predicted by the unit cell micromechanical model while instituting elasto-plastic constitutive behavior at cell wall level. Finally section 4.6 will pose some concluding remarks.

3.2 Formulation

A formulation to predict the effective dynamic response of open-cell foams based on a micromechanical unit cell model was presented in chapter 2. The formulation can be

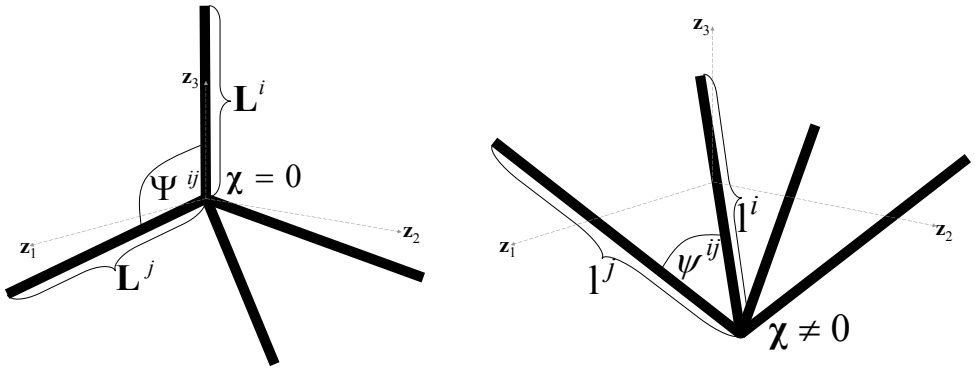

(a) Undeformed Unit Cell (b) Deformed Unit Cell

Figure 3.2: Depiction of the local kinematic evolution of the length of each half ligament $\mathbf{l}^i$ and the angle between any two ligaments ψ^{ij}. The axial strain for any ligament i is defined as $\epsilon^i = log(\lambda^i) = log(\frac{l^i}{L^i})$ and the change in angle between any two ligaments i and j is defined as $\alpha^{ij} = \psi^{ij} - \Psi^{ij}$.

implemented as a constitutive update in the realm of nonlinear finite element analysis for scenarios where the specimen size is much larger than the size of the cells composing the foam material as will be done in chapter 4. The description is limited to open-cell foams with cells containing M struts converging at a central vertex. The deformation of a 4 strut unit cell ($M = 4$) is described in Fig. 3.2. This type of unit cell can generate a coherent cellular solid by recursive application of point symmetry operations centered on each of the ligament midpoints. As shown in Fig. 3.2, the cell deforms according to the macroscopically prescribed affine deformation $\mathbf{F}$, however the formulation allows the cell vertex to move an additional amount $\boldsymbol{\chi}$ which results in non-affine motion/deformaton within the cell. Here we present the application of that formulation to open-cell metallic foams with elasto-plastic constitutive cell wall (strut) behavior.

3.2.1 Micromechanical Model

This section briefly reviews the micromechanical unit cell model reported in chapter 2 where the response of dynamically loaded open-cell foams is predicted for all stages of foam deformation (initial elastic, plateau, and densification). The model predicts the collapse behavior in open-cell foams by capturing the unstable behavior of the unit cells through the non-affine motion $\boldsymbol{\chi}$ of the cell vertex. The non-affine degree of freedom

$\boldsymbol{\chi}$ allows one to capture the bending and axial deformation with the assumption that bending is concentrated at the vertex for unit cells composed of thin struts.

Consider a 3D unit cell composed of M struts where the initial length vector L^i_α for every strut i and the initial angle Ψ^{ij} between every two struts $i \neq j$ in the unit cell are specified. Then for an applied deformation F_{kK}, the new length vector l^i_α for every struts and the new angle ψ^{ij} between every two struts on the deformed unit cell as shown in Fig. 3.2 are given by Eqn. (4.46).

$$l^i_\alpha = F_{kK} L^i_\alpha - \chi_\alpha \qquad \psi^{ij} = \cos^{-1}\left(\frac{l^i_\alpha \; l^j_\alpha}{l^i \; l^j}\right) \qquad \alpha = 1...3 \tag{3.1}$$

The χ_α needed in Eqn. (4.46) is determined for the prescribed deformation F_{kK} by enforcing on the representative 3D unit cell the principle of minimum action for dissipative systems as described by Eqn. (3.2).

$$\frac{d}{dt}\left(\frac{\partial \Pi}{\partial \dot{\chi}_\alpha}\right) - \frac{\partial \Pi}{\partial \chi_\alpha} = Q_\alpha \tag{3.2}$$

Here $\Pi(= \mathcal{T} - \mathcal{P})$ represents the Lagrangian expressed as the difference between the kinetic energy ($\mathcal{T}$) and the potential energy ($\mathcal{P}$) of the system. $Q_\alpha(= \frac{\partial \mathcal{D}}{\partial \dot{\chi}_\alpha})$ represents the nonconservative forces arising from the dissipative energy ($\mathcal{D}$) of the system. The resulting equation of motion shown in Eqn. (4.47) determines the kinematic equilibrium condition for each cell through χ_α.

$$R_\alpha(F_{kK}, \chi_\alpha) = \sum_{i=1,M} f^i_\alpha - m_c \ddot{\chi}_\alpha = 0 \tag{3.3}$$

R_α represents the equilibrium resultant for the involved forces, $m_c \ddot{\chi}_\alpha$ represents the microinertial forces where m_c is an effective mass located at the cell vertex and $\ddot{\chi}_\alpha$ is the acceleration of the cell vertex. f^i_α represents the force due to ligament i and it is evaluated as the sum of the axial $\mathcal{N}_i$ and shear $\mathcal{V}_i$ forces at the cell vertex from ligaments $i - M$ as shown below.

$$f^i_\alpha \;\; = \;\; \mathcal{N}_i e^{l^i}_\alpha + \mathcal{V}_i e^{\bar{l}^i}_\alpha = \mathcal{N}_i e^{l^i}_\alpha + \frac{1}{l^i} \sum_{j=1,M} \mathcal{M}_{ij} e^{l^i l^j}_\alpha \tag{3.4}$$

Here e^{l^i} and $e^{l^i l^j}$ represent local unit base vectors defining the direction along strut i and the direction perpendicular to struts i and j respectively. Notice that the shear force

$\mathcal{V}_i$ due to each ligament i is evaluated from the bending moment $\mathcal{M}_{ij}$ between strut i and all j struts for $i \neq j$. The unit cell configuration χ_α is determined numerically by iterating using the Taylor expansion of Eqn. (4.47) and a Newton-Raphson scheme.

Once the kinematic configuration of the cell χ_α is determined through Eqn. (4.47) for a particular value of applied deformation F_{kK}, the stress state P_{kK} is obtained by differentiation of the elastic $\mathcal{W}$ and viscous $\mathcal{D}$ energy of the system with respect to the deformation F_{kK} and the rate of deformation $\dot{F}_{kK}$. The resulting final expression is stated below.

$$P_{kK}(F_{kK}) = \frac{1}{\mathcal{B}_o}\left[\sum_{i=1,M} f_k^i L_K^i - m_c \frac{\partial \chi_\alpha}{\partial F_{kK}} \ddot{\chi}_\alpha\right] \tag{3.5}$$

Notice that the constitutive relation in Eqn 3.5 includes the microinertial stresses $m_c \frac{\partial \chi_\alpha}{\partial F_{kK}} \ddot{\chi_\alpha}$ as well as the stresses due to stretching and bending $f_k^i L_K^i$ of the struts. Keep in mind that f_k^i involves both the axial and shear forces as stated in Eqn. (3.4).

3.2.2 Cell Wall Constitutive Behavior

In order to apply the micromechanical model reviewed in Section 3.2.1 it is necessary to obtain the axial and bending constitutive behavior of the solid struts composing the unit cells, namely $\mathcal{N}_i$ and $\mathcal{M}_{ij}$ for any struts i and j on a unit cell. The strut axial force $\mathcal{N}_i$ and the bending moment $\mathcal{M}_{ij}$ are respectively determined as a function of the elastic axial strain ϵ_{n+1}^e and the elastic change in angle α_{n+1}^e between every two ligaments. At unit cell and strut level the axial strain and change in angle between any two struts are measured as explained in Fig. 3.2. Sections 3.2.2 describes the axial deformation and the expressions at strut level which allow us to model the axial elasto-plastic constitutive behavior of struts. Similarly Section 3.2.2 describes bending deformation and the expressions used to predict the bending elasto-plastic constitutive behavior at strut level. The variables in the expressions will be presented in discrete form to give the reader a sense of the numerical process. Due to the foaming process, the constitutive behavior of struts in open-cell foams can be very different when compared the their solid counterparts. Recent experiments by Zhou et al. (2004a) captured the axial constitutive behavior of the struts in metallic open-cell foams for different heat

treatments. The formulation presented next allows one to model any elasto-plastic constitutive behavior at strut level.

Strut Axial Response

For a particular *metallic strut* on a unit cell of an open-cell foam consider the discrete multiplicative decomposition of the total axial deformation (λ_{n+1}) into the elastic (λ^e_{n+1}) and plastic (λ^p_{n+1}) axial deformation.

$$\lambda_{n+1} = \lambda^e_{n+1}\lambda^p_{n+1} \quad \Rightarrow \quad \lambda_{n+1} = \frac{l_{n+1}}{L} \qquad \lambda^p_{n+1} = \frac{l^p_{n+1}}{L} \tag{3.6}$$

Here L refers to initial strut length and l_{n+1} refers to the current strut length. Further decomposition of the current plastic deformation (λ^p_{n+1}) into the previous plastic deformation (λ^p_n) and the incremental step in plastic deformation, $\Delta\lambda^p$, gives.

$$\lambda^p_{n+1} = \lambda^p_n \Delta\lambda^p \quad \Rightarrow \quad \lambda^p_n = \frac{l^p_n}{L} \qquad \Delta\lambda^p = \frac{l^p_{n+1}}{l^p_n} \tag{3.7}$$

where l^p_n and l^p_{n+1} refers to the previous and current plastic strut length respectively. The strain ϵ_{n+1} is defined through the logarithmic definition based on the expressions in Equations 3.6 and 3.7.

$$\begin{aligned}
\epsilon_{n+1} &= \log(\lambda_{n+1}) = \log(\lambda^e_{n+1}\lambda^p_{n+1}) = \log(\lambda^e_{n+1}) + \log(\lambda^p_{n+1}) \\
&\Rightarrow \quad \epsilon_{n+1} = \epsilon^e_{n+1} + \epsilon^p_{n+1} \qquad (3.8) \\
\epsilon^p_{n+1} &= \log(\lambda^p_{n+1}) = \log(\lambda^p_n \Delta\lambda^p) = \log(\lambda^p_n) + \log(\Delta\lambda^p) \\
&\Rightarrow \quad \epsilon^p_{n+1} = \epsilon^p_n + \Delta\epsilon^p \qquad (3.9) \\
\epsilon_{n+1} &= \epsilon^e_{n+1} + \epsilon^p_{n+1} = \epsilon^e_{n+1} + \epsilon^p_n + \Delta\epsilon^p \\
&\Rightarrow \quad \epsilon^e_{n+1} = \epsilon_{n+1} - (\epsilon^p_n + \Delta\epsilon^p) \qquad (3.10)
\end{aligned}$$

where ϵ_{n+1} represents the total current axial strain, ϵ^e_{n+1} represents the current axial elastic strain, ϵ^p_{n+1} represents the current axial plastic strain, ϵ^p_n refers to the previous axial plastic strain and $\Delta\epsilon^p$ refers to the increment in plastic strain.

Now we are ready to write down the expressions as functions of the strain variables in Equations 3.8 - 3.10 which will dictate the axial constitutive response of

the struts in the cells. The axial response is a function of the elastic ligament axial strain ϵ^e_{n+1}. Here the strut's axial force $\mathcal{N}(=\sigma A)$ is predicted from the linear relation

$$\begin{aligned}\mathcal{N}_{n+1}(\epsilon_{n+1},\Delta\epsilon^p) &= EA\epsilon^e_{n+1} = EA(\epsilon_{n+1}-\epsilon^p_{n+1}) \\ &= EA(\epsilon_{n+1}-(\epsilon^p_n+\Delta\epsilon^p)) \end{aligned} \tag{3.11}$$

where E represents the strut's Youngs Modulus and A represents the strut cross sectional area. The evolution of the Yield Force $\mathcal{N}_y(=\sigma_y A)$ is predicted by a hardening power law

$$\begin{aligned}\mathcal{N}_{y,n+1}(\Delta\epsilon^p) &= A\sigma_{oy}\left(\frac{|\epsilon^p_{n+1}|}{\epsilon^p_o}+1\right)^{1/r} \\ &= A\sigma_{oy}\left(\frac{|\epsilon^p_n|+|\Delta\epsilon^p|}{\epsilon^p_o}+1\right)^{1/r} \end{aligned} \tag{3.12}$$

where r is a hardening exponent, σ_{oy} is the initial yield stress and ϵ^p_o is a reference plastic strain. Finally, the increment in plastic deformation is dictated by a rate of plastic axial deformation power law

$$\dot{\epsilon^p} = \dot{\epsilon}^p_o\left(\frac{|\mathcal{N}_{n+1}|}{\mathcal{N}_{y,n+1}}-1\right)^{1/m} \tag{3.13}$$

where $\dot{\epsilon}^p_o$ is a reference plastic strain rate and m is a rate-sensitivity exponent. Now, denoting the time step by Δt and substituting $\Delta\epsilon^p = \Delta t\dot{\epsilon^p}$ into Eqn. (3.13) and rearranging we can write

$$G1(\epsilon_{n+1},\Delta\epsilon^p) = \Delta\epsilon^p - \Delta t\dot{\epsilon}^p_o\left(\frac{|\mathcal{N}_{n+1}|}{\mathcal{N}_{y,n+1}}-1\right)^{1/m} = 0 \tag{3.14}$$

For any specified deformation ϵ_{n+1} through l_{n+1} which is specified by F_{kK} and χ_α, $\Delta\epsilon^p$ is determined from Eqn. (3.14) by iterating on its Taylor expansion using a Newton Raphson procedure.

$$\Delta\epsilon^p_{n+1} = \Delta\epsilon^p_n - \frac{\partial G1}{\partial\Delta\epsilon^p} \tag{3.15}$$

The strut axial constitutive behavior predicted by Eqn. (3.11), Eqn. (3.12) and Eqn. (3.13) is shown in Fig. 3.3. Fig. 3.3a presents the axial constitutive response for tensile loading alone while Fig. 3.3b presents the loading and unloading response for both tensile and compressive loading. Fig. 3.3b clearly demonstrates that the model is able to capture the effects of the history of plastic deformation during loading, unloading and/or reverse loading.

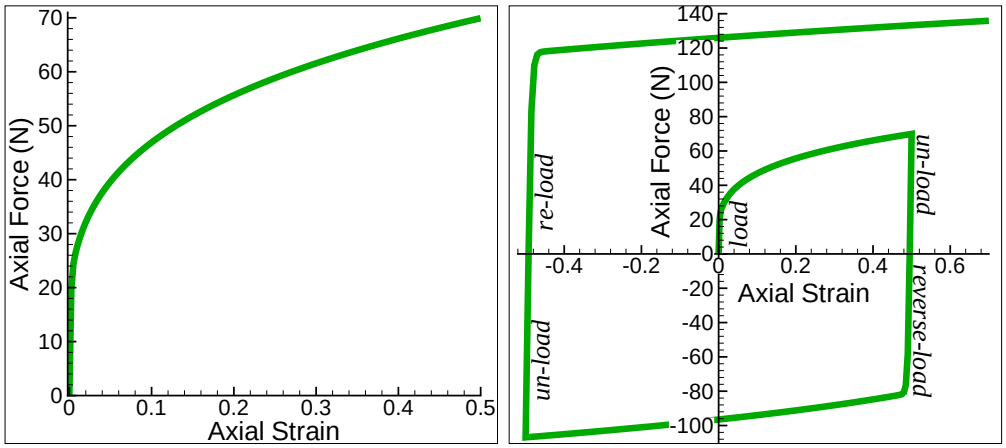

(a) Axial Force (b) Axial Force w/ Unloading

Figure 3.3: The axial constitutive behavior of the struts composing each unit cell of an open-cell metallic foam as predicted by Eqn. (3.11), Eqn. (3.12), and Eqn. (3.13). The variables in Eqn. (3.11), Eqn. (3.12), and Eqn. (3.13) were taken as *initial initial length* $L_o = 1.0mm$, *initial strut radius* $r_o = 0.3mm$, $E = 50.0Gpa$, $\sigma_{yo} = 50.0Mpa$, *exponent* $r = 4$, *axial exponet* $m = 4$, $\epsilon_p^o = 0.005$, $\dot{\epsilon}_p^o = 0.10$ (a)The loading axial constitutive response for tensile loading. (b)The axial constitutive response for loading and unloading for both tensile and compressive loading.

Strut Bending Response

Now consider two particular *metallic struts* on the unit cell of an open-cell foam. Initially the angle between the two struts is Ψ and after deformation of the unit cell the current angle between the two struts is ψ_{n+1}. Lets define the current change in angle by α_{n+1} and then lets split it into a elastic change in angle α^e_{n+1} and a plastic change in angle α^p_{n+1}.

$$\alpha_{n+1} = \alpha^e_{n+1} + \alpha^p_{n+1} \tag{3.16}$$

$$\alpha_{n+1} = \psi_{n+1} - \Psi \qquad \alpha^p_{n+1} = \psi^p_{n+1} - \Psi \tag{3.17}$$

ψ^p_{n+1} in Eqn. (3.17) refers to the remaining plastic angle between the ligaments after unloading. The current plastic change in angle α^p_{n+1} is further subdivided into the previous plastic change in angle α^p_n and the increment of plastic change in angle $\Delta\alpha^p$.

$$\alpha^p_{n+1} = \alpha^p_n + \Delta\alpha^p \quad \Rightarrow \quad \alpha^p_n = \psi^p_n - \Psi \tag{3.18}$$

ψ^p_{n+1} and ψ^p_n in Eqn. (3.17) and Eqn. (3.18) refer respectively to the current and previous parts of the plastic angle between two ligaments. From Eqn. (3.16) and Eqn. (3.18) we

can write the current elastic change in angle α^e_{n+1} as

$$\begin{aligned} \alpha_{n+1} &= \alpha^e_{n+1} + \alpha^p_{n+1} = \alpha^e_{n+1} + \alpha^p_n + \Delta\alpha^p \qquad (3.19) \\ \Rightarrow \quad \alpha^e_{n+1} &= \alpha_{n+1} - (\alpha^p_n + \Delta\alpha^p) \qquad (3.20) \end{aligned}$$

Next, Using the variables in Eqns. (3.16-3.19), we present the set expressions which will model the bending constitutive response between any two struts on a unit cell of a metallic open-cell foam. The bending response is a function of the elastic change in angle α^e_{n+1} between any two ligaments. Here the bending moment $\mathcal{M}_{n+1}$ between any two struts is given by the linear relation

$$\begin{aligned} \mathcal{M}_{n+1}(\alpha_{n+1}, \Delta\alpha^p) &= \frac{3EI}{L}\alpha^e_{n+1} = \frac{3EI}{L}(\alpha_{n+1} - \alpha^p_{n+1}) \\ &= \frac{3EI}{L}(\alpha_{n+1} - (\alpha^p_n + \Delta\alpha^p)) \qquad (3.21) \end{aligned}$$

where E refers to the Youngs Modulus of the struts, I refers to moment of inertia of the struts, and L refers to the initial ligament length. The evolution of the yielding bending moment $\mathcal{M}_{y,n+1}$ is predicted by a hardening power law

$$\begin{aligned} \mathcal{M}_{y,n+1}(\Delta\alpha^p) &= \frac{I\sigma_{oy}}{r}\left(\frac{|\alpha^p_{n+1}|}{\alpha^p_o} + 1\right)^{1/r} \\ &= \frac{I\sigma_{oy}}{r}\left(\frac{|\alpha^p_n| + |\Delta\alpha^p|}{\alpha^p_o} + 1\right)^{1/r} \qquad (3.22) \end{aligned}$$

where σ_{oy} is the initial yield stress, α^p_o is a reference plastic change in angle and r is a hardening exponent. Lastly, the increment in plastic change in angle is dictated by a rate of plastic deformation power law

$$\dot{\alpha^p} = \dot{\alpha}^p_o\left(\frac{|\mathcal{M}_{n+1}|}{\mathcal{M}_{y,n+1}} - 1\right)^{1/m} \qquad (3.23)$$

where $\dot{\alpha}^p_o$ is a reference rate for the plastic in change and m a rate sensitivity exponent. Substituting $\Delta\alpha^p = \Delta t\dot{\alpha}^p$ into Eqn.(3.23) above and rearranging we can write

$$G2(\alpha_{n+1}, \Delta\alpha^p) = \Delta\alpha^p - \Delta t\dot{\alpha}^p_o\left(\frac{|\mathcal{M}_{n+1}|}{\mathcal{M}_{y,n+1}} - 1\right)^{1/m} = 0 \qquad (3.24)$$

For any specified α_{n+1} through ψ_{n+1} which is specified through F_{kK} and χ_α, $\Delta\alpha^p$ is determined from Eqn.(3.24) by iterating on its Taylor expansion using a Newton Raphson procedure.

$$\Delta\alpha^p_{n+1} = \Delta\alpha^p_n - \frac{\partial G2}{\partial\Delta\alpha^p} \qquad (3.25)$$

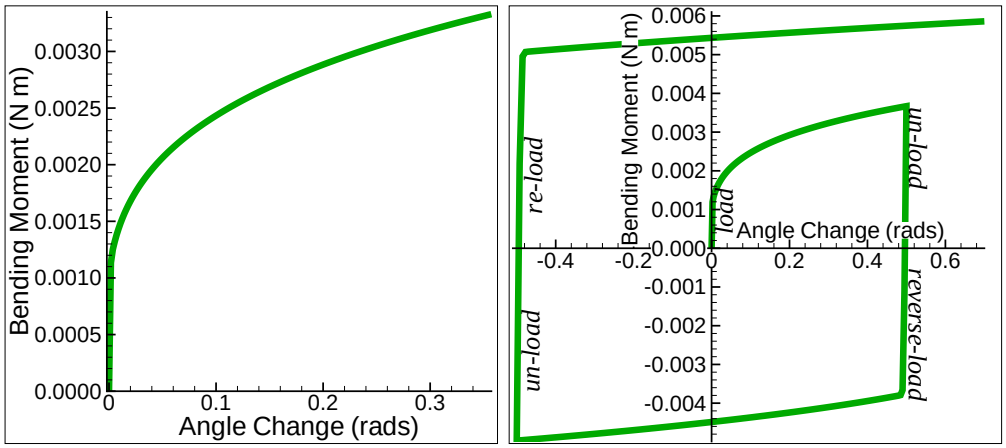

(a) Bending Moment (b) Bending Moment w/ Unloading

Figure 3.4: The bending constitutive behavior of the struts composing each unit cell of an open-cell metallic foam as predicted by Eqn. (3.21), Eqn. (3.22), and Eqn. (3.23). The variables in Eqn. (3.21), Eqn. (3.22), and Eqn. (3.23) were taken as *initial length* $L_o = 1.0mm$, *initial strut radius* $r_o = 0.3mm$, $E = 50.0Gpa$, $\sigma_{yo} = 50.0Mpa$, *exponet* $r = 4$, *exponent* $m = 20$, $\alpha_p^o = 0.005$, $\dot{\alpha}_p^o = 0.10$ (a)The loading bending constitutive response for tensile loading. (b)The bending constitutive response for loading and unloading for both tensile and compressive loading.

The bending constitutive behavior predicted by the constitutive relation in Eqn. (3.21), the power law yielding moment relation in Eqn. (3.22), and the rate of plastic angle deformation expression in Eqn. (3.23) is shown in Fig 3.4. Fig 3.4a presents the loading bending constitutive response due to tensile loading alone while Fig 3.4b presents the loading and unloading response for both tensile and compressive loading. Fig 3.4b demonstrates the ability of the model to capture the effects of the history of plastic deformation during loading, unloading, and/or reverse loading. Eqns. (3.11 - 3.13) and Eqns. (3.21 - 3.23) which dictate the cell wall constitutive behavior were taken from Ortiz and Stainer (1999) and Cuitiño and Ortiz (1992) which provide guidelines on the selection of plastic constitutive updates. Similar simpler equations exist for polymeric visco-elastic ligaments where history of deformation is not relevant.

3.3 Predictions

This section presents the predictions for metallic open-cell foams based on the expressions presented here to describe elasto-plastic cell wall constitutive behavior. The effective foam response predictions are based on the micromechanical unit cell model

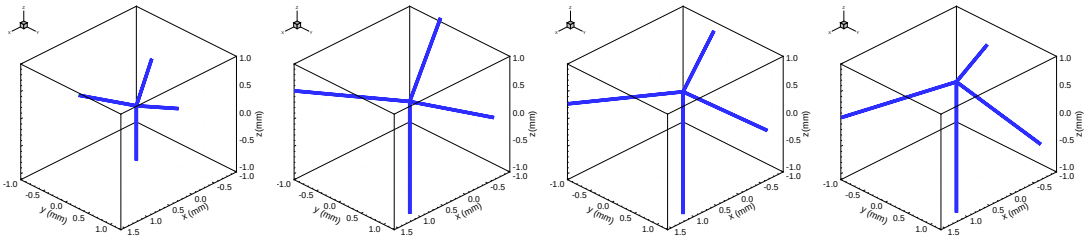

(a) 0% deformation (b) 10% deformation (c) 30% deformation (d) 50% deformation

Figure 3.5: The predicted evolution of the unit cell configuration during compressive loading The variables in Eqns. (3.11 - 3.13) and Eqns. (3.21 - 3.23) were set to *initial strut length* $L_o = 1.0mm$, *initial strut radius* $r_o = 0.3mm$, $E = 50Gpa$, $\sigma_{yo} = 50Mpa$, *axial exponent* $r = 4$, *axial exponet* $m = 4$, $\epsilon_p^o = 0.005$, $\dot{\epsilon}_p^o = 0.10$, *bending exponet* $r = 4$, *bending exponent* $m = 20$, $\alpha_p^o = 0.005$, $\dot{\alpha}_p^o = 0.10$

formulated in Chapter 2 and briefly reviewed in Sec. 3.2.1 of this chapter. Keep in mind that the strut constitutive relations for axial and bending elasto-plastic behavior described in Sec. 3.2.2 and Sec. 3.2.2 respectively dictate the predictions of the unit cell model and therefore the effective foam response. For the following predictions we consider a four strut unit cell ($M = 4$). The struts composing the unit cells are taken as cylindrical rods of initial length L_o and radius r_o with the following initial orientations:

$$\begin{aligned} L_\alpha^1 &= L_o\left(\frac{2\sqrt{2}}{2}e_\alpha^2 + \frac{1}{3}e_\alpha^3\right) \\ L_\alpha^2 &= L_o\left(\frac{\sqrt{6}}{3}e_\alpha^1 - \frac{\sqrt{2}}{3}e_\alpha^2 + \frac{1}{3}e_\alpha^3\right) \\ L_\alpha^3 &= L_o\left(\frac{-\sqrt{6}}{3}e_\alpha^1 - \frac{\sqrt{2}}{3}e_\alpha^2 + \frac{1}{3}e_\alpha^3\right) \\ L_\alpha^4 &= L_o\left(-e_\alpha^3\right) \end{aligned} \tag{3.26}$$

where the terms in parenthesis are unit vectors describing the initial ligament orientation and e_α^i is a local Cartesian coordinate basis centered at the initial vertex of the unit cell. The configurational evolution of a four ligament unit cell $M = 4$ as predicted by Eqn. (4.47) is shown in Fig. 3.5 at four different values of deformation.

Multiple predictions of the effective foam response as predicted by Eqn. 3.5 are presented next. The effective plateau stress presented here is obtained from the microscopic simulation by convexification of the non-convex portion of the microscopic energy landscape as discussed in *chapter* 3 of Ericksen (1998), Gioia et al. (2001) in the

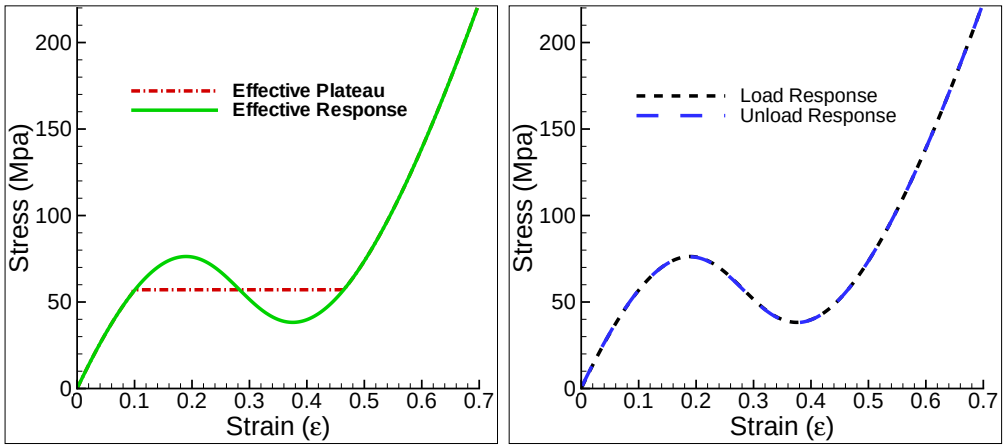

(a) Elastic Response (b) Load, Unload Response

Figure 3.6: The effective response for foams with elastic cell walls. The values for the variables in Eqns. 3.11-3.13 and Eqns. 3.21-3.23 were set to *initial initial length* $L_o = 1.0mm$, *initial strut radius* $r_o = 0.3mm$, $E = 10Gpa$, $\sigma_{yo} = 0.5Gpa$, *axial exponent* $r = 1$, *axial exponet* $m = 1$, $\epsilon_p^o = 0.005$, $\dot{\epsilon}_p^o = 0.10$, *bending exponet* $r = 1$, *bending exponent* $m = 1$, $\alpha_p^o = 0.005$, $\dot{\alpha}_p^o = 0.10$ (a) The effective cell and plateau response for foams composed from struts with a high initial yield stress such that the response doesn't involve any plastic deformation. (b) The load and unload response when the cell walls (struts) don't undergo any plastic deformation.

appendix A. Fig. 3.6a shows the effective unit cell and plateau response for foams composed from elastic ligaments which never undergo yielding deformation while Fig. 3.7a shows the effective unit cell and plateau response for foams composed from elasto-plastic (metallic) ligaments which undergo yielding during plastic deformation. Fig. 3.6b shows the loading/unloading unit cell response for foams that don't yield during deformation. Fig. 3.7b on the other had shows the loading/unloading response when the ligaments composing the unit cell undergo plastic yielding deformation. The current elasto-plastic relations for the cell wall material capture the expected plastic phenomena. Namely that if the cell wall material undergoes yielding, the loading/unloading responses have distinct paths with a large residual deformation (Fig. 3.7b) while if the cell wall material doesn't undergo yielding, the loading/unloading responses have identical paths without any residual deformation (Fig. 3.6b).

Fig. 3.8 presents the predicted effects of the cell wall initial yield stress σ_{yo} on the plateau stress on a metallic open-cell foam. Fig. 3.8a shows how the effective foam response (solid line) with the effective plateau stress (dashed line) while Fig. 3.8b

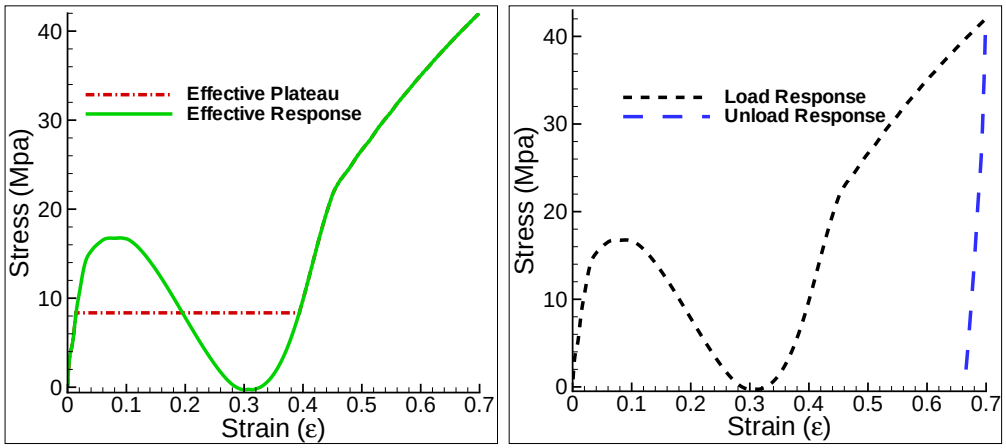

(a) Elasto-Plastic Response (b) Load, Unload Response

Figure 3.7: The effective response for foams with elasto-plastic cell walls. The values for the variables in Eqns. 3.11-3.13 and Eqns. 3.21-3.23 were set to *initial strut length* $L_o = 1.0mm$, *initial strut radius* $r_o = 0.3mm$, $E = 50Gpa$, $\sigma_{yo} = 50Mpa$, *axial exponent* $r = 4$, *axial exponet* $m = 4$, $\epsilon_p^o = 0.005$, $\dot{\epsilon}_p^o = 0.10$, *bending exponet* $r = 4$, *bending exponent* $m = 20$, $\alpha_p^o = 0.005$, $\dot{\alpha}_p^o = 0.10$ (a) The effective cell and plateau response for foams composed from struts with low initial yield stress such that the response involves a lot of plastic deformation. (b) The load and unload response when the cell walls (struts) undergo plastic deformation.

presents the effects of the initial yield stress on effective plateau stress. As expected the plateau stress increases as the yield stress increases as shown in Fig. 3.8. Fig. 3.9 presents the effects of the applied strain on the effective plateau stress of metallic open-cell foams. Fig. 3.9a presents the effects of the applied strain on the effective foam response (solid line) along with the plateau stress (dashed line). Fig. 3.9b presents the effects of the applied strain on the plateau stress. Again as expected, the plateau stress increases as the strain rate increases. Fig. 3.10 presents the effects of the initial rate of plastic deformation $\dot{\epsilon}_o^p$ on the effective foam response. The results in Fig. 3.10 can be interpreted as the effects of viscosity η because for the current strut constitutive formulation the viscosity can be written in terms of the initial yield stress and the initial rate of plastic deformation, e.g. $\eta = \frac{\sigma_{yo}}{\dot{\epsilon}_o^p}$. Fig. 3.10a presents the effects of the initial rate of plastic deformation on the effective response while Fig. 3.10b presents the effect on the plateau stress.

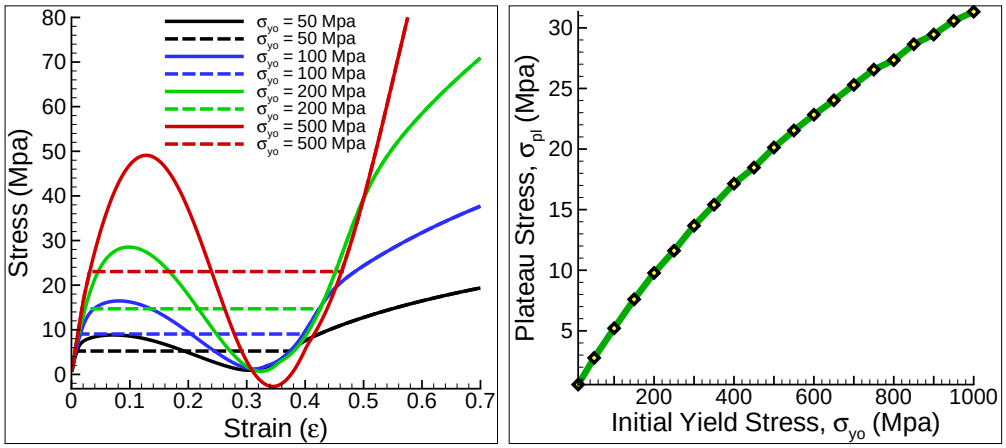

(a) Predicted response (b) Plateau Stress

Figure 3.8: The effect of initial yield stress on the response of metallic, open-cell foams. The foam density was taken as $100Kg/m^3$ and every run was carried out at a strain rate of $1s^{-1}$. The values for the variables in Eqns. 3.11-3.13 and Eqns. 3.21-3.23 were set to *initial strut length* $L_o = 1.0mm$, *initial strut radius* $r_o = 0.3mm$, $E = 50Gpa$, *axial exponent* $r = 4$, *axial exponet* $m = 4$, $\epsilon_p^o = 0.005$, $\dot{\epsilon}_p^o = 0.10$, *bending exponet* $r = 4$, *bending exponent* $m = 20$, $\alpha_p^o = 0.005$, $\dot{\alpha}_p^o = 0.10$ (a) The effective cell response (solid line) and the effective plateau (dashed line) for foams composed of struts with different initial yield stress σ_{yo}. (b) The effect of the initial yield stress σ_{yo} on the predicted effective plateau stress for metallic open-cell foams.

3.4 Conclusions

In summary, the present theory allows one to define a constitutive formulation for lightweight, open-celled metallic foams based on clear and quantifiable parameters such as microstructural topology and cell wall properties such as Youngs modulus and density while capturing the effects of dynamic loading via viscosity (initial yield stress and initial rate of plastic deformation) at cell wall level and microinertia at unit cell level. We limited the presented predictions to cells containing 4 struts converging into the internal cell vertex. A coherent cellular solid can be generated from this type of unit cell by recursive application of point symmetry operations centered on each of the ligament midpoints as previously reported in Wang and Cuitiño (2000). The microscopic results predicted the expected foam response with the plateau stress increasing for increasing applied strain rate, increasing initial cell wall yield stress, and increasing cell wall viscosity. The resulting model accounts explicitly for the foam topology, the elastic and plastic behavior of the cell wall material, and the inertial effects arising from non-affine

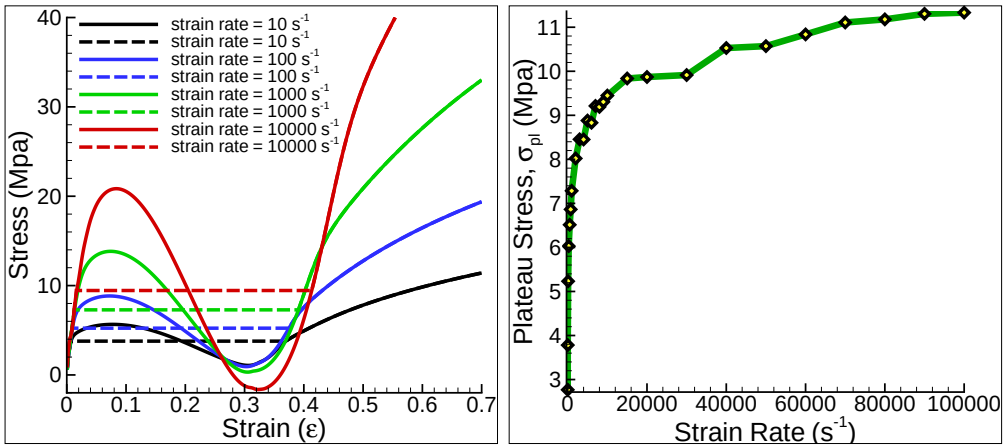

(a) Predicted response (b) Plateau Stress

Figure 3.9: The effect of applied strain rate on the response of metallic, open-cell foams. The foam density was taken as $100Kg/m^3$ and the values for the variables in Eqns. 3.11-3.13 and Eqns. 3.21-3.23 were set to *initial strut length* $L_o = 1.0mm$, *initial strut radius* $r_o = 0.3mm$, $E = 50Gpa$, $\sigma_{yo} = 50Mpa$, *axial exponent* $r = 4$, *axial exponet* $m = 4$, $\epsilon_p^o = 0.005$, $\dot{\epsilon}_p^o = 0.10$, *bending exponet* $r = 4$, *bending exponent* $m = 20$, $\alpha_p^o = 0.005$, $\dot{\alpha}_p^o = 0.10$ (a) The effective cell response (solid line) and the effective plateau (dashed line) for foams loaded at different strain rates $\dot{\epsilon}$. (b) The effect of the applied strain rate $\dot{\epsilon}$ on the predicted effective plateau stress for metallic open-cell foams.

motion within the cells. Finally, we point out that the current approach for modeling the plastic behavior of the ligaments doesn't account for softening and eventual fracture of the ligaments and it also doesn't account for the Bauschinger effect that results form loading-unloading and reverse loading which effects the ability of model to simulate the response at exceedingly high levels of deformation.

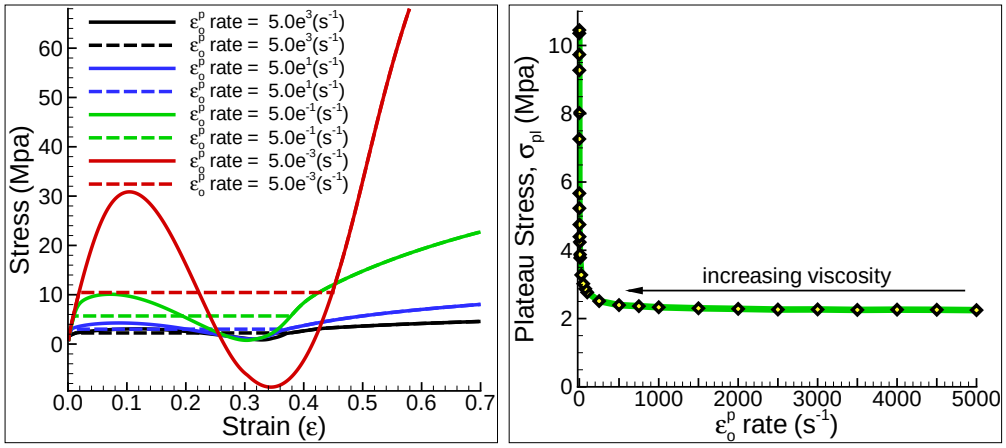

(a) Predicted response (b) Plateau Stress

Figure 3.10: The effect of the initial rate of plastic deformation ($\dot{\epsilon}_o^p$ *and* $\dot{\alpha}_o^p$) on the response of metallic, open-cell foams. The foam density was taken as $100Kg/m^3$, the applied strain was maintained at $1000s^{-1}$ and the values for the variables in Eqns. 3.11-3.13 and Eqns. 3.21-3.23 were set to *initial strut length* $L_o = 1.0mm$, *initial strut radius* $r_o = 0.3mm$, $E = 50Gpa$, $\sigma_{yo} = 50Mpa$, *axial exponent* $r = 4$, *axial exponet* $m = 4$, $\epsilon_p^o = 0.005$, *bending exponet* $r = 4$, *bending exponent* $m = 20$, $\alpha_p^o = 0.005$, (a) The effective cell response (solid line) and the effective plateau (dashed line) for foams loaded at different initial rates of plastic deformation. (b) The effect of initial rate of plastic deformation on the on the predicted effective plateau stress for metallic open-cell foams.

Chapter 4

Harnessing Continuum Mechanics and Finite Element Analysis Schemes to Predict the Behavior of Open-Cell Foams

This chapter presents an approach for modeling and simulating porous, open-cell foam materials using the established ideas of continuum nonlinear finite element analysis (FEA). The approach is valid for cases where the microstructural dimensions of the cells are much smaller than the macroscopic dimensions of the specimen under analysis. While the FEA simulations are performed at continuum level; the stresses at every node in the FEA mesh are obtained from a surrogate micromechanical model which predicts the effective foam response based on the cellular topology and the properties and constitutive behavior of the solid phase making up the cellular architecture which was presented in Chapter 2. The consistent tangents which are necessary in an implicit FEA scheme will be formulated here based on the micromechanical constitutive relation formulated in Chapter 2 which is depends on the axial and bending constitutive behavior considered for the cell wall material. The formulation captures the process of cell collapse by allowing non-affine deformation at unit cell level while maintaining affine deformation at the continuum level. The formulation is then used to predict the response of various Elasto-Plastic and Visco-Elastic Open-Cell Foams specimens for deformations up to 70%. The simulations capture the different stages of foam deformation including the plateau region which occurs during unstable cell collapse. The local strain evolution exhibits the expected heterogeneous deformation through localized bands of collapsed and un-collapsed cells. The effects of cell wall material properties as well as the effects of cellular structure topological alterations on predicted response are also shown.

4.1 Introduction

Cellular materials such as metallic and polymeric open-celled foams are gaining preference in different engineering applications requiring mitigation of energy during sudden impact loading. However before industry can take full of advantage of the properties offered by foam materials, it is necessary to develop tools capable of predicting the full field response under adverse loading conditions. The full range macroscopic dynamic response of foam materials is characterized by an initial elastic region (usually linear) followed by a long plateau region due to unstable collapse of cells and concluded by a densification region after termination of cell collapse. This mechanical response is dominated by the topology of the cellular structure and the properties and constitutive behavior of the solid phase. The majority of the pioneering studies on the mechanics, characterization and properties of metallic foams have been well documented in reviews such as Gibson (2000); Ashby et al. (2000); Gibson and Ashby (1997); Evans et al. (1999). More recently, experimental and modeling studies have concentrated on the different stages of deformation as well as on the effects of the cell wall properties on the macroscopic response of open-cell foams, for instance Bardenhagen et al. (2005); Gong et al. (2005); Zhou et al. (2004a). Due to the recent interest in exploiting foams for energy absorption applications, there has been a number of experimental studies focusing on the dynamic response of metallic foam materials for example Mukai et al. (1999a,b); Shimojima et al. (2001); Dannemann and Lankford (2000); Kanahashi et al. (2001); Han et al. (1998); Hall et al. (2000).

Predicting the full range response of foam materials by modeling the entire cellular structure and keeping track of the motion and deformation of the solid cell wall composing each cell in the cellular structure is extremely challenging theoretically due to intricate cellular architectures and diverse materials properties in multiple phases and to many issues which arise during loading such as considerably large deformation, contact among cell walls, random heterogeneous unstable collapse, multiple deformation phenomena (elasticity, plasticity, fracture) etc. Therefore, it would be computationally unfeasible to perform an FEM numerical analysis on the entire cellular structure while

taking into account the deformation of every cell in the specimen under consideration. One of the most efficient ways to predict the response of a material is by modeling the material as a continuum and then modeling the continuum system with finite elements. Foam materials however have a high degree of porosity and therefore can not be modeled as standard continuum systems. Zooming into a cellular solid reveals many voids and a network of cells made of trusses for open-cell foams and spherical walls, membranes, for closed-cell foams. This means the constitutive relation would not apply equally at every material point throughout the continuum body. The local constitutive equation only applies to the solid cell walls. It is know that even though cellular materials are predominantly composed by voids filled with a fluid, typically air, the effective foam response is dominated by the characteristics of the cells such as the orientation and dimensions and the cell wall materials properties such as elasticity and viscosity.

This communication offers an efficient approach for modeling porous foam materials as continuum systems in order to exploit the established ideas of the finite element method (FEM). In order for the current approach to be valid, it is implicitly assumed that there exists a length scale separation where the microstructural dimensions of the cells are much smaller than the macroscopic dimensions of the sample. In this context, a macroscopic continuum level material point $\mathbf{X}$ translates into a microscopic array of identical unit cells sharing the same macroscopic fields. This is essentially the technique of internal variables where a local minimum of the energy is reached at a local level through the variation of the internal variables and then a global minimum is reached by satisfying all the local minimums is the region under consideration. In this approach the global macroscopic perspective appears as a standard continuum body with mathematical points described by $\mathbf{X}$ and containing certain values of deformation $\mathbf{F}$, displacement $\mathbf{u}$, acceleration $\ddot{\mathbf{u}}$, density ρ, viscosity η etc. At continuum level it is not possible so see a cell's shape or how the cells move and deform. The details of the cellular structure only become apparent upon zooming into a mathematical point $\mathbf{X}$.

In the current approach, the effective macroscopic response such as cellular kinematic state, stresses, and stress tangents at every node in the nonlinear FEA mesh is obtained from a surrogate microscopic structural model which enforces the principle

of minimum action on a representative $3D$ unit cell. The micromechanical unit cell model in turn depends on a third phenomenological model for the elasto-plastic or visco-elastic constitutive behavior of the solid cell wall material. This chapter presents the coherent application of a global nonlinear implicit finite element analysis scheme, the local micromechanical unit cell model and sample local visco-elastic and elasto-plastic constitutive relations. The resulting FEA simulations clearly capture the different stages of deformation observed during dynamic compression experiments of open-cell foam materials. The remainder of this chapter is organized in the following manner. Section 4.2 will state the general continuum mechanics framework in the reference configuration. Section 4.3 will present the finite element analysis framework including the spatial and temporal discretizations. Section 4.4 will restate the key details of the micromechanical model which serves as the constitutive update at every node in the FEA mesh. The consistent tangents necessary in implicit FEM schemes will be formulated in Section 4.4.3 from the reported micromechanical model. Section 4.5 will present sample predictions for both elasto-plastic and visco-elastic open-cell foams. Finally Section 4.6 will pose some concluding statements for the work presented here.

4.2 Continuum Framework

A cellular solid (foam material) can be approximated as a continuum system at the macroscale when the size of the specimen under consideration is much larger than the size of the cells composing the cellular structure. In solid mechanics such a system as depicted in Figure 4.1 can be described by the field equations of continuum mechanics. In the reference configuration and in terms of the First Piola-Kirchhoff stress tensor $\mathbf{P}(\mathbf{X},t)$ with Cartesian components P_{iJ}, the governing field equations of continuum mechanics acquire the following form:

$$\begin{aligned} \textit{Conservation of linear momentum} \quad &: \\ \mathbf{P}(\mathbf{X},t)\cdot\overleftarrow{\nabla}_{\mathbf{X}} + \rho_o\,\tilde{\mathbf{b}}(\mathbf{X},t) \quad &= \quad \rho_o\,\ddot{\mathbf{u}}(\mathbf{X},t) \qquad (4.1) \\ \textit{Conservation of angular momentum} \quad &: \\ \mathbf{P}(\mathbf{X},t)\cdot\mathbf{F}^T(\mathbf{X},t) \quad &= \quad \mathbf{F}(\mathbf{X},t)\cdot\mathbf{P}^T(\mathbf{X},t) \qquad (4.2) \end{aligned}$$

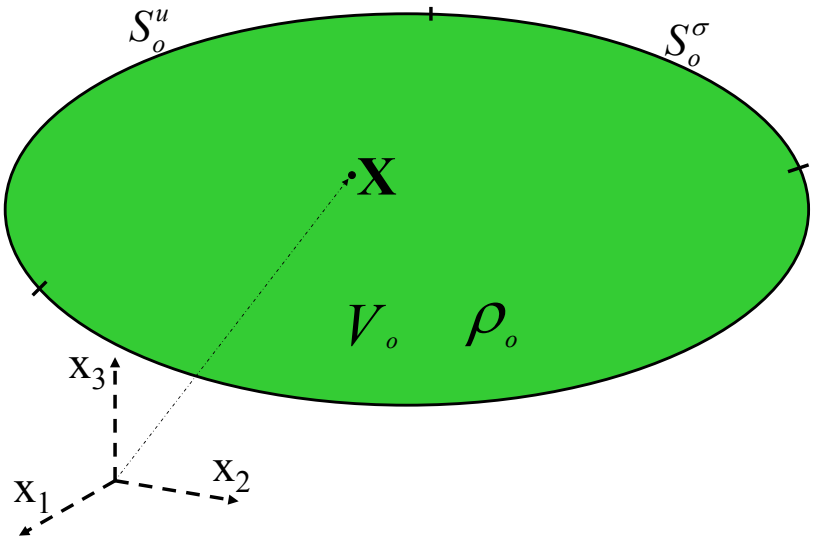

Figure 4.1: Schematic of the foam system as a continuum body with prescribed boundary conditions and initial conditions.

$$\textit{Traction boundary conditions} \quad :$$

$$\mathbf{P}(\mathbf{X},t)\cdot\mathbf{N} = \tilde{\mathbf{t}}(\mathbf{X},t) \quad \textit{on } \mathcal{S}_o^\sigma \tag{4.3}$$

$$\textit{Displacement boundary conditions} \quad :$$

$$\mathbf{u}(\mathbf{X},t) = \tilde{\mathbf{u}}(\mathbf{X},t) \quad \textit{on } \mathcal{S}_o^u \tag{4.4}$$

Here $\mathbf{X}$ represents the position of a material particle in the original or reference configuration. At time t the same material particle is located at position $\mathbf{x}$ in the current or deformed configuration. $\tilde{\mathbf{b}}$ refers to the body force per unit mass and ρ_o to the mass density per unit reference volume and $\mathbf{u}$ and $\ddot{\mathbf{u}}$ refer respectively to the displacement and acceleration throughout the body. In addition, $\tilde{\mathbf{t}}$ and $\tilde{\mathbf{u}}$ are the prescribed traction and imposed displacement along the traction surface $\mathcal{S}_o^\sigma$ and displacement surface $\mathcal{S}_o^u$ respectively. Finally, $\mathbf{N}$ is the surface unit normal in the reference configuration.

4.2.1 Derivation of the Weak Form

The *strong* form of the balance of linear momentum stated in Equation 4.1 can be recast in a *weak* form by invoking the Principle of Virtual Work. First the *strong* form given

in Equation 4.1 is multiplied by an arbitrary virtual displacement $\delta\mathbf{u}$ which satisfies the prescribed displacement ($\tilde{\mathbf{u}}$) boundary condition on $\mathcal{S}_o^u$ and then the expression is integrated over the reference volume V_o as shown below

$$\int_{V_o} \delta\mathbf{u} \cdot (\mathbf{P} \cdot \overleftarrow{\nabla}_{\mathbf{X}} + \rho_o \tilde{\mathbf{b}} - \rho_o \ddot{\mathbf{u}}) \; dV_o = \mathbf{0} \tag{4.5}$$

Separating each term in equation 4.5 gives

$$\int_{V_o} \delta\mathbf{u} \cdot (\mathbf{P} \cdot \overleftarrow{\nabla}_{\mathbf{X}}) \; dV_o + \int_{V_o} \rho_o \delta\mathbf{u} \cdot \tilde{\mathbf{b}} \; dV_o - \int_{V_o} \rho_o \delta\mathbf{u} \cdot \ddot{\mathbf{u}} \; dV_o = \mathbf{0} \tag{4.6}$$

Now notice that the first term in Equation 4.6 can be written as

$$\int_{V_o} \delta\mathbf{u} \cdot (\mathbf{P} \cdot \overleftarrow{\nabla}_{\mathbf{X}}) \; dV_o = \int_{V_o} (\delta\mathbf{u} \cdot \mathbf{P}) \cdot \overleftarrow{\nabla}_{\mathbf{X}} \; dV_o - \int_{V_o} \mathbf{P}{:}(\delta\mathbf{u} \overleftarrow{\nabla}_{\mathbf{X}}) \; dV_o \tag{4.7}$$

since

$$\begin{aligned} (\delta\mathbf{u} \cdot \mathbf{P}) \cdot \overleftarrow{\nabla}_{\mathbf{X}} &= \delta\mathbf{u} \cdot (\mathbf{P} \cdot \overleftarrow{\nabla}_{\mathbf{X}}) + \mathbf{P}{:}(\delta\mathbf{u} \overleftarrow{\nabla}_{\mathbf{X}}) \qquad (4.8) \\ &\textit{or} \\ (\delta u_i P_{iJ}) \frac{\partial}{\partial X_J} &= \delta u_i \frac{\partial P_{iJ}}{\partial X_J} + P_{iJ} \frac{\partial \delta u_i}{\partial X_J} \end{aligned}$$

Making use of Gauss' theorem to convert the first term on the right side of Equation 4.7 from a volume integral to a surface integral on the reference configuration with unit surface normal $\mathbf{N}$ gives

$$\int_{V_o} \delta\mathbf{u} \cdot (\mathbf{P} \cdot \overleftarrow{\nabla}_{\mathbf{X}}) \; dV_o = \int_{S_o} \delta\mathbf{u} \cdot \mathbf{P} \cdot \mathbf{N} \; dS_o - \int_{V_o} \mathbf{P}{:}(\delta\mathbf{u} \overleftarrow{\nabla}_{\mathbf{X}}) \; dV_o \tag{4.9}$$

Further noticing that $\mathbf{t} = \mathbf{P} \cdot \mathbf{N}$ gives

$$\int_{V_o} \delta\mathbf{u} \cdot (\mathbf{P} \cdot \overleftarrow{\nabla}_{\mathbf{X}}) \; dV_o = \int_{S_o} \delta\mathbf{u} \cdot \mathbf{t} \; dS_o - \int_{V_o} \mathbf{P}{:}(\delta\mathbf{u} \overleftarrow{\nabla}_{\mathbf{X}}) \; dV_o \tag{4.10}$$

Now, recalling that on the portion of the boundary (S_o^σ) where a traction BC ($\tilde{\mathbf{t}}$) is specified we have

$$\delta\mathbf{u} \cdot (\mathbf{P} \cdot \mathbf{N}) \equiv \delta u_i P_{iJ} N_J = \delta\mathbf{u} \cdot \tilde{\mathbf{t}} \tag{4.11}$$

and on the portion of the boundary where no tractions are specified, we have

$$\delta\mathbf{u} \cdot (\mathbf{P} \cdot \mathbf{N}) = \mathbf{0} \quad \textit{or} \quad \mathbf{t} = \mathbf{0} \tag{4.12}$$

allows us to write Equation 4.10 as

$$\int_{V_o} \delta\mathbf{u} \cdot (\mathbf{P} \cdot \overleftarrow{\nabla}_{\mathbf{X}})\ dV_o = \int_{S_o^\sigma} \delta\mathbf{u} \cdot \tilde{\mathbf{t}}\ dS_o - \int_{V_o} \mathbf{P}{:}(\delta\mathbf{u}\overleftarrow{\nabla}_{\mathbf{X}})\ dV_o \tag{4.13}$$

Substituting Equation 4.13 into Equation 4.6 and rearranging gives

$$\int_{S_o^\sigma} \delta\mathbf{u} \cdot \tilde{\mathbf{t}}\ dS_o + \int_{V_o} \rho_o \delta\mathbf{u} \cdot \tilde{\mathbf{b}}\ dV_o - \int_{V_o} \mathbf{P}{:}(\delta\mathbf{u}\overleftarrow{\nabla}_{\mathbf{X}})\ dV_o = \int_{V_o} \rho_o \delta\mathbf{u} \cdot \ddot{\mathbf{u}}\ dV_o \tag{4.14}$$

Equation 4.14 above is the *weak* form of the balance of linear momentum stated earlier in Equation 4.1. Given a proper constitutive relation $\mathbf{P}(\mathbf{F}(t))$ for the continuum foam system, the continuum problem can be solved numerically by employing the finite element method. Before presenting the details of the micromechanical model which furnishes the necessary constitutive expression $\mathbf{P}(\mathbf{F}(t))$, the next section discretizes Equation 4.14 in space and time in order to provide a brief overview of the general finite element analysis method.

4.3 Finite Element Analysis Framework

In an effort to make this a self-contained communication as self-contained, this section presents a brief overview of the general finite element analysis (FEA) framework. The finite element method provides an approximation of the gradual response of the continuum body for an incrementally applied load. The Finite Element Method essentially enforces the weak form of the balance of linear momentum stated in Equation 4.14 along with the specified boundary and initial conditions on every element in the discretized form of the continuum body at every instant of the incrementally applied load. Before discretizing the problem in space and time, notice that the weak balance of momentum expression in Equation 4.14 can be written as

$$\begin{aligned} \int_{S_o^\sigma} \delta\mathbf{u}^T \cdot \tilde{\mathbf{t}}^T\ dS_o + \int_{V_o} \rho_o \delta\mathbf{u}^T \cdot \tilde{\mathbf{b}}^T\ dV_o \ &- \int_{V_o} (\delta\mathbf{u}\overleftarrow{\nabla}_{\mathbf{X}}){:}\mathbf{P}\ dV_o \\ &= \int_{V_o} \rho_o \delta\mathbf{u}^T \cdot \ddot{\mathbf{u}}^T\ dV_o \end{aligned} \tag{4.15}$$

and recalling that for any two tensors $\mathbf{A}$ and $\mathbf{B}$, $\mathbf{A}{:}\mathbf{B} = \mathbf{B}{:}\mathbf{A} = \mathbf{A}^T \cdot\cdot \mathbf{B} = \mathbf{A} \cdot\cdot \mathbf{B}^T$, then Equation 4.15 can be rewritten as

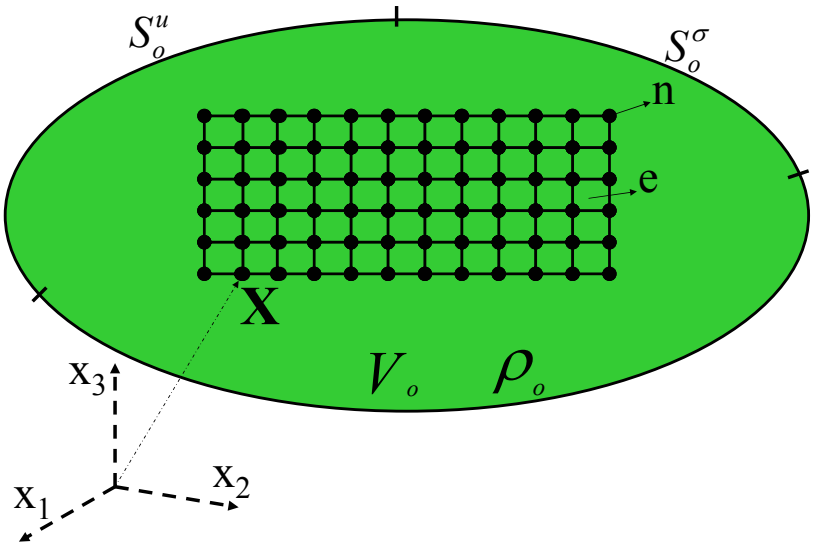

Figure 4.2: Schematic representation of the spatially discretized continuum body. Each element is assigned a number e and every node is assigned a number n.

$$\int_{S_o^\sigma} \delta\mathbf{u}^T \cdot \tilde{\mathbf{t}}\ dS_o + \int_{V_o} \rho_o \delta\mathbf{u}^T \cdot \tilde{\mathbf{b}}\ dV_o \ - \ \int_{V_o} (\delta\mathbf{u}\overleftarrow{\nabla}_{\mathbf{X}})^T \cdot\cdot \mathbf{P}\ dV_o = \int_{V_o} \rho_o \delta\mathbf{u}^T \cdot \ddot{\mathbf{u}}\ dV_o \tag{4.16}$$

4.3.1 Spatial Discretization

This sections presents the discretization of the body in space. Figure 4.2 depicts the discretized form of the continuum body with every element numbered by e and every node numbered by n. A set of shape (interpolation) functions are represented by $\mathbf{N} = \mathbf{N}(\mathbf{X})$ and the nodal displacement, velocity, and acceleration by $\mathbf{U}$, $\dot{\mathbf{U}}$, $\ddot{\mathbf{U}}$ respectively. The continuum displacement, velocity, and acceleration are represented by $\mathbf{u}(\mathbf{X})$, $\dot{\mathbf{u}}(\mathbf{X})$, $\ddot{\mathbf{u}}(\mathbf{X})$ respectively and are expressed in terms of the shape functions and discrete nodal values as written below

$$\mathbf{u}(\mathbf{X}) = \mathbf{N}(\mathbf{X})\mathbf{U} \qquad \delta\mathbf{u}(\mathbf{X}) = \mathbf{N}(\mathbf{X})\delta\mathbf{U} \qquad \delta\mathbf{u}^T(\mathbf{X}) = \delta\mathbf{U}^T\mathbf{N}^T(\mathbf{X}) \tag{4.17}$$

$$\dot{\mathbf{u}}(\mathbf{X}) = \mathbf{N}(\mathbf{X})\dot{\mathbf{U}} \qquad \delta\dot{\mathbf{u}}(\mathbf{X}) = \mathbf{N}(\mathbf{X})\delta\dot{\mathbf{U}} \qquad \delta\dot{\mathbf{u}}^T(\mathbf{X}) = \delta\dot{\mathbf{U}}^T\mathbf{N}^T(\mathbf{X}) \tag{4.18}$$

$$\ddot{\mathbf{u}}(\mathbf{X}) = \mathbf{N}(\mathbf{X})\ddot{\mathbf{U}} \qquad \delta\ddot{\mathbf{u}}(\mathbf{X}) = \mathbf{N}(\mathbf{X})\delta\ddot{\mathbf{U}} \qquad \delta\ddot{\mathbf{u}}^T(\mathbf{X}) = \delta\ddot{\mathbf{U}}^T\mathbf{N}^T(\mathbf{X}) \tag{4.19}$$

The deformation gradient $\mathbf{F}$ can also de expressed in term of the nodal values as

$$\mathbf{F} = \mathbf{u}\overleftarrow{\nabla}_{\mathbf{X}} - \mathbf{I} = \mathbf{N}\overleftarrow{\nabla}_{\mathbf{X}}\mathbf{U} - \mathbf{I} = \mathbf{B}\mathbf{U} - \mathbf{I} \tag{4.20}$$

$$\delta\mathbf{F} = \delta\mathbf{u}\overleftarrow{\nabla}_{\mathbf{X}} - \mathbf{I} = \mathbf{N}\overleftarrow{\nabla}_{\mathbf{X}}\delta\mathbf{U} - \mathbf{I} = \mathbf{B}\delta\mathbf{U} - \mathbf{I} \tag{4.21}$$

$$\delta\mathbf{F}^T = (\delta\mathbf{u}\overleftarrow{\nabla}_{\mathbf{X}})\,T - \mathbf{I} = (\mathbf{N}\delta\mathbf{U}\overleftarrow{\nabla}_{\mathbf{X}})\,T - \mathbf{I} = \delta\mathbf{U}^T\mathbf{B}^T - \mathbf{I} \tag{4.22}$$

Now substituting for $\ddot{\mathbf{u}}$, $\delta\mathbf{u}^T$ and $(\delta\mathbf{u}\overleftarrow{\nabla}_{\mathbf{X}})^T$ from Equations 4.17 - 4.19 into Equation 4.16 results in

$$\begin{aligned}\int_{S_o^\sigma} \delta\mathbf{U}^T\mathbf{N}^T\cdot\tilde{\mathbf{t}}\;dS_o + \int_{V_o}\rho_o\delta\mathbf{U}^T\mathbf{N}^T\cdot\tilde{\mathbf{b}}\;dV_o \;&-\; \int_{V_o}\delta\mathbf{U}^T\mathbf{N}^T\overleftarrow{\nabla}_{\mathbf{X}}\cdot\cdot\mathbf{P}\;dV_o \\ &= \int_{V_o}\rho_o\delta\mathbf{U}^T\mathbf{N}^T\cdot\mathbf{N}\ddot{\mathbf{U}}\;dV_o\end{aligned} \tag{4.23}$$

Now substituting $\mathbf{B}^T = \mathbf{N}^T\overleftarrow{\nabla}_{\mathbf{X}}$ and factoring out $\delta\mathbf{U}^T$ gives

$$\delta\mathbf{U}^T\left[\int_{S_o^\sigma}\mathbf{N}^T\cdot\tilde{\mathbf{t}}\;dS_o + \int_{V_o}\rho_o\mathbf{N}^T\cdot\tilde{\mathbf{b}}\;dV_o - \int_{V_o}\mathbf{B}^T\cdot\cdot\mathbf{P}\;dV_o = \int_{V_o}\rho_o\mathbf{N}^T\cdot\mathbf{N}\ddot{\mathbf{U}}\;dV_o\right] \tag{4.24}$$

In order for Equation 4.24 to be satisfied for any valid virtual displacement field $\delta\mathbf{U}$, the term in square brackets must be satisfied independently at all times. Applying the term in square brackets in Equation 4.24 to every element e and summing over all the elements in the discretized body gives

$$\begin{aligned}\sum_e\int_{S_e^\sigma}\mathbf{N}^T\cdot\tilde{\mathbf{t}}\;dS_o + \sum_e\int_{V_e}\rho_o\mathbf{N}^T\cdot\tilde{\mathbf{b}}\;dV_o \;&-\; \sum_e\int_{V_e}\mathbf{B}^T\cdot\cdot\mathbf{P}\;dV_o \\ &= \sum_e\int_{V_e}\rho_o\mathbf{N}^T\cdot\mathbf{N}\ddot{\mathbf{U}}\;dV_o\end{aligned} \tag{4.25}$$

For convenience, the different terms in Equation 4.25 will be represented by

$$\mathcal{R} = \sum_e\int_{S_e^\sigma}\mathbf{N}^T\cdot\tilde{\mathbf{t}}\;dS_o \tag{4.26}$$

$$\mathcal{G}(\mathbf{U},\dot{\mathbf{U}}) = \sum_e\int_{V_e}\rho_o\mathbf{N}^T\cdot\tilde{\mathbf{b}}\;dV_o - \sum_e\int_{V_e}\mathbf{B}^T\cdot\cdot\mathbf{P}\;dV_o \tag{4.27}$$

$$\mathcal{I}(\ddot{\mathbf{U}}) = \sum_e\int_{V_e}\rho_o\mathbf{N}^T\cdot\mathbf{N}\;dV_o\ddot{\mathbf{U}} \tag{4.28}$$

where $\mathcal{R}$ represents the *external* forces, $\mathcal{G}$ represents the *internal* forces, and $\mathcal{I}$ represents the *inertial* forces. $\mathcal{G}$ is a function of the displacement $\mathbf{U}$ and velocity $\dot{\mathbf{U}}$ because in

general the stress state $\mathbf{P}$ is a function of both strain and strain rate which in turn depend on displacement and velocity.

4.3.2 Temporal Discretization

This section presents the discretization in time of the motion and deformation. The duration of the loading event is discretized in increments of Δt with the previous time represented by t_n and current time represented by t_{n+1}. Then it is necessary to satisfy Equation 4.25 at the current given time t_{n+1}, i.e.

$$\mathcal{G}(\mathbf{U}_{n+1}, \dot{\mathbf{U}}_{n+1}) + \mathcal{I}(\ddot{\mathbf{U}}_{n+1}) = \mathcal{R}_{n+1} \tag{4.29}$$

where $\mathbf{U}_{n+1}$,$\dot{\mathbf{U}}_{n+1}$ and $\ddot{\mathbf{U}}_{n+1}$ are the current nodal values of displacement, velocity, and acceleration on every element. Knowing the conditions at the previous time t_n including the previous nodal values $\mathbf{U}_n$,$\dot{\mathbf{U}}_n$ and $\ddot{\mathbf{U}}_n$, together with a time integration scheme given by

$$\mathbf{U}_{n+1} = \mathbf{U}_n + \Delta t \dot{\mathbf{U}}_n + \frac{\Delta t^2}{2}(1-2\beta)\ddot{\mathbf{U}}_n + \beta \Delta t^2 \ddot{\mathbf{U}}_{n+1} \tag{4.30}$$

$$\dot{\mathbf{U}}_{n+1} = \dot{\mathbf{U}} + \Delta t(1-\gamma)\ddot{\mathbf{U}}_n + \gamma \Delta t \ddot{\mathbf{U}}_{n+1} \tag{4.31}$$

Permits us to determine the necessary values for each incremental time step. Notice that different implicit time integration schemes are possible depending on the selected values for γ and β in Equations 4.30 and 4.31. Notice that for $\beta = \gamma = 0$ we have an explicit integration scheme. Substituting Equations 4.30 and 4.31 into Equation 4.29 gives

$$\mathcal{H}(\ddot{\mathbf{U}}_{n+1}) = \mathcal{G}(\mathbf{U}_{n+1}(\ddot{\mathbf{U}}_{n+1}), \dot{\mathbf{U}}_{n+1}(\ddot{\mathbf{U}}_{n+1})) + \mathcal{I}(\ddot{\mathbf{U}}_{n+1}) = \mathcal{R}_{n+1} \tag{4.32}$$

or simply

$$\mathcal{H}_{n+1}(\ddot{\mathbf{U}}_{n+1}) - \mathcal{R}_{n+1} = 0 \tag{4.33}$$

Equation 4.33 is a nonlinear system of equations for the current nodal acceleration $\ddot{\mathbf{U}}_{n+1}$ which is solved utilizing a Newton Raphson scheme as

$$\ddot{\mathbf{U}}_{n+1} = \ddot{\mathbf{U}}_n - \left[\frac{\partial \mathcal{H}_{n+1}}{\partial \ddot{\mathbf{U}}_{n+1}}\right]^{-1} (\mathcal{H}_{n+1} - \mathcal{R}_{n+1}) \tag{4.34}$$

This iteration scheme necessitates the evaluation and inversion of the modified mass matrix defined as

$$\tilde{\mathbf{M}} = \frac{\partial \mathcal{H}_{n+1}}{\partial \ddot{\mathbf{U}}_{n+1}} = \left[\beta \Delta t^2 \frac{\partial \mathcal{G}_{n+1}}{\partial \mathbf{U}_{n+1}} + \gamma \Delta t \frac{\partial \mathcal{G}_{n+1}}{\partial \dot{\mathbf{U}}_{n+1}} + \frac{\partial \mathcal{I}}{\partial \ddot{\mathbf{U}}_{n+1}}\right] \tag{4.35}$$

where the term $\frac{\partial \mathcal{G}_{n+1}}{\partial \mathbf{U}_{n+1}}$ is the global stiffness matrix. Taking $\mathbf{P} = \mathbf{P}(\mathbf{F}, \dot{\mathbf{F}})$ and making use of Equations 4.29 and 4.27, the global mass matrix can be written as

$$\begin{aligned} \frac{\partial \mathcal{G}_{n+1}}{\partial \mathbf{U}_{n+1}} = \mathbf{K}_{n+1} = \sum_e \mathbf{K}_{e,n+1} &= \sum_e \left[\int_{V_e} \mathbf{B}^T \cdot\cdot \frac{\partial \mathbf{P}}{\partial \mathbf{U}}\, dV_o\right] \\ &= \sum_e \left[\int_{V_e} \mathbf{B}^T \cdot\cdot \frac{\partial \mathbf{P}}{\partial \mathbf{F}} \mathbf{B}\, dV_o\right] \end{aligned} \tag{4.36}$$

where

$$\frac{\partial \mathbf{P}}{\partial \mathbf{U}} = \frac{\partial \mathbf{P}}{\partial \mathbf{F}} \frac{\partial \mathbf{F}}{\partial \mathbf{U}} = \frac{\partial \mathbf{P}}{\partial \mathbf{F}} \mathbf{B} \tag{4.37}$$

since

$$\mathbf{u} \overleftarrow{\nabla}_{\mathbf{X}} = \mathbf{F} + \mathbf{I} \quad \Rightarrow \quad \mathbf{F} = \mathbf{u} \overleftarrow{\nabla}_{\mathbf{X}} - \mathbf{I} = \mathbf{N} \overleftarrow{\nabla}_{\mathbf{X}} \mathbf{U} - \mathbf{I} \quad \Rightarrow \quad \frac{d\mathbf{F}}{d\mathbf{U}} = \mathbf{B} \tag{4.38}$$

The term $\frac{\partial \mathcal{G}_{n+1}}{\partial \dot{\mathbf{U}}_{n+1}}$ represents the damping matrix and can be written as

$$\begin{aligned} \frac{\partial \mathcal{G}_{n+1}}{\partial \dot{\mathbf{U}}_{n+1}} = \mathbf{C}_{n+1} = \sum_e \mathbf{C}_{e,n+1} &= \sum_e \left[\int_{V_e} \mathbf{B}^T \cdot\cdot \frac{\partial \mathbf{P}}{\partial \dot{\mathbf{U}}}\, dV_o\right] \\ &= \sum_e \left[\int_{V_e} \mathbf{B}^T \cdot\cdot \frac{\partial \mathbf{P}}{\partial \dot{\mathbf{F}}} \mathbf{B}\, dV_o\right] \end{aligned} \tag{4.39}$$

where

$$\frac{\partial \mathbf{P}}{\partial \dot{\mathbf{U}}} = \frac{\partial \mathbf{P}}{\partial \dot{\mathbf{F}}} \frac{\partial \dot{\mathbf{F}}}{\partial \dot{\mathbf{U}}} = \frac{\partial \mathbf{P}}{\partial \dot{\mathbf{F}}} \mathbf{B} \tag{4.40}$$

since

$$\dot{\mathbf{u}} \overleftarrow{\nabla}_{\mathbf{X}} = \dot{\mathbf{F}} \quad \Rightarrow \quad \dot{\mathbf{F}} = \dot{\mathbf{u}} \overleftarrow{\nabla}_{\mathbf{X}} = \mathbf{N} \overleftarrow{\nabla}_{\mathbf{X}} \dot{\mathbf{U}} \quad \Rightarrow \quad \frac{d\dot{\mathbf{F}}}{d\dot{\mathbf{U}}} = \mathbf{B} \tag{4.41}$$

The term $\frac{\partial \mathcal{I}_{n+1}}{\partial \ddot{\mathbf{U}}_{n+1}}$ represents the inertial mass matrix and can be written as

$$\frac{\partial \mathcal{I}_{n+1}}{\partial \ddot{\mathbf{U}}_{n+1}} = \mathbf{M} = \sum_e \mathbf{M}_e = \sum_e \left[\int_{V_e} \rho_o \mathbf{N}^T \cdot \mathbf{N}\, dV_o\right] \tag{4.42}$$

The modified mass matrix in Equation 4.35 can now be restated as

$$\tilde{\mathbf{M}} = \frac{\partial \mathcal{H}_{n+1}}{\partial \ddot{\mathbf{U}}_{n+1}} = \left[\beta \Delta t^2 \mathbf{K}_{n+1} + \gamma \Delta t \mathbf{C}_{n+1} + \mathbf{M}\right] \tag{4.43}$$

The micromechanical model formulated in chapter 2 renders $\mathbf{P} = \mathbf{P}(\mathbf{F}(t))$ hence the modified mass matrix won't involve the variation of the stress with respect to the rate of deformation $\frac{\partial \mathbf{P}}{\partial \dot{\mathbf{F}}}$ and will take the simpler form

$$\tilde{\mathbf{M}} = \frac{\partial \mathcal{H}_{n+1}}{\partial \ddot{\mathbf{U}}_{n+1}} = \left[\beta \Delta t^2 \mathbf{K}_{n+1} + \mathbf{M}\right] \tag{4.44}$$

In addition to the terms stated in the modified mass matrix in Equation 4.35, the Newton-Raphson iteration scheme also requires the evaluation of $\mathcal{H}$

$$\mathcal{H}_{n+1} = \sum_e \left[\int_{V_e} \rho_o \mathbf{N}^T \cdot \tilde{\mathbf{b}}_{n+1} - \mathbf{B}^T \cdot \cdot \mathbf{P}_{n+1} + \rho_o \mathbf{N}^T \cdot \mathbf{N}\ \ddot{\mathbf{U}}_{n+1} \right] dV_o \tag{4.45}$$

In order to march in time by utilizing the Newton-Raphson scheme in Equation 4.34, we need to have a constitutive relation $\mathbf{P}$ and its consistent tangents $\frac{d\mathbf{P}}{d\mathbf{F}}$ as required by Equations 4.36 and 4.45. We seek a continuum-level constitutive relation for open-cell foam materials attendant to their internal microstructure and including the inertial effects arising from the internal collapse of the foam structure. In formulating such a constitutive relation, we conceptualize that the material is generated by the systematic repetition of a particular unit cell, the size of which is much smaller than the region of interest (sample). In other words we assume separation of scales where the mechanical response of any material macroscopic point in the body is obtained from a local or microscopic model of the cellular structure as sketched in Figure 4.3. The next sections presents a brief review of the necessary continuum level constitutive relation $\mathbf{P}(\mathbf{F}(t))$ for open-cell foams as recently reported in Romero et al. (2008). The consistent tangents $\frac{d\mathbf{P}}{d\mathbf{F}}$ are then formulated based on the developed constitutive relation.

4.4 Micromechanical Formulation

An separation of scales is implicity assumed by the current formulation where the region of foam material under analysis is much larger then the size of the cells composing the foam's cellular structure as depicted in Figure 4.3a which is repeated here from Chapter 2 for convenience. In this context, the global continuum level perspective is limited to mathematical points designated by $\mathbf{X}$ which contain certain values for an array of variables such deformation $\mathbf{F}$, Stress $\mathbf{P}$, density ρ, viscosity η, etc. The

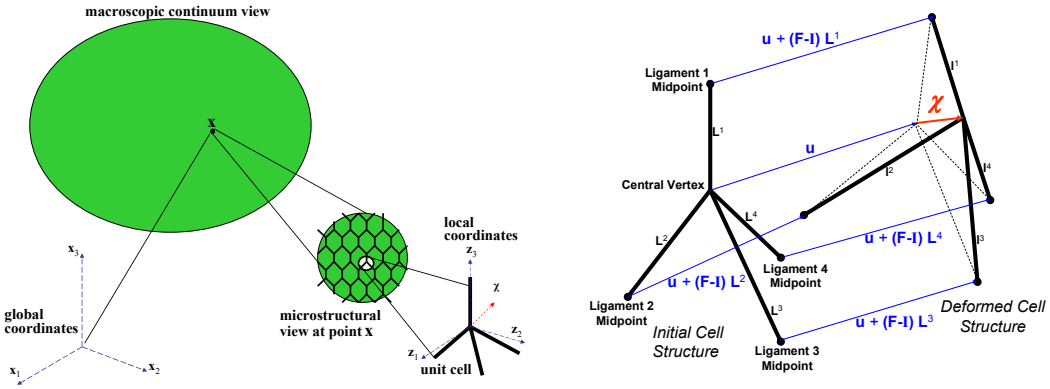

(a) Multiscale Model (b) Unit Cell Motion

Figure 4.3: a) Continuum and microstructural view of foam material composed of very small cells relative to the sample size. The macroscopic fields such as $\mathbf{u}$ and $\mathbf{F}$ prescribed at point $\mathbf{X}$ are trickled down to the microstructure to the midpoints of the ligaments. b) Kinematic assumptions for a 4-ligament unit cell showing the reference and deformed cell configurations. The cell deforms according to the prescribed macroscopic affine field $\mathbf{F}$ and all ligament midpoints move with the specified macroscopic affine field $\mathbf{u}$, however the cell vertex may have the additional displacement $\boldsymbol{\chi}$ resulting in non-affine deformation within the microstructure.

cellular structure only becomes visible after zooming into one of the continuum level mathematical points $\mathbf{X}$. Further zooming into the cellular structure reveals the unit cell along with the shape, dimension, and orientation of each cell wall (strut). The structural level perspective exhibits the motion and deformation of each cell as a whole and the individual deformation of the struts composing it. The cell moves and deforms according to the applied deformation $\mathbf{F}$ however the current approach allows the unit cell vertex to move an additional amount $\boldsymbol{\chi}$ until structural equilibrium is achieved as shown in Figure 4.3b. Keep in mind that the motion of the strut midpoints remains tied to the global continuum deformation $\mathbf{F}$ at all times.

Before presenting the continuum level stress state equation $\mathbf{P}$ and formulating the consistent tangents $\frac{d\mathbf{P}}{d\mathbf{F}}$ which are necessary in any Implicit Finite Element Analysis scheme, it is necessary to link the global heterogeneous deformation field $\mathbf{F}$ to the local field $\boldsymbol{\chi}$ at every global point $\mathbf{X}$. As shown in Figure 4.3 and as reported in Romero et al. (2008), this is done by trickling down from the continuum level to the unit cell level the global field $\mathbf{F}$ and enforcing the principle of minimum action on a representative $3D$ unit cell. This results in an Equation of Motion (EOM) in terms of

$\boldsymbol{\chi}$ which dictates the evolution of the configuration of each unit cell for every globally specified deformation $\mathbf{F}$ at every point $\mathbf{X}$ in the continuum view. Section 4.4.1 will briefly summarize this lengthy derivation previously communicated in Romero et al. (2008) and Section 4.4.2 will state the derived continuum level, First Piola-Kirchoff Stress equation $\mathbf{P}(\mathbf{F}(t))$ which predicts the stress state for every unit cell configuration as required by the applied global deformation $\mathbf{F}$. Finally Section 4.4.3 will formulate the stress tangents necessary to march in the implicit continuum level finite element analysis scheme being implemented here.

4.4.1 Kinematic Equilibrium Condition

We consider a unit cell composed of M ligaments and consider the axial and bending deformation of the ligaments. The bending deformation is concentrated at the cell's vertex and is evaluated as a function of the current angle ψ between every two ligaments. This assumption allows us to capture the unstable buckling process of every unit cell through a single additional degree of freedom $\boldsymbol{\chi}$ which locates the unit cell vertex and results in non-affine motion within the cell. Once the initial length $\mathbf{L}^i$ of every ligament i and the initial angle Ψ^{ij} between every two ligaments i and j in the unit cell are specified and a deformation $\mathbf{F}$ is applied, we need to determine the new lengths and angles for the ligaments composing the unit cell. The current length $\mathbf{l}^i$ of any ligament i and the current angle ψ^{ij} between any two ligaments i and j are respectively defined in Equation 4.46.

$$Kinematics :\Rightarrow \mathbf{l}^i = \mathbf{F}\mathbf{L}^i - \boldsymbol{\chi} \qquad \psi^{ij} = \cos^{-1}\left(\frac{\mathbf{l}^i \cdot \mathbf{l}^j}{l^i\ l^j}\right) \tag{4.46}$$

Once the deformation $\mathbf{F}$ is specified, Equation 4.46 requires the value of $\boldsymbol{\chi}$ in order to determine $\mathbf{l}^i$ and ψ^{ij}. First, notice that once $\mathbf{F}$ is specified at unit cell level, the only degree of freedom in the system is the motion of the central vertex $\boldsymbol{\chi}$ which can be determine by satisfying equilibrium at the unit cell vertex. The Equation of Motion for $\boldsymbol{\chi}$ resulting from application of the principle of minimum action for non-conservative systems, $\frac{d}{dt}\left(\frac{\partial \mathcal{L}}{\partial \dot{\chi}_\alpha}\right) - \frac{\partial \mathcal{L}}{\partial \chi_\alpha} = Q_\alpha$, is presented in Equation 4.47 as a resultant equilibrium

condition.

$$Equilibrium :\Rightarrow \mathbf{R}(\mathbf{F},\boldsymbol{\chi}) = \sum_{i=1,M} \mathbf{f}^i - m_c\ddot{\boldsymbol{\chi}} = \mathbf{O} \tag{4.47}$$

where

$$\mathbf{f}^i \;=\; \mathcal{N}^i(\mathbf{F},\boldsymbol{\chi})\mathbf{e}^{l^i} + \frac{1}{l^i}\sum_{j=1,M} \mathcal{M}^{ij}(\mathbf{F},\boldsymbol{\chi})\mathbf{e}^{l^i l^j} \tag{4.48}$$

with $\mathcal{N}^i$ representing the axial force for ligament i and $\mathcal{M}^{ij}$ representing the bending moment between ligaments i and j. At ligament level $\mathcal{N}^i$ and $\mathcal{M}^{ij}$ depend on the current ligament length $l^i(\mathbf{F},\boldsymbol{\chi})$ and angle $\psi^{ij}(\mathbf{F},\boldsymbol{\chi})$ and come from the assumed potentials as described in Romero et al. (2008). $m_c\ddot{\boldsymbol{\chi}}$ represents the microinertia within each cell with the current acceleration of the cell vertex $\ddot{\boldsymbol{\chi}}_{n+1}$ given by

$$\ddot{\boldsymbol{\chi}}_{n+1} = \frac{\boldsymbol{\chi}_{n+1} - \boldsymbol{\chi}_n}{\Delta t^2} - \frac{\dot{\boldsymbol{\chi}}_n}{\Delta t} \tag{4.49}$$

The condition in Equation 4.47 provides the link between the continuum level affine field $\mathbf{F}$ and the cell level non-affine field $\boldsymbol{\chi}$ and allows us to univocally define the kinematic configuration of the cellular structure for an applied macroscopic deformation field. The specification of the global deformation $\mathbf{F}$ together with the history of motion of the cell vertex turns Equation 4.47 into a second order system of nonlinear ordinary differential equations for $\boldsymbol{\chi}$. Therefore, once a macroscopic deformation field $\mathbf{F}$ is prescribed, one can solve for the current configuration ($\boldsymbol{\chi}_{n+1}$) of each unit cell, by iterating utilizing the Taylor expansion of Equation 4.47 such as

$$\boldsymbol{\chi}_{n+1} = \boldsymbol{\chi}_n - \left[\frac{\partial \mathbf{R}}{\partial \boldsymbol{\chi}}\right]^{-1}\mathbf{R} \tag{4.50}$$

where

$$\frac{\partial \mathbf{R}}{\partial \boldsymbol{\chi}} = -\sum_{i=1,M}\left(\sum_{j=1,M}\frac{\partial \mathbf{f}^i}{\partial \mathbf{l}^j}\right) - \frac{m_c}{\Delta t^2}\mathbf{I} \tag{4.51}$$

as will be shown in Section 4.4.3.

4.4.2 Macroscopic Stress State

Once the unit cell equilibrium configuration $\boldsymbol{\chi}$ is determined for a globally specified field $\mathbf{F}$ through Equation 4.47, the First Piola-Kirchhoff stress tensor $\mathbf{P} = \tilde{\mathbf{P}}(\mathbf{F}(t))$

emerges as the derivative with respect to $\mathbf{F}$ and $\dot{\mathbf{F}}$ of the assumed *elastic* $\mathcal{W}(\mathbf{F})$ and *viscous* $\mathcal{D}(\dot{\mathbf{F}})$ potentials respectively, $P_{kK}(\mathbf{F}(t)) = \frac{\partial \mathcal{W}(\mathbf{F})}{\partial F_{kK}} + \frac{\partial \mathcal{D}(\dot{\mathbf{F}})}{\partial \dot{F}_{kK}}$. The resulting final expression is presented in Equation 4.52.

$$Stresses :\Rightarrow \mathbf{P} = \tilde{\mathbf{P}}(\mathbf{F}(t)) = \frac{1}{\mathcal{B}_o}\left[\sum_{i=1,M} \mathbf{f}^i \otimes \mathbf{L}^i - m_c \frac{\partial \boldsymbol{\chi}}{\partial \mathbf{F}} \cdot \ddot{\boldsymbol{\chi}}\right] \tag{4.52}$$

Notice that the constitutive relation in Equation 4.52 includes the microinertial stress $m_c \frac{\partial \boldsymbol{\chi}}{\partial \mathbf{F}} \cdot \ddot{\boldsymbol{\chi}}$ in addition to the stresses due to stretching and bending ($\mathbf{f}^i \otimes \mathbf{L}^i$) of the cell ligaments. We also point out that the constitutive relation for $\tilde{\mathbf{P}}(\mathbf{F})$ in Equation 4.52 satisfies the principle of frame indifference, namely $\tilde{\mathbf{P}}(\mathbf{F}) = \mathcal{R}^{*-\mathbf{1}}\tilde{\mathbf{P}}(\mathcal{R}^*\mathbf{F})$ where $\mathcal{R}^*$ represents a superposed rigid body motion.

4.4.3 Stress Tangents

In order to implement the derived constitutive relation $\mathbf{P} = \tilde{\mathbf{P}}(\mathbf{F}(t))$ into an implicit finite element analysis program, it is necessary to determine the consistent stress tangents. In the current problem the tangents take the following form

$$\frac{d\mathbf{P}}{d\mathbf{F}} = \frac{\partial \mathbf{P}}{\partial \mathbf{F}} + \frac{\partial \mathbf{P}}{\partial \boldsymbol{\chi}} \frac{\partial \boldsymbol{\chi}}{\partial \mathbf{F}} \tag{4.53}$$

Furthermore, since $\frac{\partial \boldsymbol{\chi}}{\partial \mathbf{F}}$ can be evaluated from 4.47,

$$\frac{\partial \mathbf{R}}{\partial \mathbf{F}} + \frac{\partial \mathbf{R}}{\partial \boldsymbol{\chi}} \frac{\partial \boldsymbol{\chi}}{\partial \mathbf{F}} = 0 \quad \Rightarrow \frac{\partial \boldsymbol{\chi}}{\partial \mathbf{F}} = -\left[\frac{\partial \mathbf{R}}{\partial \boldsymbol{\chi}}\right]^{-1} \frac{\partial \mathbf{R}}{\partial \mathbf{F}}, \tag{4.54}$$

the stress tangents defined in Equation 4.53 can be re-stated as

$$Tangents :\Rightarrow \frac{d\mathbf{P}}{d\mathbf{F}} = \frac{\partial \mathbf{P}}{\partial \mathbf{F}} - \frac{\partial \mathbf{P}}{\partial \boldsymbol{\chi}} \left[\frac{\partial \mathbf{R}}{\partial \boldsymbol{\chi}}\right]^{-1} \frac{\partial \mathbf{R}}{\partial \mathbf{F}}. \tag{4.55}$$

It's clear that the stress tangents in Equation 4.55 depend on the four partial derivatives $\frac{\partial \mathbf{R}}{\partial \boldsymbol{\chi}}$, $\frac{\partial \mathbf{R}}{\partial \mathbf{F}}$, $\frac{\partial \mathbf{P}}{\partial \boldsymbol{\chi}}$, and $\frac{\partial \mathbf{P}}{\partial \mathbf{F}}$. According to Equation 4.47 we can write

$$\frac{\partial \mathbf{R}}{\partial \boldsymbol{\chi}} = \sum_{i=1,M} \frac{\partial \mathbf{f}^i}{\partial \boldsymbol{\chi}} - \frac{\partial (m_c \ddot{\boldsymbol{\chi}})}{\partial \boldsymbol{\chi}} \tag{4.56}$$

and

$$\frac{\partial \mathbf{R}}{\partial \mathbf{F}} = \sum_{i=1,M} \frac{\partial \mathbf{f}^i}{\partial \mathbf{F}}. \tag{4.57}$$

Also, according to Equation 4.52 we can write

$$\frac{\partial \mathbf{P}}{\partial \boldsymbol{\chi}} = \frac{1}{\mathcal{B}_o}\left[\sum_{i=1,M} \frac{\partial \mathbf{f}^i}{\partial \boldsymbol{\chi}} \otimes \mathbf{L}^i - \frac{\partial \boldsymbol{\chi}}{\partial \mathbf{F}} \cdot \frac{\partial (m_c \ddot{\boldsymbol{\chi}})}{\partial \boldsymbol{\chi}}\right] \tag{4.58}$$

and

$$\frac{\partial \mathbf{P}}{\partial \mathbf{F}} = \frac{1}{\mathcal{B}_o} \sum_{i=1,M} \frac{\partial \mathbf{f}^i}{\partial \mathbf{F}} \otimes \mathbf{L}^i. \tag{4.59}$$

Observing 4.56, 4.57, 4.58, and 4.59 and recalling 4.54; we notice that the four partial derivatives depend on just three partial derivatives, namely $\frac{\partial \mathbf{f}^i}{\partial \boldsymbol{\chi}}$, $\frac{\partial \mathbf{f}^i}{\partial \mathbf{F}}$, and $\frac{\partial (m_c \ddot{\boldsymbol{\chi}})}{\partial \boldsymbol{\chi}}$. Using chain rule differentiation we can write

$$\frac{\partial \mathbf{f}^i}{\partial \boldsymbol{\chi}} = \sum_{k=1,M} \frac{\partial \mathbf{f}^i}{\partial \mathbf{l}^k} \frac{\partial \mathbf{l}^k}{\partial \boldsymbol{\chi}} \tag{4.60}$$

and

$$\frac{\partial \mathbf{f}^i}{\partial \mathbf{F}} = \sum_{k=1,M} \frac{\partial \mathbf{f}^i}{\partial \mathbf{l}^k} \frac{\partial \mathbf{l}^k}{\partial \mathbf{F}}. \tag{4.61}$$

and recalling Equation 4.49

$$\frac{\partial (m_c \ddot{\boldsymbol{\chi}})}{\partial \boldsymbol{\chi}} = \frac{m_c}{\Delta t^2}\mathbf{I} \quad or \quad m_c \frac{\partial \ddot{\chi}_\alpha}{\partial \chi_\beta} = \frac{m_c}{\Delta t^2}\delta_{\alpha\beta} \qquad where \;\; \alpha, \beta = 1 - 3 \tag{4.62}$$

Furthermore, based on Equation 4.46, the partial derivatives $\frac{\partial \mathbf{l}^k}{\partial \boldsymbol{\chi}}$ and $\frac{\partial \mathbf{l}^k}{\partial \mathbf{F}}$ can be written as

$$\frac{\partial \mathbf{l}^k}{\partial \boldsymbol{\chi}} = -\mathbf{I} \tag{4.63}$$

$$\frac{\partial \mathbf{l}^k}{\partial \mathbf{F}} = \mathbf{I} \otimes \mathbf{L}^k. \tag{4.64}$$

Now, we can simplify $\frac{\partial \mathbf{f}^i}{\partial \boldsymbol{\chi}}$ and $\frac{\partial \mathbf{f}^i}{\partial \mathbf{F}}$ as

$$\frac{\partial \mathbf{f}^i}{\partial \boldsymbol{\chi}} = -\sum_{k=1,M} \frac{\partial \mathbf{f}^i}{\partial \mathbf{l}^k} \tag{4.65}$$

$$\frac{\partial \mathbf{f}^i}{\partial \mathbf{F}} = \sum_{k=1,M} \frac{\partial \mathbf{f}^i}{\partial \mathbf{l}^k} \otimes \mathbf{L}^k. \tag{4.66}$$

It's clear that the two partial derivatives 4.65 and 4.66 only depend on one partial derivative, namely $\frac{\partial \mathbf{f}^i}{\partial \mathbf{l}^k}$. Now let's express everything in terms of $\frac{\partial \mathbf{f}^i}{\partial \mathbf{l}^k}$ explicitly.

$$\frac{\partial \mathbf{R}}{\partial \boldsymbol{\chi}} = -\sum_{i=1,M}\left(\sum_{j=1,M} \frac{\partial \mathbf{f}^i}{\partial \mathbf{l}^j}\right) - \frac{m_c}{\Delta t^2}\mathbf{I} \tag{4.67}$$

$$\frac{\partial \mathbf{R}}{\partial \mathbf{F}} = \sum_{i=1,M}\left[\sum_{j=1,M}\left(\frac{\partial \mathbf{f}^i}{\partial \mathbf{l}^j}\otimes \mathbf{L}^j\right)\right] \tag{4.68}$$

$$\frac{\partial \mathbf{P}}{\partial \boldsymbol{\chi}} = -\frac{1}{\mathcal{B}_o}\left[\sum_{i=1,M}\left(\sum_{j=1,M}\frac{\partial \mathbf{f}^i}{\partial \mathbf{l}^j}\right)\otimes \mathbf{L}^i + \frac{m_c}{\Delta t^2}\frac{\partial \boldsymbol{\chi}}{\partial \mathbf{F}}\cdot \mathbf{I}\right] \tag{4.69}$$

$$\frac{\partial \mathbf{P}}{\partial \mathbf{F}} = \frac{1}{\mathcal{B}_o}\left[\sum_{i=1,M}\sum_{j=1,M}\left(\frac{\partial \mathbf{f}^i}{\partial \mathbf{l}^j}\otimes \mathbf{L}^j\right)\otimes \mathbf{L}^i\right] \tag{4.70}$$

The four tensor expressions in Equations 4.67 - 4.70 above define the necessary stress tangents according to Equation 4.55. By defining two tensor as

$$\mathbf{S}_1^i = \sum_{j=1,M}\frac{\partial \mathbf{f}^i}{\partial \mathbf{l}^j} \tag{4.71}$$

$$\mathbf{S}_2^i = \sum_{j=1,M}\left(\frac{\partial \mathbf{f}^i}{\partial \mathbf{l}^j}\otimes \mathbf{L}^j\right), \tag{4.72}$$

the four partial derivatives in Equations 4.67 - 4.70 can be stated more concisely as

$$\frac{\partial \mathbf{R}}{\partial \boldsymbol{\chi}} = -\sum_{i=i,M}\mathbf{S}_1^i - \frac{m_c}{\Delta t^2}\mathbf{I} \tag{4.73}$$

$$\frac{\partial \mathbf{R}}{\partial \mathbf{F}} = \sum_{i=1,M}\mathbf{S}_2^i \tag{4.74}$$

$$\frac{\partial \mathbf{P}}{\partial \boldsymbol{\chi}} = -\frac{1}{\mathcal{B}_o}\left[\sum_{i=1,M}\left(\mathbf{S}_1^i\otimes \mathbf{L}^i\right) + \frac{m_c}{\Delta t^2}\frac{\partial \boldsymbol{\chi}}{\partial \mathbf{F}}\cdot \mathbf{I}\right] \tag{4.75}$$

$$\frac{\partial \mathbf{P}}{\partial \mathbf{F}} = \frac{1}{\mathcal{B}_o}\sum_{i=1,M}\left(\mathbf{S}_2^i\otimes \mathbf{L}^i\right). \tag{4.76}$$

4.4.4 Numerical Notation

Consider a four ligament unit cell ($M = 4$) and let's define arrays to store data in the form of $dfdl(3,3,4,4)$ and cL(3,4) such that

$$\frac{\partial \mathbf{f}^i}{\partial \mathbf{l}^j} = \frac{\partial f_m^i}{\partial l_n^j} \Rightarrow dfdl(m,n,j,i) \tag{4.77}$$

$$\mathbf{L}^j = L_k^j \Rightarrow cL(k,j) \tag{4.78}$$

where m, n, k = 1-3 and i, j = 1-4 . It follows that the arrays storing $\mathbf{S}_1^i$ and $\mathbf{S}_2^i$ can be defined as

$$\mathbf{S}_1^i = S_{1mn}^i = \sum_{j=1,4}\frac{\partial f_m^i}{\partial l_n^j} \Rightarrow S_1(m,n,i) = \sum_{j=1,4} dfdl(m,n,j,i) \tag{4.79}$$

$$\mathbf{S}_2^i = S_{2lmn}^i = \sum_{j=1,4} \frac{\partial f_l^i}{\partial l_m^j} L_n^j \Rightarrow S_2(l,m,n,i) = \sum_{j=1,4} dfdl(l,m,j,i) \cdot cL(n,j) \quad (4.80)$$

where l, m, n = 1-3 and i = 1-4 . Similarly the arrays for storing the four partial derivatives $\frac{\partial \mathbf{R}}{\partial \boldsymbol{\chi}}$, $\frac{\partial \mathbf{R}}{\partial \mathbf{F}}$, $\frac{\partial \mathbf{P}}{\partial \boldsymbol{\chi}}$, and $\frac{\partial \mathbf{P}}{\partial \mathbf{F}}$ are defined as

$$\frac{\partial \mathbf{R}}{\partial \boldsymbol{\chi}} = \frac{\partial R_m}{\partial \chi_n} \Rightarrow dRdu(m,n) = -\sum_{i=1,4} S_1(m,n,i) - \frac{m_c}{\Delta t^2}\delta_{mn} \quad (4.81)$$

$$\frac{\partial \mathbf{R}}{\partial \mathbf{F}} = \frac{\partial R_l}{\partial F_{mn}} \Rightarrow dRdF(l,m,n) = \sum_{i=1,4} S_2(l,m,n,i) \quad (4.82)$$

$$\frac{\partial \mathbf{P}}{\partial \boldsymbol{\chi}} = \frac{\partial P_{lm}}{\partial \chi_n} \Rightarrow dPdu(l,m,n) = -\frac{1}{\mathcal{B}_o} \sum_{i=1,4} S_1(l,n,i) \cdot cL(m,i) \quad (4.83)$$

$$-\frac{\partial \chi_n}{\partial F_{lm}} \frac{m_c}{\Delta t^2}\delta_{mn}$$

$$\frac{\partial \mathbf{P}}{\partial \mathbf{F}} = \frac{\partial P_{lm}}{\partial F_{nk}} \Rightarrow dPdF(l,m,n,k) = \frac{1}{\mathcal{B}_o} \sum_{i=1,4} S_2(l,n,k,i) \cdot cL(m,i) \quad (4.84)$$

where l, m, n, k = 1-3. To make sense of the dimensions of the arrays above, it is beneficial to write down the derivatives in component form.

$$\frac{\partial R_m}{\partial \chi_n} = \sum_{i=1,4} \frac{\partial f_m^i}{\partial \chi_n} = -\sum_{i=1,4}\sum_{j=1,4} \frac{\partial f_m^i}{\partial l_n^j} = -\sum_{i=1,4} S_{1mn}^i$$

$$\Rightarrow \quad dRdu(m,n) = -\sum_{i=1,4} S_1(m,n,i) \quad (4.85)$$

$$\frac{\partial R_l}{\partial F_{mn}} = \sum_{i=1,4} \frac{\partial f_l^i}{\partial F_{mn}} = \sum_{i=1,4}\sum_{j=1,4} \frac{\partial f_l^i}{\partial l_m^j} L_n^j = \sum_{i=1,4} S_{2lmn}^i$$

$$\Rightarrow \quad dRdF(l,m,n) = \sum_{i=1,4} S_2(l,m,n,i) \quad (4.86)$$

$$\frac{\partial P_{lm}}{\partial \chi_n} = -\frac{1}{\mathcal{B}_o} \sum_{i=1,4} \frac{\partial f_l^i}{\partial \chi_n} L_m^i = -\frac{1}{\mathcal{B}_o} \sum_{i=1,4} \left(\sum_{j=1,4} \frac{\partial f_l^i}{\partial l_n^j} \right) L_m^i = -\frac{1}{\mathcal{B}_o} \sum_{i=1,4} S_{1ln}^i L_m^i$$

$$\Rightarrow \quad dPdu(l,m,n) = -\frac{1}{\mathcal{B}_o} \sum_{i=1,4} S_1(l,n,i) \cdot cL(m,i) \quad (4.87)$$

$$\frac{\partial P_{lm}}{\partial F_{nk}} = \frac{1}{\mathcal{B}_o} \sum_{i=1,4} \frac{\partial f_l^i}{\partial F_{nk}} L_m^i = \frac{1}{\mathcal{B}_o} \sum_{i=1,4} \left(\sum_{j=1,4} \frac{\partial f_l^i}{\partial l_n^j} L_k^j \right) L_m^i = \frac{1}{\mathcal{B}_o} \sum_{i=1,4} S_{2lnk}^i L_m^i$$

$$\Rightarrow \quad dPdF(l,m,n,k) = \frac{1}{\mathcal{B}_o} \sum_{i=1,4} S_2(l,n,k,i) \cdot cL(m,i) \quad (4.88)$$

4.5 Predictions

This section presents the implementation of the formulation in Section 2.3 as a constitutive update within the framework of nonlinear finite element analysis(FEA) schemes. The results presented here were obtained using an in-house implicit Nonlinear Finite Element Analysis (FEA) code. The stress tangents needed in any implicit FEA simulation are those formulated in Section 4.4.3. The simulations serve as an example of how the micromechanical open-cell foam constitutive law, Equation 2.77, formulated in Section 2.3 of Chapter 2 can be implemented as a constitutive update into a nonlinear implicit finite element analysis program to simulate the response of dynamically loaded polymeric (visco-elastic) and metallic (elasto-plastic) open-cell foam specimen. In order to use the derived constitutive law (Equation 2.77) to simulate the mechanical response of a foam specimen, first we assume that the size of the specimen is much larger than the size of the individual cells which compose it. Then, we assume a separation of scales where the response of any point on the sample when viewed from a global (macroscopic) perspective is obtained from the local (microscopic) model of the cellular structure described in Section 2.3. This is a multiscale simulation where the overall response of the foam material is obtained from a finite element analysis simulation which obtains the response at each node in the mesh from a lower scale micromechanical simulation of the cells. The micromechanical unit cell model in turn requires a third model which predicts the axial and bending constitutive behavior of the ligaments composing each unit cell.

4.5.1 Polymeric Visco-Elastic Foam Predictions

This section presents the finite element analysis simulations for polymeric foams with decoupled visco-elastic behavior at cell wall level. Figure 4.4a shows a schematic of the geometry of the sample and the boundary and initial conditions. The simulation mimics a $2D$ cuboid sample under plane strain conditions dynamically compressed at constant velocity from the top surface. Figure 4.4b shows the recorded stress at the top surface as a function of the average vertical strain. The stress-strain signature in

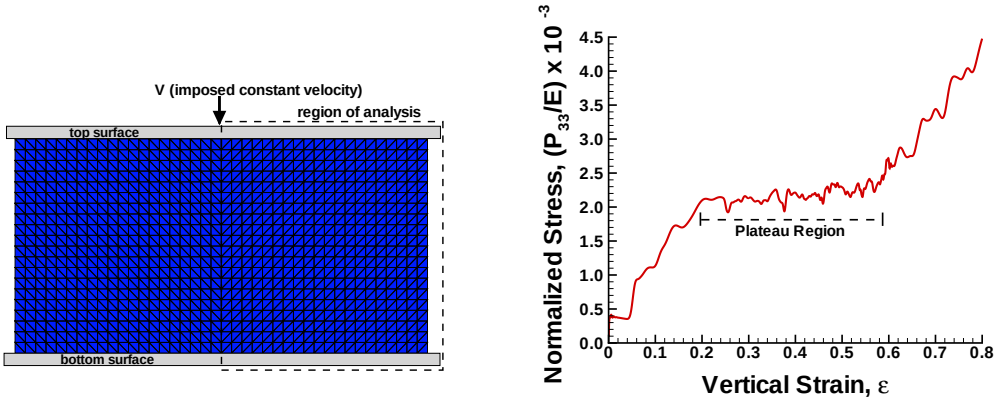

(a) Initial Specimen State

(b) Top Surface Response

Figure 4.4: Simulation of impact at a constant downward velocity of $v = 10.0\frac{m}{s}$ on a visco-elastic foam material. The foam is homogeneous and composed of the unit cell described in the section 2.4.1. The foam density was taken as $\rho = 75.0\ \frac{Kg}{m^3}$ and the ligaments of every cell in the microstructure had the properties: ligament Young's Modulus $(E) = 7.5 \times 10^8$ Pa, ligament viscosity $(\eta) = 10.0\ \frac{N \cdot s}{m^2}$, ligament radius $(r) = 0.3\ mm$, ligament length $(L) = 1.0\ mm$. (a) Visco-elastic foam specimen in its initial state along with the region selected for finite element analysis. (b) Vertical Piola Stress P_{33} normalized by the Young's Modulus (E) vs. vertical strain ϵ_{yy} response evaluated at the top surface.

Figure 4.4b clearly shows the strain (or displacement) interval where collapse (configurational transformation) occurred. The details of the transformation process can be studied by inspecting snapshots at different times or strain levels during the loading process.

Nine snapshots taken at different strains or times are shown in Figure 4.5. Three clearly different stages are observed during the evolution of the deformation. In the small deformation regime with average deformation up to approximately 20% all the material remains in the original stable configuration without cell collapse. This process can be observed in the first two snapshots (Strain = 4% and 15%) shown in Figure 4.5 where the deformation remains nearly homogeneous throughout the entire specimen. Any small variations are due to disturbance from the boundaries and dynamic effects such as wave propagation.

As can be observed from Figures 4.5c -4.5h, during the intermediate deformation regime with average strain between 20% to 60%, the deformation pattern is consistent with materials exhibiting phase transformation behavior such as foams. The common plateau response of foam materials during the collapse process is captured by the model

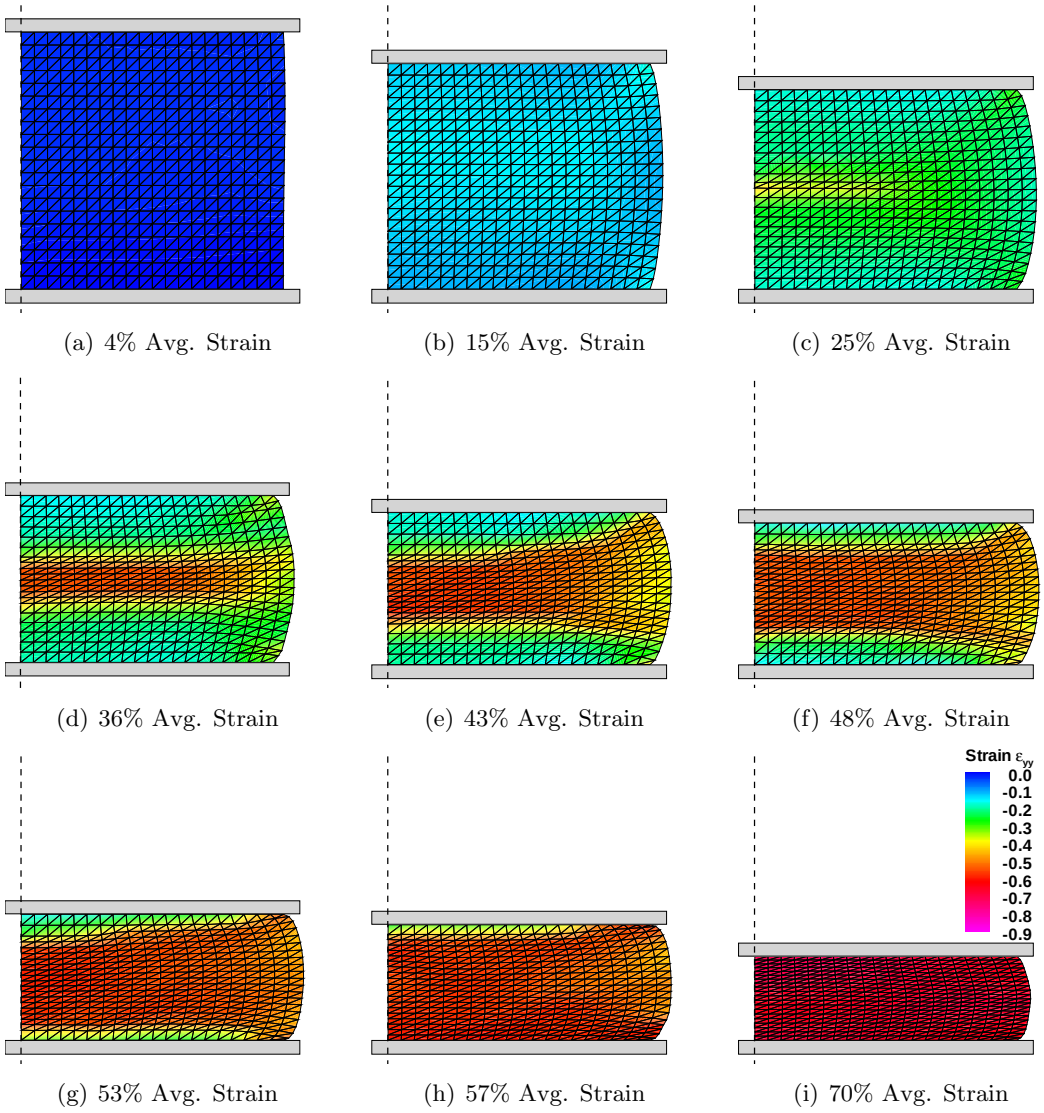

(a) 4% Avg. Strain (b) 15% Avg. Strain (c) 25% Avg. Strain

(d) 36% Avg. Strain (e) 43% Avg. Strain (f) 48% Avg. Strain

(g) 53% Avg. Strain (h) 57% Avg. Strain (i) 70% Avg. Strain

Figure 4.5: Snapshot taken at different times corresponding to different average vertical strains during the dynamic compression of the 2D visco-elastic foam sample described in Figure 4.4. Colors represent the local deformation in the vertical direction. The black lines describe the FEM mesh, not the lattice. The snapshots clearly show the transition from (nearly) homogeneous deformation to heterogeneous deformation (mixture of collapsed and un-collapsed phases) and back to nearly homogeneous (completely collapsed) phase.

as shown in Figure 4.4b. During this deformation regime there is a spatial distribution of two phases (collapsed and un-collapsed regions) which minimize the energy of the system. As shown in Figures 4.5c -4.5h, the deformation process evolves by the gradual transformation of the un-collapsed phase (which initially has the larger volume) into the collapsed phase (which initially has the smaller volume). This process is clearly observed from Figures 4.5c -4.5h, where the snapshots were taken at times with strain 25%, 36%, 43%, 48%, 53%, and 57%.

The transformed phase (red region) starts in the middle due to stress concentration effects (Strain = 25%), propagates as a band towards the edges (Strain = 36%), continues to thicken in the interior (Strain = 43%), propagates as a thick band towards the top and bottom (Strain = 48% and Strain = 53%) and eventually reaches the lower surface (Strain = 57%), leaving a small region (green) without transforming next to the top surface in contact with the support plate. While the general behavior is similar to plasticity, the process is quite different. In this case there is a co-existence of two phases, each one with characteristic deformation associated with λ^+ and λ^- which are the deformation at the initiation of collapse and at the termination of collapse respectively. Locally, λ^+ and λ^- are defined by the two strain values defining the interval of non-convex energy during the deformation of the unit cell as shown by the red curve in Figure A.1b in appendix A. In the large deformation regime with average deformation above 60%, all the material has transformed into the collapsed phase as indicated in the last snapshot in Figure 4.5 (Strain = 70%). The deformation is again homogeneous across the specimen after complete collapse throughout. As can be observed from Figure 4.4b, the increased stiffness exhibited by foam materials when the whole sample has been transformed into the collapsed phase is captured by the current model.

In the Chapter 2, we study the effects of strain rate on the response of dynamically loaded open-cell foams based solely on the local micromechanical model derived in Section 2.3 and a Maxwell construction of the effective foam response. It is also worth noting that the local strain rate throughout the foam specimen is actually nonuniform while the foam system is undergoing collapse. Figure 4.6 shows snapshots at different average vertical strains of the variation of the local vertical strain rate through the foam

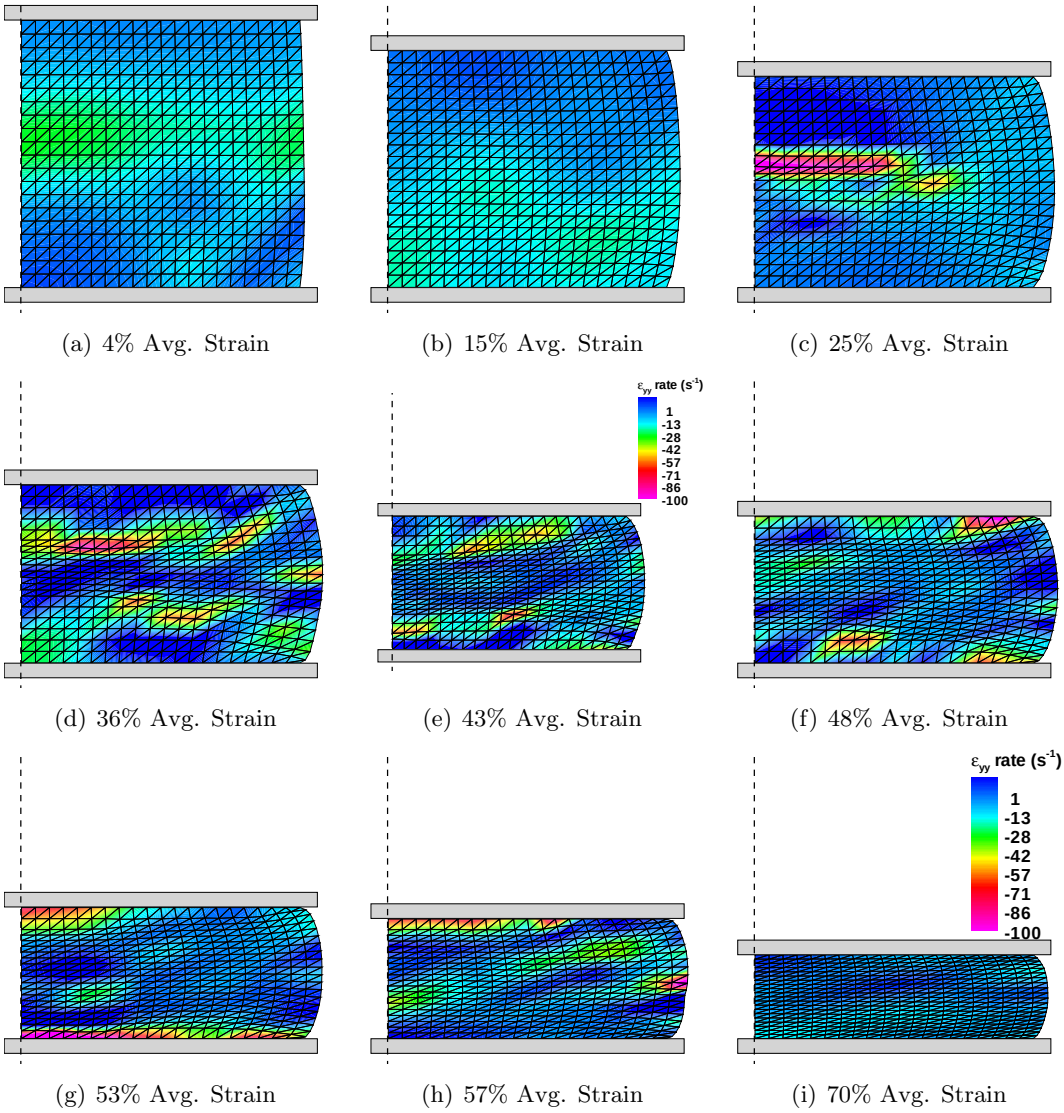

(a) 4% Avg. Strain (b) 15% Avg. Strain (c) 25% Avg. Strain

(d) 36% Avg. Strain (e) 43% Avg. Strain (f) 48% Avg. Strain

(g) 53% Avg. Strain (h) 57% Avg. Strain (i) 70% Avg. Strain

Figure 4.6: Snapshots taken at different times corresponding to different average vertical strains during the dynamic compression of the 2D visco-elastic foam sample described in Figure 4.4. Colors represent the local strain rate in the vertical direction. The black lines describe the FEM mesh, not the lattice. The snapshots show the variation of the local strain vertical strain rate throughout the foam specimen as it is being loaded with a constant downward velocity at the top surface. The snapshots clearly show the variation of the strain rate before collapse, during collapse and after collapse.

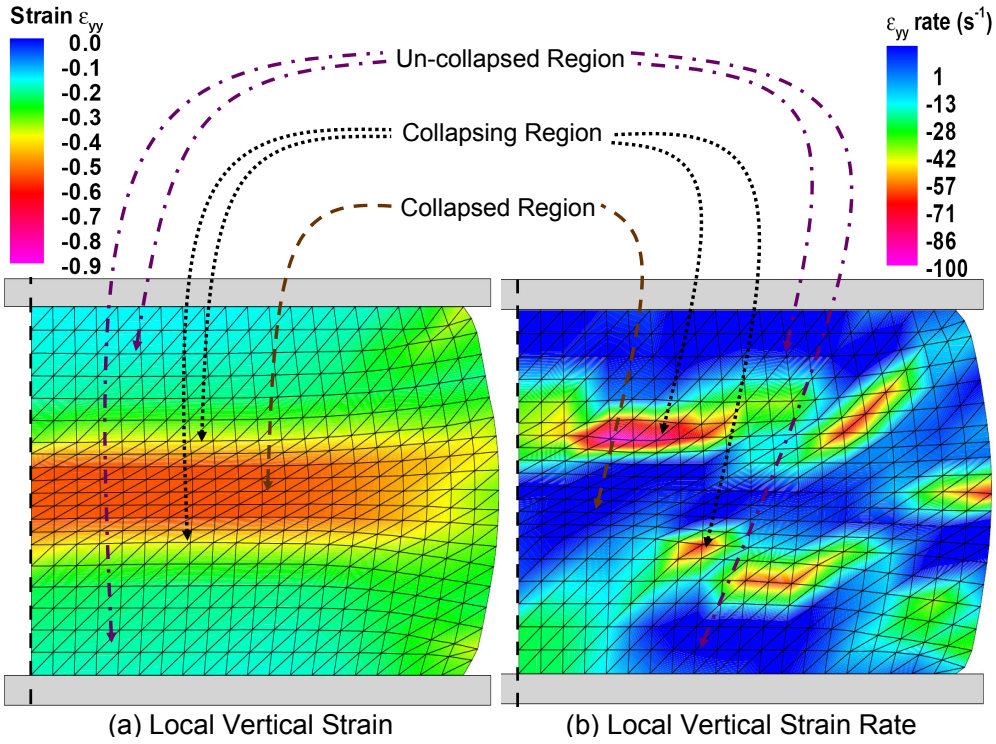

Figure 4.7: Comparison of the strain and strain rate for the 36% average vertical strain snapshots in Figures 4.5d and 4.6d. (a) Variation of the local vertical strain. (b)Variation of the local vertical strain rate.

material for the FEM simulation presented in Figures 4.4 and 4.5. As can be observed from Figures 4.6a and 4.6b, the strain rate is approximately uniform before the materials starts to collapse and any small variations are due wave propagation. Figures 4.6c - 4.6h show the variation of the strain rate while the cellular structure is undergoing collapse. As can be observed from Figures 4.6c - 4.6h, once collapse initiates, the local strain rate is very heterogeneous throughout the material. The strain rate is highest for regions of the material which are currently undergoing collapse as captured by the yellow and red portions in Figures 4.6c - 4.6h. Once a certain region of material finishes collapsing, the strain rate for that region returns to a lower value corresponding to blue and green in Figures 4.6c - 4.6h. Once the whole material is done collapsing, the strain rate once again becomes approximately uniform through the material as shown in Figure 4.6i.

Figure 4.7 shows a more detailed description of the variation of the local vertical

strain and strain rate while the foam system is undergoing collapse for example at 36% average vertical strain. Comparison of Figures 4.7a and 4.7b clearly indicates that the local strain rate is highest at the interface between collapsed and un-collapsed regions which are the regions currently undergoing collapse. The regions currently undergoing collapse are highlighted by the higher strain rate regions marked with red in Figure 4.7b. Figure 4.7 also points out that the strain rate is lowest in both the collapsed and non-collapsed region.

4.5.2 Metallic Elasto-Plastic Foam Predictions

Here we present the Finite Element Modeling simulations for metallic open-cell foams with coupled elasto-plastic constitutive behavior at cell wall level. During the FEA simulations, the microscopic unit cell model reviewed in Section 4.4 provides the stress response at every node in the mesh while the stress tangents formulated in Section 4.4.3 allow the simulation to march in time. Keep in mind that the micromechanical unit cell in turn obtains the necessary forces and moments from the strut axial and bending constitutive models described in Chapter 3. The simulations provides a coherent description of the metallic foam material from specimen level to unit cell level to strut level.

The images shown in Fig. 4.8 and Fig. 4.8 are snapshots taken at different average vertical strains during dynamic compression of a $2D$ specimen a constant downward velocity of $10m/s$. Fig. 4.8 presents the evolution of the local vertical deformation for open-cell foams with a *high initial yield stress* which reduces the amount of plastic deformation during compression of the foam specimen. Fig. 4.9 on the other hand presents the evolution of the local vertical strain for the case of *low initial yield stress* which results in a high amount of plastic deformation during compression of the specimen. This prediction clearly shows how the system undergoes heterogeneous deformation during collapse of the cells in the system.

Fig. 4.8 and Fig. 4.9 clearly show that the model captures the experimentally observed heterogeneous deformation through localized collapse bands. First, in Figs. 4.8a - 4.8c and Figs. 4.9a - 4.9b the cellular microstructure has not yet collapsed and the

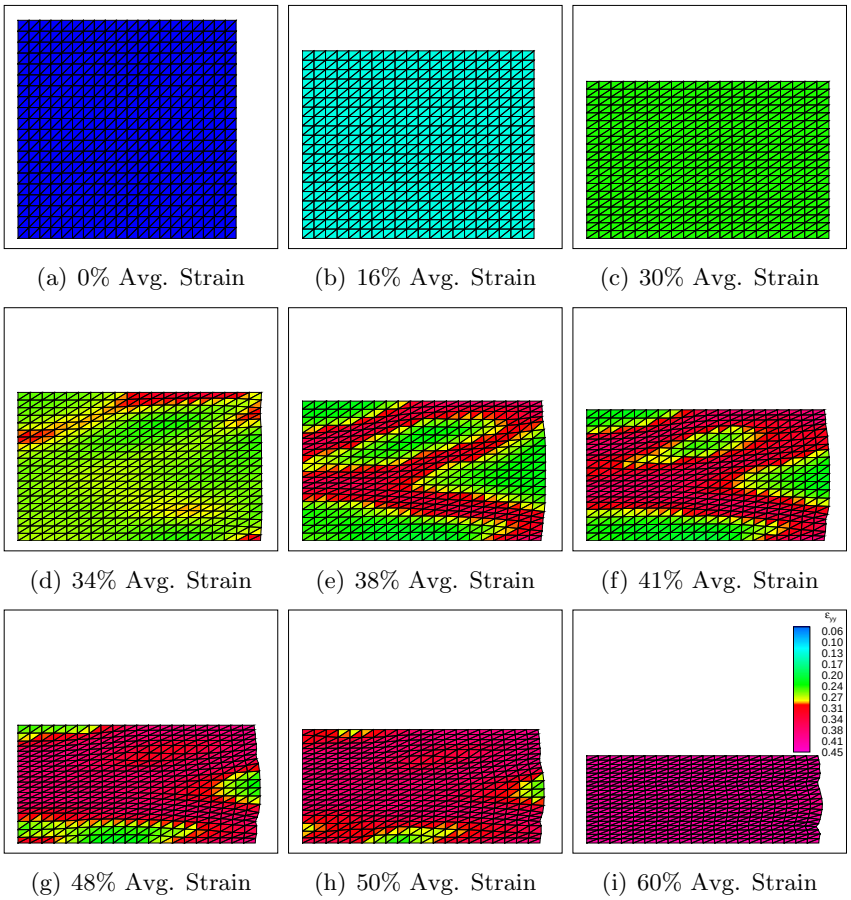

(a) 0% Avg. Strain (b) 16% Avg. Strain (c) 30% Avg. Strain

(d) 34% Avg. Strain (e) 38% Avg. Strain (f) 41% Avg. Strain

(g) 48% Avg. Strain (h) 50% Avg. Strain (i) 60% Avg. Strain

Figure 4.8: Simulation of impact at a constant downward velocity of $v = 10.0m/s$ on a homogeneous *elasto-plastic* 2D open-cell foam specimen with a *high initial yield stress* resulting in a small amount of plastic deformation. The snapshots were taken at different times corresponding to different average vertical strains during the dynamic compression. Colors represent the local deformation in the vertical direction and the black lines describe the FEM mesh. The snapshots clearly demonstrate the transition from (nearly) homogeneous deformation to heterogeneous deformation (mixture of collapsed and uncollapsed regions) and back to nearly homogeneous (completely collapsed) deformation.

material is undergoing uniform deformation. Next, in Figs. 4.8d - 4.8h and Figs. 4.9c - 4.9h the cellular microstructure is collapsing and the material is undergoing heterogeneous deformation. Finally, in Fig. 4.8i and Fig. 4.9i the cellular microstructure has collapsed completely and the material is again undergoing uniform compaction deformation. Overall the formulation agrees well with the main conclusions of the experimental studies capturing the different characteristic of foam response, namely initial homogeneous, heterogeneous collapse and homogeneous compaction.

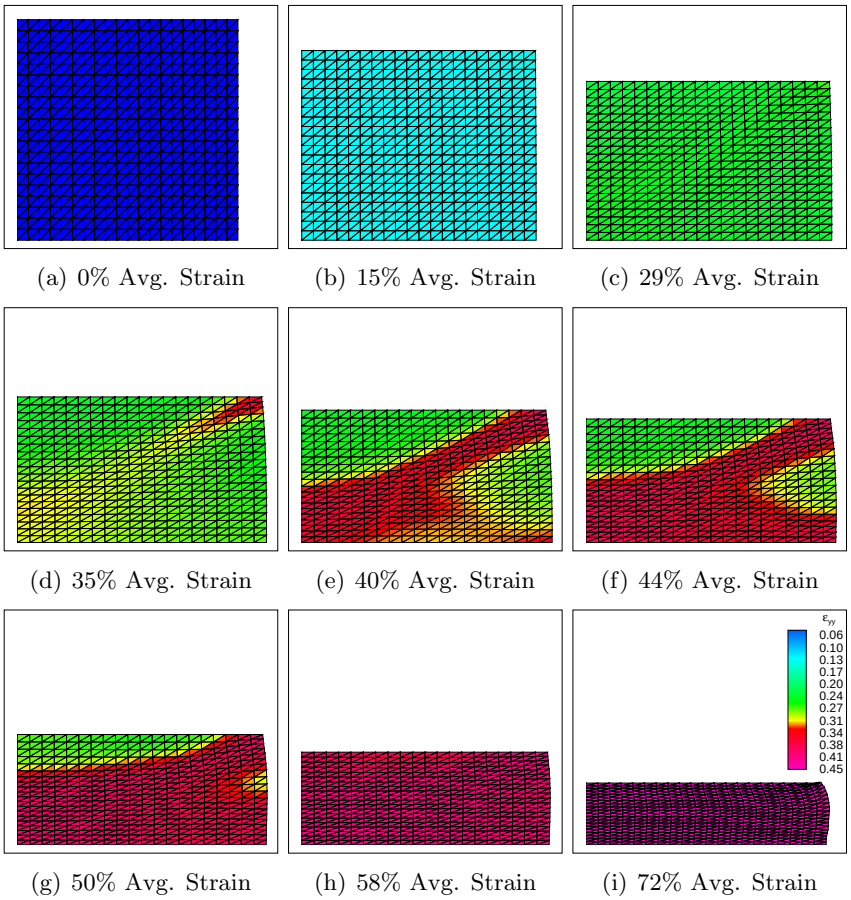

(a) 0% Avg. Strain (b) 15% Avg. Strain (c) 29% Avg. Strain

(d) 35% Avg. Strain (e) 40% Avg. Strain (f) 44% Avg. Strain

(g) 50% Avg. Strain (h) 58% Avg. Strain (i) 72% Avg. Strain

Figure 4.9: Simulation of impact at a constant downward velocity of $v = 10.0m/s$ on a homogeneous *elasto-plastic* 2D open-cell foam specimen with a *low initial yield stress* resulting in a large amount of plastic deformation. The snapshot were taken at different times corresponding to different average vertical strains during the dynamic compression. Colors represent the local deformation in the vertical direction and the black lines describe the FEM mesh. The snapshots clearly demonstrate the transition from (nearly) homogeneous deformation to heterogeneous deformation (mixture of collapsed and uncollapsed regions) and back to nearly homogeneous (completely collapsed) deformation.

4.6 Conclusions

As demonstrated in this chapter, the theory formulated in Chapter 2 provides a continuum-level constitutive formulation for lightweight, open-celled foams based on clear and quantifiable parameters such as microstructural topology and ligament properties while capturing the effects of dynamic loading via viscous dissipation at ligament level and microinertia at unit cell level. The model captures the successive collapse process of the unit cells through relocation of the unit cell vertex and reorientation of the ligaments while evaluating the axial and bending deformation of the ligaments composing

the unit cell level. History of deformation is considered at ligament level and used to predict the succeeding cell wall axial and bending constitutive response. As shown, the derived constitutive relation is readily implementable in the realm of nonlinear implicit and implicit finite element analysis FEA schemes. In the specimen level simulations the FEA scheme obtains the response at every node in the mesh from the micromechanical open-cell foam model which in turn requires constitutive models for the axial and bending cell wall constitutive behavior.

In the simulations, the deformation pattern of constrained cuboidal foam samples subjected to uniaxial compression is followed utilizing an implicit FEA dynamic formulation. The predictions are in good agreement with the experimental observations, revealing the typical deformation stages of foam materials. Specifically, the resulting macroscopic FEA simulations clearly capture all the typical stages of deformation observed during dynamic compression of foams materials. Namely, the typical initial homogeneous deformation region, the collapse region with localized heterogenous deformation, and the homogeneous densification region in addition to the effective wave propagation due to dynamic loads. While the outlined procedure can be utilized for a more general class of unit cells, we limited the presented results to cells containing 4 ligaments concurring into one internal vertex. The present unit cell model assumed that the ligaments remain straight after buckling to ease the computational burden however this restriction could be removed in future improvements of the model. Additionally, the visco-elastic and the elasto-plastic constitutive cell wall behavior for polymeric and metallic foams respectively are just two examples of the type of constitutive behavior that can be implemented. Other relations for visco-elasto or elasto-plastic or elasto-brittle constitutive behavior could be implemented in the future.

Chapter 5

Conclusions and Future Work

5.1 Summary

Cellular materials such as metallic and polymeric foams are multi-phase materials that have structure, geometry, density, viscosity, and elasticity properties with no clear understanding about how these different properties effect the dynamic behavior separately or coupled. The modeling work presented here aids in understanding the connection between the complex mechanical response exhibited by foam materials during dynamics loading and the diverse cellular characteristic and distinct materials properties found in these materials. The developed model could be used by engineers and scientist looking to develop the next generation of multi-functional, multi-property materials such as metallic and polymeric foams. The present development has the potential to simulate a wide array of material systems exhibiting a cellular structure. Different mechanics have been incorporated to account for very different potential scenarios. From viscoelastic systems such as polymeric foams to brittle systems such ceramic foams to plastic systems such as Metallic Foams. With minor alterations, the formulated model could be used to study different types of foam systems with diverse cellular structures and varying cell wall material properties.

The model presented here evolved from the earlier work reported in Wang and Cuitiño (2000) and conducted under the direction of prof. Alberto M. Cuitiño. The previously developed numerical model for the analysis of statically loaded, open-cell, hyperelastic foam systems was enhanced with the capability to analyze dynamically loaded, visco-elastic (polymeric) and elasto-plastic (metallic) open-cell foam systems because many current and future applications of foam materials are or will take place under dynamic loading environments where the loading occurs at very high, impact

type strain rates. The enhanced model takes into account the effects of the cell wall material properties, dimensions of the solid cell walls, and inertial motion of the cells which in turn facilitates one to investigate the effects of density, viscosity, elasticity and plasticity of the small bars making up every unit cell in the cellular structure. First, the micromechanical formulation is resolved numerically and used to predict the effective response of different foams. The formulation is then implemented as a constitutive update into implicit and explicit finite element analysis schemes to predict the full field response. The resulting FEM simulations capture the localized collapse behavior and the variation of the local strain rate due to unstable cell collapse.

5.2 Conclusions

As long as we stay in the range of cellular solids without increasing the relative density of the cellular solid to the point that one is looking at a porous material instead of a foam system, the predictions by the presented model make sense physically and support the experimentally observed deformation patterns for dynamically loaded cellular solids. The mechanical behavior of solid foams is a complex, nonlinear process where the cellular microstructure and the cell-wall material properties dictate the response in a coupled manner. The deformation process can involve elasticity, plasticity, fracture, viscosity, temperature effects, strain rate effects, density (microinertia), unstable collapse etc. Experimentally it is extremely difficult to investigate the different effects separately, however through the current model, we can afford to look at effect separately. For instance, Almost all the experimental studies on dynamically loaded solid foam systems point out that as the strain rate increases the yield and collapse strength increases. This conclusion is also reached by the current model in the case of both visco-elastic and visco-elastic foams but the model is able to give reasons for this increase such as viscous and inertial effects going on inside the microstructure.

Experimental studies on dynamically loaded foams systems conclude that as the density of a cellular material is increased the collapse strength increases. We also make this conclusion and point out the reasons for this increase in strength is an increased in inertial force. When the cellular solid is dynamically loaded the increase in mass due

to higher density results in larger inertial forces inside the cellular material resulting in a stronger response from the foam material as observed experimentally. Cellular solids also exhibit higher strengths during dynamic loading if the relative density is increased. This can also be understood in term of inertial effects according the present model. For a given bulk solid density, changing the cell dimensions (same as changing the relative density) in a foam system has the same effect as increasing the bulk solid density. If the dimensions such as the thickness or length of bars in a cell are changed, the collapse stress will change. If the cell leg thickness such as the radius increases or if the cell leg length decreases, the collapse strength increases because a bigger inertial force results inside the material with such cell dimension changes. The opposite will happen if the dimensions are changed by decreasing the cell leg radius and increasing the cell leg length.

It has been shown that increasing the viscosity in a foam system by increasing the viscosity of the surrounding fluid also increases the strength response during dynamic loading. This effect is also understood via the current model. The current visco-elastic version of the model is able to the viscous response of the solid phase and it is also able to superimpose an additional response from a filler material. The viscous property of a material exerts a dissipative, friction force against the motion or deformation in the material. The effects of solid phase viscosity on dynamically loaded solid foam systems have not been investigated experimentally because it is difficult to measure the viscosity of the solid cell wall material. The current model predicts that as the viscosity of the solid cell wall material increases the strength of the dynamically loaded cellular solid increases including an increase in collapse strength. Increasing the viscosity of the fluid inside the microstructure should have a similar effect as increasing the solid cell wall material viscosity.

In the metallic version of the model the viscous effects are coupled with the elastic effects in the local relations therefore we must look at the viscous effects in metallic foams through the initial yield stress and the initial rate of plastic deformation. As expected increasing the initial value of the yield stress which a way to increase the cell wall material viscosity, increases the collapse strength of the metallic foam. Similarly

decreasing the initial rate of plastic deformation which essentially increases the cell wall material viscosity, causes an increase in the collapse strength of metallic foams during dynamic loading. The elasto-plastic model maintains the history of plastic deformation at strut level to use in predicting the succeeding strut constitutive response based on the Young's Modulus, initial yield stress, initial rate of plastic deformation, hardening power law exponent, rate of plastic deformation power law exponent and strut cross sectional area and moment of inertia. The model is able to gage the effects of loading rate through the elasticity and viscosity of the solid cell wall materials.

The micromechanical visco-elastic and elasto-plastic alone provide effective responses in a numerically efficient manner allowing the user to probe a wide range of properties in a short amount of time. However in order to predict the full range full field response through an open-cell foam specimen, it is necessary to implement the micromechanical model as a constitutive update into nonlinear finite element analysis schemes. The FEM predicted response captures the experimental signature response of open-cell foams observed during compressive loading. The FEM simulation nicely capture the different stages of deformation (initial homogeneous, heterogenous collapse, and homogeneous compaction) during compression of polymeric and metallic open-cell foams. The simulations clearly capture the heterogeneous bands of deformation during collapse of dynamically compressed visco-elastic and elasto-plastic open-cell foams. Finally, the FEM simulations also capture the heterogeneity of the local strain rate during collapse of the open-cell foams.

Solid open-cell foams such as the one that has been modeled here have great material properties which can be put to use in many different applications. However, it is more important to emphasize that cellular solids are materials which contain great combinations of material properties such as high strengths and low density, good sound absorption and thermal stability, great energy absorption ability at low stress levels etc. It is through this extraordinary combinations of properties that cellular solids offer the greatest potential for applications Korner and Singer (2000). Nowadays, we usually need to satisfy more than one property in a certain material application, it's here that we see the advantages of materials with great combinations of properties such

as cellular solids. Models such as the one presented here can provide industry in the cellular materials field with great insights on how the low level material properties of cellular solids affect the mechanical behavior. This could be used as a tool to decide on the properties of the liquid that will be used to form the cell walls of the foam system or to tell us how to guide and control the foaming process to obtain desired densities, viscosities, cell wall dimensions, strength etc. The present model is very general and eventually will have the ability to simulate all the different types of foam systems in different loading scenarios.

5.3 Recommendations and Future Work

The work presented here could enhanced or expanded by considering varied cellular geometries, distinct constitutive local relations, accelerating impact loads, careful treatment of the fluid flow around the cellular structure, high temperature environments, and developing similar ideas for dynamically loaded closed-cell foams. The model presented here is applicable to foams which can be mimicked by a homogeneous cellular structure but the model can be extended to foam with cell size distributions by considering a Taylor averaging approach as done in Cuitiño and Zheng (2003). The current model could also be enhanced by adding ligament bending away form the unit cell vertex by considering vertex rotation in present formulation. The formulation was derived for open-cell foams which can be considered as being composed of bars with circular cross sections however considering ligaments with different cross sectional areas such as squares, rectangles or triangles will result in drastically different problems because it has been show that the ligament shape (specific microstructure) can have a very strong effect on the measured response. Currently the structural problem at cell level is being considered as a decoupled system with moment equilibrium automatically satisfied since it is limited to the cell vertex. A different problem could be analyzed by considering the coupled bending and axial problem at cell level.

In its current state, the formulation presented here has the ability to model polymeric and metallic foams respectively exhibiting visco-elastic and elasto-plastic

constitutive behavior at cell wall level. Polymeric foams are dominated by elastic deformation while metallic undergo mostly plastic deformation during the loading process. Different predictions could be obtained for polymeric foams by employing different cell wall material constitutive models such as coupled visco-elastic (Kelvin-Voigt model) local relations. Consideration of local elasto-plastic local relations which account for softening, necking and eventual fracture will render different results for metallic foams because the current approach for modeling the plastic behavior of the ligaments does not account for these effects. Additionally, the current plastic local relations do not account for the Bauschinger effect that results from loading-unloading and reverse loading. Therefore, local relations which account for the Bauschinger effect will also generate different predictions for metallic foams. Brittle foams undergo fracture in addition some yielding during collapse. Their signature response could be predicted by current model after some alterations. Consequently, work is currently under way to enhance the model with the ability to model materials which fracture during the loading process such as brittle ceramic foams. This involves preserving the history of plastic and fracture deformation in addition to considering local fracture constitutive relations at cell wall level. Still more challenging types of loading that remain to be addressed by the model are creep and fatigue Loading. A very challenging issue that remains to be addressed is contact that occurs between cell walls after neighboring cells collapse.

Industries envision potential applications for foam systems as impact absorbers and as energy mitigators therefore research work on the energy absorption capacity of different foam systems is currently needed. The developed model can be utilized for this purpose to a certain extent but currently it lack the ability to account for varying global strain rates which would trickle down to cell level as affine acceleration. Adding this capability will enhance the model tremendously. The temperature of foam materials increases during high strain rate impact loading therefore it is also necessary to consider temperature effects. Additionally many foam systems are used in high temperature environments as insulators therefore studies are need to learn about the effects of temperature the mechanical response. To provide a more complete treatment of the energy absorption capacity of foam materials it is essential to perform a careful

study of fluid flow around the cellular structure during dynamic loading. If desired, the current model can impose the strength of a filler material on the response of the solid phase but it doesn't consider the effects of fluid flow. One needs to perform a detailed, in dept investigation on the effects of the fluid phase surrounding the solid phase to learn of its contribution to both the quasi-static and dynamic foam response. This way the model will provide a thorough treat of the dynamically loaded open-cell foam, and at that point the model could possibly be applied to study semisolid foams such as wet foams (e.g. mayonnaise, whip cream, shaving cream, coffee foam).

The formulation presented here was developed for open-cell foam which can be modeled as a network of interconnected struts. The model is not applicable to closed-cell foams, however the same approach could be used to derive an equivalent model for closed-cell foams in dynamic loading environments. Axial and bending deformation can be accounted through stretching and curvature changes to the spherical membranes composing each cell in the cellular structure. Keeping track of the curvature and stretching of the membranes would allow us to account for the elastic and viscous effects. The inertial forces however need to be considered more carefully. Additionally, incorporation of warping of the membranes might be extremely challenging and very expensive computationally. The contribution from the fluid surrounding the cellular structure could be superimposed on the response of the solid phase, however if we are able to account for the flow of fluid in and around the cells of closed-cell foams, the model would provide a much more complete treatment. An model capable of predicting the dynamic response of closed-cell foams would be very useful to the community looking to exploit foam materials in energy absorption applications.

5.4 Final Comments

As pointed out throughout the dissertation, the current approach is only valid for situations where the cell size dimensions are much large the specimen region under consideration. Also, the relatively must be small so that we are not considering porous materials instead of low density foams. As mentioned earlier, the results presented here in general agree with the expected results of the physical problem and with the

available experimental data on cellular solids loaded at high strain rates, however a complete validation was not presented because equipment was not available and because experimental data was not available at most of the strain rates that were used for the simulations. In the future, once equipment or a suitable set of experimental data becomes available a thorough comparisons should be made with the simulation results. The expectation is that the model will agree in general with the pattern of the experimental response, but the specimens used in experiments usually have defective cells with cracks and unevenness of cell wall thickness which lower stress values, speed up the initiation of collapse, lower the collapse stress and reduce the compaction stress and strain. Therefore, it is very difficult to exactly match numerical and experimental results on cellular solids.

The model presented here could provide more accurate results if better local constitutive laws were specified. Improvement of the local constitutive laws requires a detailed study at cell wall level. For the dynamic simulations mentioned here, we used bulk material properties for the cell wall material properties. However, it has been shown that the properties of the material in the cell walls of foams can be very different compared to the properties of their bulk solid counterparts as result of small sizes and the curing process during foaming. For instance in metallic foams you are very likely to find just a few grains in a strut of an open-cell foam, which results in very different properties from the bulk solid metal. Therefore, it would be beneficial to utilize a multi-scale modeling technique based on first principles to obtain the properties and the behavior of the cell wall material in metallic foams. The multi-scale method would consists of obtaining the material properties from the bottom-up (crystals and their orientation, defects, inhomogeneities, cell walls etc) through computer simulations of models based on first principles. In addition to reducing some of the experimental drawbacks of measuring the micro-scale samples the multi-scale modeling method offers the possibility of achieving a deeper understanding of the physics of material behavior, supplying guidelines for cellular material design. Figure 5.1 shows the modeling approach for open cell metallic crystalline material, which clearly shows the different connections among hierarchical spatial scales. Each leg of the cell is a thin bar that is

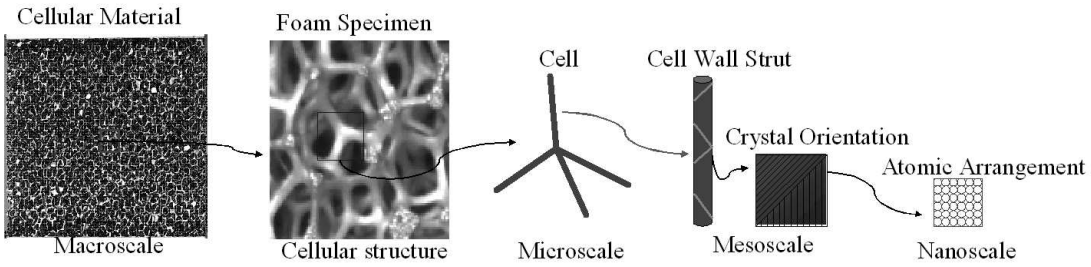

Figure 5.1: Depiction of metallic open-cell foams across the scales.

composed of multiple orientated crystals. The crystals have distinct boundaries where yield sliding and the stress concentration is expected to occur. Each grain of the crystals is divided into many elements, but many atoms will be included in a single element. In other words, the elements bridge the gap from nano- to meso-scale for the materials. The introduction of elements with a characteristic size between atoms and grains allows capturing nanoscale effects while providing average estimates for a relatively large size sample.

Appendix A

A.1 Evaluation of the Effective Foam Response w/ the Maxwell stress

When many cells are present in a foam specimen, the collapse of every cell occurs at the same stress, the plateau stress, at which point the strain for the cell goes from λ^- to λ^+ which are respectively the strain values at the start and end of collapse behavior. Once collapse is initialized until its completion, two groups of cells coexist to minimize the total energy. A group of un-collapsed cells with deformation λ^- and a group of collapsed cells with deformation λ^+ coexist to equilibrate the system. Therefore, during the interval of deformation between λ^- and λ^+, the cells dynamically transforms from one phase (un-collapsed) to another (collapsed) without visiting intermediate deformation states. Macroscopically, the foam specimen exhibits a completely convex energy landscape while microscopically the individual cells exhibit an energy landscape with a non-convex interval (see red/solid curve in Figure A.1b). One can obtain the effective response of a foam specimen from a microscopic simulation by convexification of the non-convex portion of the microscopic energy landscape as discussed in *chapter* 3 of Ericksen (1998) and in Gioia et al. (2001).

If we observe the energy vs. strain graphs in Figure A.1b, we obtain the entirely convex landscape (green/dashed curve) by linearly approximating the non-convex portion between λ^- and λ^+ of the microscopic energy landscape (red/solid curve). We can then obtain the Maxwell stress ($\mathbb{P}$) by determining the slope of the convexified energy landscape ($\mathbb{E} = \mathcal{W} + \mathcal{D} = \int P_{33} d\lambda$) between λ^- and λ^+ as written in Equation A.1 below.

$$\mathbb{P} = \left[\frac{d\mathbb{E}(\lambda)}{d\lambda}\right]_{\lambda^+} = \left[\frac{d\mathbb{E}(\lambda)}{d\lambda}\right]_{\lambda^-} = P_{33}(\lambda^+) = P_{33}(\lambda^-) \tag{A.1}$$

The Maxwell stress ($\mathbb{P}$) in then identified as the effective plateau stress ($P_{33}(\lambda^-)$ or $P_{33}(\lambda^-)$) for the macroscopic foam specimen. Note that since the convexified energy

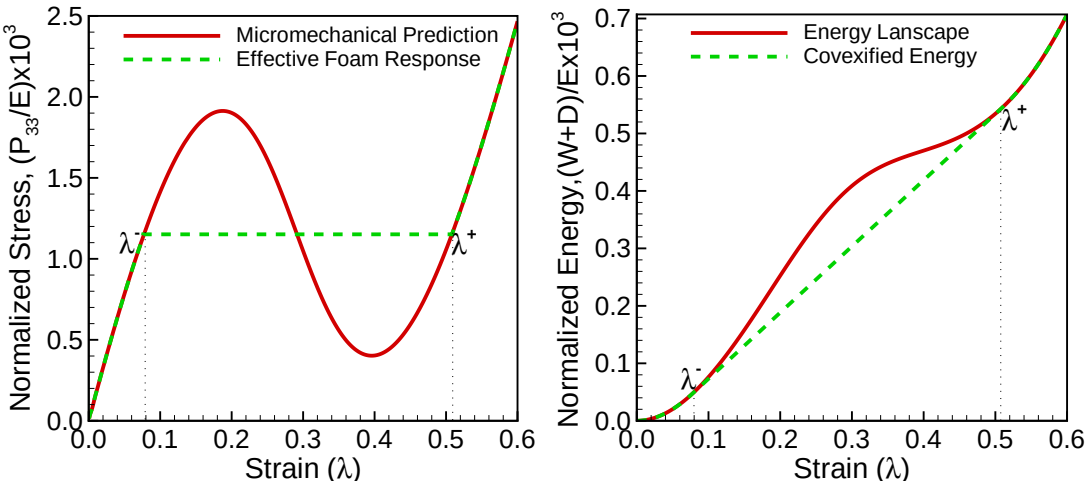

(a) Foam Response (b) Evolution of Potentials

Figure A.1: Evaluation of the macroscopic, effective foam specimen response from the micromechanical effective response during uniaxial dynamic compression. a) The compressive uniaxial First Piola-Kirchoff stress P_{33} normalized by the Youngs Modulus E plotted versus the uniaxial strain λ. The red/solid line represents the local micromechanical response and the green/dashed line represents the evaluated effective response with the Maxwell stress as the plateau stress. b) The elastic $\mathcal{W}$ plus viscous $\mathcal{D}$ energy potentials normalized by the Youngs Modulus E plotted against the uniaxial strain λ. The red/solid line represents the potential energy evolution with the non-convex region between strains λ^- and λ^+. The green/dashed line represents the convexified energy landscape where the non-convex region has been replaced by a linear approximation.

region is linear, the slope or the Maxwell stress is constant from λ^- to λ^+.

Figure A.1a shows the predicted microscopic response (red/solid curve) and the calculated effective response (green/dashed curve) including the collapse region for a foam specimen with homogeneous unit cell distribution. The convexification of the microscopic energy landscape corresponds to finding the points on the microscopic stress vs. strain graph (red/solid curve in Figure A.1a) where the change in area ($= \int_{\lambda^-}^{\lambda+} P_{33} d\lambda$) between two strain values λ^+ and λ^- is equal to the area ($= \mathbb{P}\Delta\lambda$ between the two strain values λ^+ and λ^- at the common stress $\mathbb{P}$ as shown in Equation A.2 below.

$$\Delta\mathbb{E} = \int_{\lambda^-}^{\lambda+} P_{33} d\lambda = \mathbb{P}\Delta\lambda = \mathbb{E}(\lambda^+) - \mathbb{E}(\lambda^-) \tag{A.2}$$

where

$$\Delta\lambda = \lambda^+ - \lambda^- \tag{A.3}$$

In Summary, the non-convex energy interval of the microscopic energy curve

defines the plateau or Maxwell stress ($\mathbb{P}$) and the extent of the plateau region ($\Delta\lambda$). The slope of this non-convex interval after it has been convexified (green dashed curve in Figure A.1b) defines the plateau stress. While the first and second inflection points λ^- and λ^+ respectively, define the extent of the plateau region. Using this procedure, one can obtain stress versus strain curves from micromechanical simulations such as the one in Figure A.1a which can be interpreted as representative of a foam specimen with a homogeneous distributions of cells.

Bibliography

Ashby, M. F., Evans, T., Fleck, N., Gibson, L., Hutchinson, J., Wadley, H., 2000. Metal Foams: A Design Guide, 1st Edition. Butterworth-Heinemann.

Banhart, J., 2003. Aluminum foams: On the road to real application. MRS Bulletin 28(4), 270306.

Bardenhagen, S. G., Brydon, A. D., Guilkey, J. E., 2005. Insight into the physics of foam densification via numerical simulation. Journal of the Mechanics and Physics of Solids 53, 597–617.

Boonyongmaneerat, Y., Chmielus, M., Dunand, D. C., Mllner, P., 2007. Increasing magnetoplasticity in polycrystalline ni-mn-ga by reducing internal constraints through porosity. The American Physical Society 99 (247201).

Chen, C. P., Anderson, W. B., Lakes, R. S., 1994. Relating the properties of foam to the properties of the solid from which it is made. Cellular Polymers 13, 16–32.

Chen, C. P., Lakes, R. S., 1996. Micromechanical analysis of dynamic behavior of conventional and negative poisson's ratio foams. Journal of Engineering Materials and Technology, Transactions of the ASME 118, 285–288.

Chen, W., Lu, F., Winfree, W., 2002. High-strain-rate compressive behavior of a rigid polyurethane foam with various densities. Experimental Mechanics 42, 65–73.

Chen, W., Lu, T. J., Fleck, N. A., 1999. Effect of imperfections on the yielding of two-dimensional foams. Journal of the Mechanics and Physics of Solids 47, 2235–2272.

Christensen, R. M., 1986. Mechanics of low density materials. Journal of the Mechanics and Physics of Solids 34, 563–578.

Cuitiño, A. M., Ortiz, M., 1992. A material-independent method for extending stress update algorithms from small-strain plasticity to finite plasticity with multiplicative kinematics. Engineering Computations 9, 437–451.

Cuitiño, A. M., Zheng, S., 2003. Taylor averaging of heterogenous foams. Journal of Composite Materials 37(8), 701–713.

Dannemann, K. A., Lankford, J., 2000. High strain rate compression of closed-cell aluminum foams. Materials Science and Engieering A293, 157–164.

Dement'ev, A. G., Tarakanov, O. G., 1970. Effect of cellular structure on the mechanical properties of plastic foams. Polymer Mechanics 6, 519–525.

Dement'ev, A. G., Tarakanov, O. G., 1973. Deformative properties of fexible plastic foams in compression. Polymer Mechanics 9, 395–400.

Demiray, S., Becker, W., Hohe, J., 2007. Numerical determination of initial and subsequent yield surfaces of open-celled model foams. International Journal of Solids and Structures 44, 20932108.

Deshpande, V. S., Ashby, M. F., Fleck, N. A., 2001. Foam topology bending versus stretching dominated architectures. Acta Materialia 49, 1035–1040.

Deshpande, V. S., Fleck, N. A., 2000a. High strain rate compressive behavior of aluminum alloy foams. International Journal of Impact Engineering 24, 277–98.

Deshpande, V. S., Fleck, N. A., 2000b. Isotropic constitutive models for metallic foams. Journal of the Mechanics and Physics of Solids 48, 1253–1283.

Deshpande, V. S., Fleck, N. A., 2001. Multiaxial yield behavior of polymeric foams. Acta Materialia 49, 1859–1866.

Ericksen, J. L., 1998. Introduction to the Thermodynamics of Solids, revised edition Edition. Springer-Verlag New York, Inc.

Erikson, R., 1999. Foams on the cutting edge. The American Society of Mechanical Engineers.

Evans, A. G., Hutchinson, J. W., Ashby, M. F., 1999. Multifunctionaly of cellular metal systems. Progress in Material Science 43, 171–221.

Evans, A. G., Hutchinson, J. W., Fleck, N. A., Ashby, M. F., Wadley, H. N. G., 2001. The topological design of multifunctional cellular metals. Progress in Material Science 46, 309–327.

Friis, E. A., Lakes, R. S., Park, J. B., 1988. Negative poisson's ratio polymeric and metallic foams. Journal of Materials Science 23, 4406–4414.

Fuganti, A., Lorenzi, L., Hanssen, A. G., Langseth, M., 2000. Aluminum foam for automotive applications. Advanced Engineering Materials 2 (4), 200–204.

Gent, A. N., Thomas, A. G., 1963. Mechanics of foamed elastic materials. Rubber Chemistry Tech. 63, 597–610.

Gibson, L., 2000. Mechanical behavior of metallic foams. Annual Review of Material Science 30, 191227.

Gibson, L. J., Ashby, M. F., 1982. The mechanics of three-dimensional cellular materials. Proc. R. Soc. Lond. A 382, 43–59.

Gibson, L. J., Ashby, M. F., 1997. Cellular Solids Structure and Properties, 2nd Edition. Cambridge University Press.

Gibson, L. J., Ashby, M. F., Schajer, G. S., Robertson, C. I., 1982. The mechanics of two-dimensional cellular materials. Proc. Royal Soc. London A 382, 25–42.

Gilchrist, A., Mills, N. J., 1994. Modeling of the impact response of motorcycle helmets. International Journal of Impact Engineering 15, 201–218.

Gioia, G., Wang, Y., Cuitiño, A. M., 2001. The energetics of heterogeneous deformation in open-cell solid foams. Proc. Royal Soc. London A 457, 1079–1096.

Gong, L., Kyriakides, S., 2005. Compressive response of open-cell foams. part ii: Initiation and evolution of crushing. International Journal of Solids and Structures 42, 1381–1399.

Gong, L., Kyriakides, S., Jang, W.-Y., 2005. Compressive response of open-cell foams. part i: Morphology and elastic properties. International Journal of Solids and Structures 42, 1355–1379.

Hall, I. W., Guden, M., Yu, C. J., 2000. Crushing of aluminum closed cell foams: density and strain rate effects. Scripta Mater. 43, 515–521.

Han, F., Zeu, Z., Gao, J., 1998. Compressive deformation and energy absorbing characteristics of foamed aluminum. Metall. Mater. Trans A 29, 2497–2502.

Hilyard, N. C., 1982. Mechanics of Cellular Plastics. Macmillan Publishing Co., Inc.

Hucko, B., Faria, L., 1997. Material model of metallic cellular solids. Computers and Structures 62, 1049–1057.

Kanahashi, H., Mukai, T., Nieh, T. G., Aizawa, T., Higashi, K., 2002. Effect of cell size on the dynamic compressive properties of open-celled aluminum foams. The Japan Institute of Metals 42, 2548–2553.

Kanahashi, H., Mukai, T., Yamada, Y., Shimojima, K., Mabuchi, M., Nieh, T., Higashi, K., 2001. Experimental study for the improvement of crashworthiness in az91 magnesium foam controlling its microstructure. Materials Science and Engineering A308.

Kanahashi, H., Mukai, T., Yamada, Y., Shimojima, K., Mabuchi, M., Nieh, T. G., Higashi, K., 2000. Dynamic compression of an ultra-low density aluminum foam. Materials Science and Engineering A280, 349–353.

Korner, C., Singer, R. F., 2000. Processing of metal foams – challenges and opportunities. Advanced Engineering Materials 4, 159–165.

Kraynik, A. M., Warren, M. K., Reinelt, D. A., Warren, W. E., 1997. Foams micromechanics. In: Proceedings of the NATO Advanced Study of Foams, Emulsions and Cellular Materials. Cargese, Corsica.

Kraynik, A. M., Warren, W. E., 1994. In: Hilyard, N. C., Conningham, A. (Eds.), Low Density Cellular Plastics. Cahapman and Hall, London.

Kusner, R., Sullivan, J. M., 1996. Comparing the weaire-phelan equal-volume foam to kelvin's foam. Forma 11, 233–242.

Lankford, J., Dannemann, K. A., 1998. Strain rate effects in porous materials. In: Schwartz, D. S., Shih, D. S., Evans, A. G., Wadley, H. N. (Eds.), Porous and Cellular Materials for Structural Applications. Vol. 251. Materials Research Society, pp. 103–108.

Laroussi, M., Sab, K., Alaoui, A., 2002. Foam mechanics: nonlinear response of an elastic 3d-periodic microstructure. International Journal of Solids and Structures 39, 3599–3623.

Lee, S., Barthelat, F., Espinosa, H. D., 2003. Strain rate effects in metallic cellular materials. In: Proceedings of the 2003 SEM Annual Conference and Exposition on Experimental and Applied Mechanics.

Lee, S., Barthelat, F., Hutchinson, J. W., Espinosa, H. D., 2006a. Dynamic failure of pyramidal truss core materials - experiments and modeling. International Journal of Plasticity 22, 2118–2145.

Lee, S., Barthelat, F., Moldovan, N., Espinosa, H. D., Wadley, H. N. G., 2006b. Deformation rate effects on failure modes of open-cell al foams and textile cellular materials. International Journal of Solids and Structures 43, 53–73.

Li, K., Gao, X. L., Roy, A. K., 2003. Micromechanics model for three dimensional open-cell foams using a tetrakaidecahedral unit cell and castigliano's second theorem. Composite Science and Technology 63, 1769–1781.

Loveridge, P., Mills, N. J., 1993. Prediction of packaging cushion curves and helmet liner responses. Cellular Polymer II Conference, Edinbburgh, RAPRA Technologies.

Lubliner, J., 1972. On the thermodynamic foundations of non-linear solid mechanics. International Journal of Non-Linear Mechanics 7, 237–254.

Lubliner, J., 1990. Plasticity Theory. Macmillan Publishing Company.

Meguid, S. A., Cheon, S. S., El-Abbasi, N., 2002. Fe modelling of deformation localization in metallic foams. Finite Elements in Analysis and Design 38, 631–643.

Menges, G., Knipschild, F., 1975. Estimation of mechanical properties for rigis polyurethane foams. Polymer eng. Sci. 64, 623–627.

Mills, N. J., 2000. Micromechanics of polymeric foams. Published in 3rd Nordic meeting on Materials and Mechanics, Aalborg, Denmark.

Mills, N. J., Gilchrist, A., 1991. The effectiveness of foams in bicycle and motorcycle helmets. Accident Analysis and Prevention 23, 153–163.

Mukai, T., Kanahashi, H., Miyoshi, T., Mabushi, M., Nieh, T. G., Higashi, K., 1999a. Dynamic compressive behavior of an ultra-lightweight magnesium foam. Scripta Materialia 41(4), 365–371.

Mukai, T., Kanahashi, H., Yamada, Y., Shimojima, K., Mabuchi, M., Nieh, T. G., Higashi, K., 1999b. Experimental study of the energy absorption in a closed-celled aluminum foam under dynamic loading. Scripta Materlia 40(8), 921–927.

Nagy, A., Ko, W. L., Lindholm, U. S., 1974. Mechanical behavior of foamed materials under dynamic compression. J. Cellular Plastics 10, 1–8.

Onck, P. R., Andrews, E. W., Gibson, L. J., 2001. Size effects in ductile cellular solids. part i: Modeling. International Journal of Mechanical Sciences 43, 681–699.

Ortiz, M., Stainer, L., 1999. The variational formulation of viscoplastic constitutive updates. Comput. Methods Appl. Mech. Engrg. 171, 419–444.

Overaker, D. W., Cuitiño, A. M., Langrana, N. A., 1998a. Effects of morphology and orientation on the behavior of two-dimensional hexagonal foams and application in a re-entrant foam anchor model. Mechanics of Materials 29, 43–52.

Overaker, D. W., Cuitiño, A. M., Langrana, N. A., 1998b. Elastoplastic micromechanical modeling of two-dimensional irregular convex and nonconvex (re-entrant) hexagonal foams. Journal of Applied Mechanics 65, 748–757.

Papka, S. D., Kyriakides, S., 1998. Experiments and full-scale numerical simulations of in-plane chrushing of a honeycomb. Acta Materialia 46, 2565–2776.

Perkowitz, S., 2000. Universal Foam. Anchor Books.

Plateau, J. A. F., 1873. Statique Experimentale et Theorique des Liquides soumis aux seules Forces Moleculaires. Gauthier-Villars, Paris.

Rinde, J. A., Hoge, K. G., 1971. Time and temperature dependence of the mechanical properties of polysteren bed foam. J. Appl. Polymer Science 15, 1377.

Romero, P. A., Zheng, S. F., Cuitiño, A. M., 2008. Modeling the dynamic response of viscoelastic open-cell foams. Journal of the Mechanics and Physics of Solids.

Shimojima, K., Chino, Y., Yamada, Y., Wen, C., Mabuchi, M., 2001. Compression test simulation of controlled cell shape open cellular magnesium alloy under dynamic loading. The Japan Institute of Metals 41, 1326–1331.

Shulmeister, V., der Burg, M. V., der Giessen, E. V., Marissen, R., 1998. A numerical study of large deformations of low-density elastomeric open-cell foams. Mechanics of Materials 30, 125–140.

Sihn, S., Roy, A. K., 2001. Modeling and stress analysis of open-cell carbon foam. In: 46th International SAMPE Symposium and Exhibition. 2001: Materials and Processes Odyssey. Society for the Advancement of Material and Process Engineering, pp. 230–242.

Sihn, S., Roy, A. K., 2004. Modeling and prediction of bulk properties of open-cell carbon foam. Journal of the Mechanics and Physics of Solids 52, 167–191.

Tedesco, J. W., Ross, C. A., Kuennen, S. T., 1993. Strain rate effects on the compressive strength of shock-mitigating foams. Journal of Sound and Vibration 165, 376–384.

Thompson, D. W., 1961. On Growth and Form, abridged Edition. Cambridge University Press.

Tyler, C. J., Ashby, M. F., 1986. Project report. Cambridge University Engineering Department.

Wang, Y., Cuitiño, A. M., 2000. Three-dimensional nonlinear open-cell foams with large deformations. Journal of the Mechanics and Physics of Solids 48, 961–988.

Wang, Y., Gioia, G., Cuitiño, A. M., 2000. The deformation habits of compressed open-cell foams. Transactions of the ASME 122, 376–378.

Warren, W. E., Kraynik, A. M., 1987. Foam mechanics: The linear elastic response of two-dimensional spatially periodic cellular materials. Mech. Mater. 6, 27–37.

Warren, W. E., Kraynik, A. M., 1988. The linear elastic properties of open-cell foams. Journal of Applied Mechanics 55, 341–346.

Warren, W. E., Kraynik, A. M., 1997. Linear elastic behavior of a low-density kelvin foam with open cells. Journal of Applied Mechanics 64, 787–794.

Weaire, D., Hutzler, S., 1999. The Physics of Foam. Oxford University Press.

Yamada, Y., Shimojima, K., Sakaguchi, Y., Mabuchi, M., Nakamura, M., Asahina, T., Mukai, T., Kanahashi, H., Higashi, K., 2000. Processing of cellular magnesium materials. Advanced Engineering Materials 4, 184–187.

Yi, F., Zhu, Z., Zu, F., Hu, S., Yi, P., 2001. Strain rate effects on the compressive property and the energy-absorbing capacity of aluminum alloy foams. Materials Characterization 47, 277–98.

Zhang, J., Kikuchi, N., Li, V., Yee, A., Nusholtz, G., 1998. Constitutive modeling of polymeric foam material subjected to dynamic crashloading. International Journal of Impact Engineering 21(5), 369–386.

Zhou, J., Gao, Z., Cuitiño, A. M., Soboyejo, W. O., 2004a. Effects of heat treatment on the compressive deformation behavior of open cell aluminum foams. Material Science and Engineering A 386, 118–128.

Zhou, J., Shrotriya, P., Soboyejo, W. O., 2004b. Mechanisms and mechanics of compressive deformation in open-cell al foams. Mechanics of Materials 36, 781–797.

Zhou, J., Soboyejo, W. O., 2004. Compression-compression fatigue of open cell aluminum foams: macro-/micro- mechanisms and the effects of heat treatment. Materials Science and Engineering A 369, 23–35.

Zhu, H. X., Knott, J. F., Mills, N. J., 1997a. Analysis of the elastic properties of open-cell foams with tetrakaidecahedral cells. Journal of the Mechanics and Physics of Solids 45, 319–343.

Zhu, H. X., Mills, N. J., , Knott, J. F., 1997b. Analysis of the high strain compression of open-cell foams. Journal of the Mechanics and Physics of Solids 45, 1875–1904.

Zhu, H. X., Windle, A. H., 2002. Effects of cell irregularity on the high strain compression of open-cell foams. Acta Materialia 50, 1041–1052.

Zilauts, A. F., Lagzdin, A. Z., 1992. Single-bar model of cellular materials subjected to large elastic deformations. Mech. Composite Materials 28, 1–7.

Vita

Pedro A. Romero

2008 Ph.D., Mechanical and Aerospace Engineering, Rutgers University
Piscataway, NJ

2006-2007 G.A.,Mechanical and Aerospace Engineering, Rutgers University
Piscataway, NJ

2005-2006 T.A., Mechanical and Aerospace Engineering, Rutgers University
Piscataway, NJ

2004 M.S., Mechanical and Aerospace Engineering, Rutgers University
Piscataway, NJ

2002-2005 NSF/Rutgers Fellow, STEM GK12 Program, Rutgers University
Piscataway, NJ

2001 Physics Instructor - CAHSEE YEP George Washington University
Washington, DC

2001 B.S., Mechanical and Aerospace Engineering, Rutgers University
Piscataway, NJ

2001 Minor, Economics, Rutgers University
New Brunswick, NJ

2000 Lucent Technologies Intern-Wireless Networks Division
Whippany, NJ

1999 United Technologies Intern - Pratt and Whitney-Computational Fluid Dynamics
East Hartford, CT

1998 U.S. Department of Energy Intern - Yucca Mountain Project Group
Las Vegas, NV

1996 H.S. Diploma, Class Salutatorian, Scholar Athlete, Weehawken High School
Weehawken, NJ